UNIVERSITÀ
DEGLI STUDI
DI PADOVA

Università degli Studi di Padova
Dipartimento di Fisica e Astronomia "Galileo Galilei"

SCUOLA DI DOTTORATO DI RICERCA IN ASTRONOMIA
INDIRIZZO UNICO, CICLO XXIV

New techniques to detect and characterize extrasolar planets

Direttore della Scuola: Ch.mo Prof. Giampaolo Piotto

Supervisore: Ch.mo Prof. Giampaolo Piotto
dott. Luigi R. Bedin

. . . . . .

Dottorando: Valerio Nascimbeni

. . . . . .

CONTENTS

ABSTRACT

The study of extrasolar planets (in short, "exoplanets") is one of the most young and rapidly-evolving fields of astronomical research. The present thesis is primarily about the development of new observational and reduction/analysis techniques to 1) characterize known transiting extrasolar planets by means of high-precision, ground-based differential photometry 2) to exploit the same data to search for additional bodies in known planetary systems, by employing the so-called Transit Time Variation (TTV) analysis. For both aims, I developed independent and customized software pipelines targeted at minimizing or correcting every significant source of uncorrelated ("red") noise. Most of my thesis is focused on the design and implementation of the TASTE project (once known as "The Asiago Search for Timing time variations of Exoplanets"), a long-term and multi-site photometric campaign to follow up a selected sample of transiting exoplanets at small/medium-sized facilities. The contents of each chapter in summarized in what follows:

1) Introduction

In this chapter I will briefly discuss the present status of exoplanetary research, including an overview of the main techniques employed so far to detect and characterize exoplanets. Then I will discuss why and how we are looking for smaller and lighter planets around bright stars, and what techniques have been developed to work out the resulting instrumental issues. In particular, I will describe what the TTV technique is, its theoretical basis and how it can be applied to real measurements. I will also review the first results obtained with this method, both from ground-based facilities and from CoRoT and Kepler space missions.

2) The implementation of TASTE

In this chapter I will describe the design and implementation of the TASTE project, as originally conceived to be operated at one single facility (the 1.82m telescope at the Asiago Observatory). I will discuss the technical requirements, the criteria adopted for the selection of the target sample, the observing strategy, and the first version of the STARSKY pipeline, optimized to carry out differential photometry on defocused images. I will present the first two light curves of the "hot Jupiters" HAT-P-3b and HAT-P-14b gathered by TASTE, and demonstrate that they achieve the accuracy required to detect Earth-mass

perturbers through TTVs, if locked on low-order orbital resonances such as 3:2 or 2:1.

This chapter is based on: V. Nascimbeni, G. Piotto, L. R. Bedin, M. Damasso (2011) *TASTE: The Asiago Search for Transit timing variations of Exoplanets. I. Overview and improved parameters for HAT-P-3b and HAT-P-14b*, A&A, 527, A85.

3) A new observational study of HAT-P-13b

In this chapter I will present the first observational TTV study published by the TASTE collaboration. This work was prompted by a paper of Pál et al. (2011), who claimed the detection of a sizeable TTV in the transits of HAT-P-13b (an interesting hot Jupiter hosted by a multiplanetary system). I will show that TASTE data are in agreement with the Pál et al. (2011) measurements, supporting –along with other archival data– the possible presence of a periodic TTV signal. I will point out how subsequent works (Southworth et al. 2012, Fulton et al. 2012) demonstrated that most past timing measurements were published with underestimated errors caused by neglected red noise, thus disproving the previously claimed TTV for this system.

This chapter is based on: V. Nascimbeni, G. Piotto, L. R. Bedin, M. Damasso, L. Malavolta, L. Borsato (2011) *TASTE II. A new observational study of transit time variations in HAT-P-13b*, A&A, 532, A24.

4) A homogeneous study of WASP-3b

In this chapter I will present the first TASTE work based on observations made at IAC facilities, namely a new study of the hot Jupiter WASP-3b from six high-precision light curves secured at the IAC-80 telescope. I will describe the thorough (re-)analysis carried out on both archival and our data, employing homogeneous techniques and software tools, with the goal of deriving auto-consistent planetary parameters and timing measurements. I will show that our ensemble data set is not in agreement with the periodic TTV previously claimed by Maciejewski et al. (2010). Instead, I will demonstrate that the measured TTV scatter is indeed statistically significant, though it does not show any significant periodicity. Hence I will discuss the possible causes for that behavior, and present an updated ephemeris and improved orbital/physical parameters for this target.

This chapter is based on: V. Nascimbeni, A. Cunial, S. Murabito, P. V. Sada, A. Aparicio, G. Piotto, L. R. Bedin, A. P. Milone, A. Rosenberg, L. Borsato, M. Damasso, V. Granata, and L. Malavolta (2012) *TASTE III. A homogeneous study of transit time variations in WASP-3b*, A&A, submitted.

5) Improved parameters for WASP-1b and HAT-P-20b

In this chapter I will analyze four high-precision light curves caught serendipitously at the Asiago 1.82m telescope (one of WASP-1b, three of HAT-P-20b). By also re-analyzing the most accurate archival data available, I will derive improved parameters and ephemeris for both targets, which do not show any significant TTV. I will discuss what upper limits can be set from this null detection to the mass of hypotetical perturbing planets.

This chapter is based on: V. Granata, V. Nascimbeni, G. Piotto, L. R. Bedin, L. Borsato, M. Damasso, L. Malavolta (2012) *TASTE IV. Refined ephemeris and parameters for WASP-1b and HAT-P-20b*, A&A, in preparation.

6) A search for planets in NGC 6397

In this chapter I will describe a search for transiting planets and variable stars carried out in an outer field of the globular cluster NGC 6397 from space-based HST observations. The main sample is a set of $\sim 2\,200$ cluster-member M dwarfs belonging to the same stellar popolation. I will describe the algorithms I developed to correct systematic errors in a data set composed by 252 ultra-deep archival images from the ACS camera. As no transits were detected, I will discuss the significance of this null result. I will report twelve unpublished variables of various types, all of them discovered among field stars.

This chapter is based on: V. Nascimbeni, L. R. Bedin, G. Piotto, F. De Marchi, R. M. Rich (2012) *An HST search for planets in the lower Main Sequence of the globular cluster NGC 6397*, A&A, 541, A144.

7) Field selection for PLATO

In the final chapter I will summarize my involvement in PLATO. Plato is a proposed ESA mission that will search primarily for low-mass, habitable planets around bright stars, covering up to the $\sim 40\%$ of the sky at the end of the mission. Suitable targets (dwarfs and subgiants later than spectral type F5, down to $V \sim 13$) have to be selected in advance. An unprecedented all-sky stellar classification is then needed. Within the Working Package (WP 131210: "Analysis of photometric and astrometric catalogues") I evaluated the feasibility and reliability of stellar classification techniques based upon the existing and forthcoming photometric/astrometric catalogs.

SOMMARIO

Lo studio dei pianeti extrasolari (o "esopianeti") è una branca della ricerca astronomica molto giovane e in rapidissima evoluzione. Il lavoro svolto nella presente tesi riguarda principalmente lo sviluppo di nuove tecniche di osservazione e di riduzione e analisi dati al fine di 1) caratterizzare pianeti extrasolari transitanti già noti attraverso fotometria differenziale di alta precisione, condotta da terra; e 2) fare uso degli stessi dati per cercare nuovi corpi in sistemi planetari già noti, sfruttando una tecnica di analisi nota come TTV (*Transit Time Variation:* variazione dei tempi di transito). Per entrambi gli scopi, ho sviluppato strumenti software indipendenti e mirati al fine di minimizzare o correggere ogni sorgente rilevante di errori sistematici (noto anche come *correlated noise* o *red noise*). Gran parte della mia tesi è focalizzata sulla progettazione e implementazione del progetto TASTE, una campagna osservativa multisito e a lungo termine per monitorare un campione selezionato di esopianeti con telescopi terrestri di classe piccola e media. Il contenuto di ciascun capitolo è riassunto in seguito.

1) Introduzione

In questo capitolo tratterò in breve la situazione attuale della ricerca sugli esopianeti, comprendente anche una panoramica sulle principali tecniche finora impiegate per rivelare e caratterizzare pianeti extrasolari. Quindi passerò a discutere perché e come la comunità scientifica si sta orientando verso la ricerca di pianeti sempre più piccoli e leggeri attorno a stelle brillanti, e illustrerò le tecniche sviluppate per aggirare i limiti attualmente imposti dagli strumenti. In particolare, descriverò in cosa consiste la tecnica TTV, quali sono i principi teorici sui quali si fonda e come questi possano essere applicati a misure reali. Passerò infine in rassegna i primi risultati ottenuti applicando questo metodo, sia da strumentazioni terrestri che dalle missioni spaziali Kepler e CoRoT.

2) Implementazione del progetto TASTE

In questo capitolo descriverò la progettazione e l'implementazione di TASTE nella configurazione originaria: ovvero, come un progetto concepito per un singolo telescopio (il riflettore Copernico da 1.82m presso l'Osservatorio Astrofisico di Asiago). Discuterò i requisiti tecnici imposti, i criteri adottati per la selezione del campione di oggetti, la strategia osservativa e la prima versione della pipeline software STARSKY, ottimizzata per eseguire fotometria differenziale di apertura su immagini appositamente sfuocate. Presenterò le prime curve di

luce pubblicate da TASTE, dei pianeti cosiddetti "hot Jupiters" HAT-P-3b e HAT-P-14b, e dimostrerò che esse raggiungono l'accuratezza fotometrica necessaria per rilevare con la tecnica TTV pianeti perturbatori di massa terrestre, nel caso questi ultimi siano bloccati in una risonanza orbitale di basso ordine, come 3:2 o 2:1.

Questo capitolo è basato sull'articolo: V. Nascimbeni, G. Piotto, L. R. Bedin, M. Damasso (2011) *TASTE: The Asiago Search for Transit timing variations of Exoplanets. I. Overview and improved parameters for HAT-P-3b and HAT-P-14b*, A&A, 527, A85.

3) Un nuovo studio osservativo di HAT-P-13b

In questo capitolo presenterò il primo studio TTV osservativo pubblicato dalla collaborazione TASTE. Questo lavoro è stato stimolato da un articolo di Pál et al. (2011) che rivendicava la scoperta di un considerevole segnale TTV nei transiti del pianeta HAT-P-13b (un caso interessante di "hot Jupiter" ospitato da un sistema planetario multiplo). Mostrerò che i dati raccolti da TASTE sono in accordo con le misure di Pál et al. (2011), il che conforta –assieme ad altri dati di archivio– la possibile presenza di un segnale TTV periodico. Infine metterò in evidenza che lavori più recenti (Southworth et al. 2012, Fulton et al. 2012) hanno tentato di dimostrare che molte misure condotte in passato sono state pubblicate con errori di gran lunga sottostimati, a causa della presenza di *red noise* trascurato durante la fase di analisi di dati. Per questo motivo, oggi si ritiene probabile che la rivendicazione di Pál et al. (2011) sia spuria.

Questo capitolo è basato sull'articolo: V. Nascimbeni, G. Piotto, L. R. Bedin, M. Damasso, L. Malavolta, L. Borsato (2011) *TASTE II. A new observational study of transit time variations in HAT-P-13b*, A&A, 532, A24.

4) Un'analisi omogenea del sistema WASP-3

In questo capitolo presenterò il primo lavoro del progetto TASTE basato su osservazioni condotte presso l'Observatorio del Teide dell'*Instituto de Astrofisica de Canarias* (IAC): sei curve di luce ad alta precisione ottenute con il telescopio IAC-80. Descriverò l'analisi approfondita che è stata svolta sia su dati di archivio che sulle nostre misure, facendo uso di tecniche e software di riduzione/analisi omogenei. Lo scopo è di derivare parametri del pianeta e misure di tempo di transito in modo completamente autoconsistente. Illustrerò come l'insieme dei dati disponibili non sia in accordo con il presunto segnale TTV periodico rivendicato da Maciejewski et al. (2010). Al contrario, dimostrerò che la dispersione delle misure TTV è statisticamente significativa, sebbene priva di qualsiasi tipo di periodicità rivelabile. Passerò quindi a discutere le possibili cause di questo comportamento, pre-

sentando un'effemeride aggiornata per WASP-3b e ricavando per lo stesso parametri fisici e orbitali aggiornati.

Questo capitolo è basato sull'articolo: V. Nascimbeni, A. Cunial, S. Murabito, P. V. Sada, A. Aparicio, G. Piotto, L. R. Bedin, A. P. Milone, A. Rosenberg, L. Borsato, M. Damasso, V. Granata, and L. Malavolta (2012) *TASTE III. A homogeneous study of transit time variations in WASP-3b*, A&A, submitted.

5) Parametri fisici e orbitali di WASP-1b e HAT-P-20b

In questo capitolo analizzerò quattro curve di luce di alta precisione ottenute serendipicamente con il telescopio da 1.82m di Asiago (un transito di WASP-1b e tre transiti completi di HAT-P-20b). Rianalizzando anche i più accurati dati di archivio attualmente disponibili, deriverò un'effemeride e dei parametri fisici e orbitali più precisi per entrambi i pianeti. Nessuno dei due mostra un segnale TTV significativo. Discuterò infine quali limiti superiori possono essere stimati riguardo alla massa di un ipotetico pianeta perturbatore in base a questa misura nulla.

Questo capitolo è basato sull'articolo: V. Granata, V. Nascimbeni, G. Piotto, L. R. Bedin, L. Borsato, M. Damasso, L. Malavolta (2012) *TASTE IV. Refined ephemeris and parameters for WASP-1b and HAT-P-20b*, A&A, in preparation.

6) Una ricerca di pianeti in NGC 6397

In questo capitolo descriverò una ricerca di pianeti transitanti e stelle variabili condotta in un campo stellare periferico dell'ammasso globulare NGC 6397, sfruttando osservazioni di archivio del telescopio spaziale Hubble. Il campione principale è costituito da un insieme di $\sim 2\,200$ nane rosse appartenenti all'ammasso. Descriverò gli algoritmi che ho sviluppato per correggere gli errori fotometrici sistematici presenti in un insieme di 252 immagini ultraprofonde riprese con la camera ACS nel 2006. Poiché non sono stati rivelati transiti, discuterò la significatività di questo risultato nullo. Infine, descriverò e caratterizzerò dodici stelle variabili di diverse tipologie scoperte per la prima volta. Tutte queste variabili sono sorgenti di campo, non appartenenti all'ammasso.

Questo capitolo è basato sull'articolo: V. Nascimbeni, L. R. Bedin, G. Piotto, F. De Marchi, R. M. Rich (2012) *An HST search for planets in the lower Main Sequence of the globular cluster NGC 6397*, A&A, 541, A144.

7) Selezione del campo di vista di PLATO

Nell'ultimo capitolo passerò in rassegna il lavoro che mi ha visto coinvolto nello studio preparatorio per PLATO. PLATO è una missione

spaziale proposta all'ESA che cercherà principalmente pianeti "abitabili" di piccola massa attorno a stelle brillanti, coprendo alla fine della missione un angolo sferico pari al ~ 40% dell'intero cielo. I target adatti comprendono stelle nane e subgiganti di tipo spettrale F5V e più freddi, più brillanti della magnitudine $V \sim 13$. Tali target devono essere selezionati prima dell'inizio della missione vera e propria, pertanto è necessaria una classificazione stellare su tutto il cielo, e molto più profonda di quelle attualmente disponibili. All'interno del gruppo di lavoro WP 131210 (*"Analysis of photometric and astrometric catalogues"*) ho investigato la fattibilità e l'affidabilità delle tecniche di classificazione stellare basate sui cataloghi fotometrici e astrometrici, sia quelli disponibili che quelli di prossima realizzazione.

1 INTRODUCTION

The discovery and characterization of extrasolar planets (in short, "exoplanets") is one of the youngest and most rapidly-evolving field of astronomical research. Theoretical speculations about the existence of other worlds have been around from antiquity, but only in the second half of twentieth century the technological progress made feasible the genuine detection of planetary bodies around stars other than the Sun (Struve 1952).

Some authoritative claims published in the past about discovered exoplanets are now widely recognized to be spurious (i.e., the planetary system around the Barnard's star proposed by van de Kamp 1969). The first publication of a confirmed discovery of an exoplanet had to wait 1992, though it concerns a very exotic system hosted by a pulsar (Wolszczan & Frail 1992). Instead, the first planet around a "normal" main-sequence star was announced only few years later by Mayor & Queloz (1995). Since then, the number of known exoplanets is steadily growing (Fig. 1, yellow histogram), having surpassed the 100 discoveries/yr for the first time in 2011. About 780 planets, of which 102 hosted by multiple planetary systems, are confirmed at the time of writing (`exoplanet.eu` online database).

I will briefly review in Section 1.1 the main techniques employed so far both for the detection and characterization of exoplanets. This includes the Transit Time Variation (TTV) method, which plays a central role in most of my thesis work.

1.1 DETECTION TECHNIQUES

Many techniques, both direct and indirect, have been developed to detect the extremely small signal caused by presence of a planet. Even in the favourable case of a Jupiter-like giant planet around a solar twin, we are dealing with an object more than ~ 300 times lighter than its host star, ~ 1000 less bulky and several order of magnitude fainter at visible wavelenghts, lying at angular distances much smaller than one arcsecond. We will summarize these techniques in decreasing order of number of confirmed discoveries, the most successful methods being so far that based on Radial Velocity (Fig. 1, blue histogram).

1.1.1 *Radial velocities*

The gravitational pull of the planet set its host star in a periodical motion around the center of mass of the system (Seager 2011a,

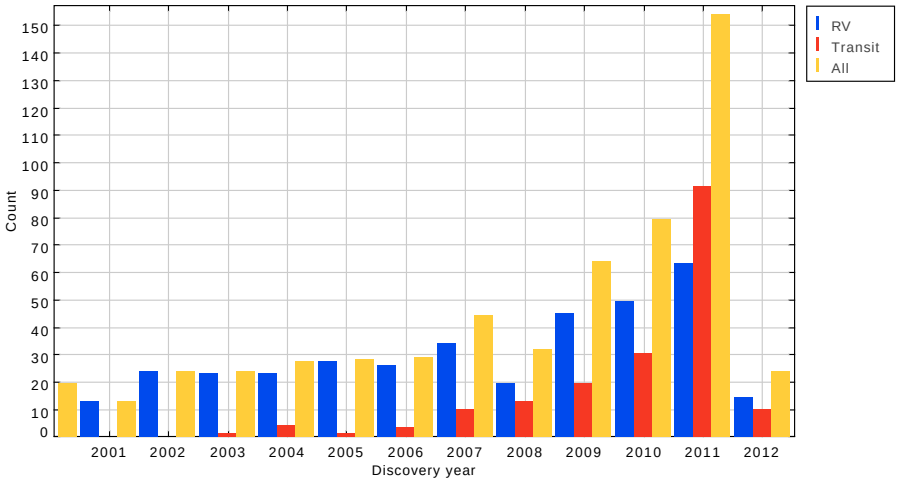

Figure 1: Number of discovered exoplanets as a function of year, overall (yellow histogram) and selected for detection method: radial velocity (blue histogram) and transits (red histogram). Updated: May 2012.

p. 27). Through Doppler effect, this motion induces a radial velocity (RV) variation of the host star of semiamplitude K, that can be detected with accurate spectroscopical measurements of the stellar photosphere. Naming $M_\star$ the stellar mass, M_p the planetary mass, and P, e, i the orbital period, eccentricity and inclination respect to the line of sight, from the solution of the two-body problem it is straightforward to derive that

$$K = \left(\frac{2\pi G}{P}\right)^{1/3} \frac{M_p \sin i}{M_\star^{2/3}} \frac{1}{\sqrt{1-e^2}} \tag{1}$$

or, by measuring P in days, $M_\star$ in solar masses $M_\odot$, and M_p in Earth- or Jupiter-mass $M_\oplus$, M_{jup} units we get

$$K = 0.64 \text{ m s}^{-1} \left(\frac{M_p \sin i}{M_\oplus}\right) \frac{M_\star^{2/3}}{P^{1/3}\sqrt{1-e^2}} \tag{2}$$

$$K = 203.2 \text{ m s}^{-1} \left(\frac{M_p \sin i}{M_{jup}}\right) \frac{M_\star^{2/3}}{P^{1/3}\sqrt{1-e^2}} \tag{3}$$

It is easy to notice from Eq. 1 that RV techniques are strongly biased towards massive planets with short orbital periods. The first planets discovered by RVs, including 51 Peg b (Mayor & Queloz 1995) were indeed objects belonging to a previously-unknown class of short-period ($P < 10$ d) giant planets ($M_p \sim M_{jup}$), now called "hot Jupiters". In the following years, exploiting a larger temporal baseline, giant planets with longer orbital periods were found (Santos et al. 2001), and now they constitute the vast majority of the whole sample (Fig. 2, blue dots). Some of them are within the so-called "habitable zone" (HZ),

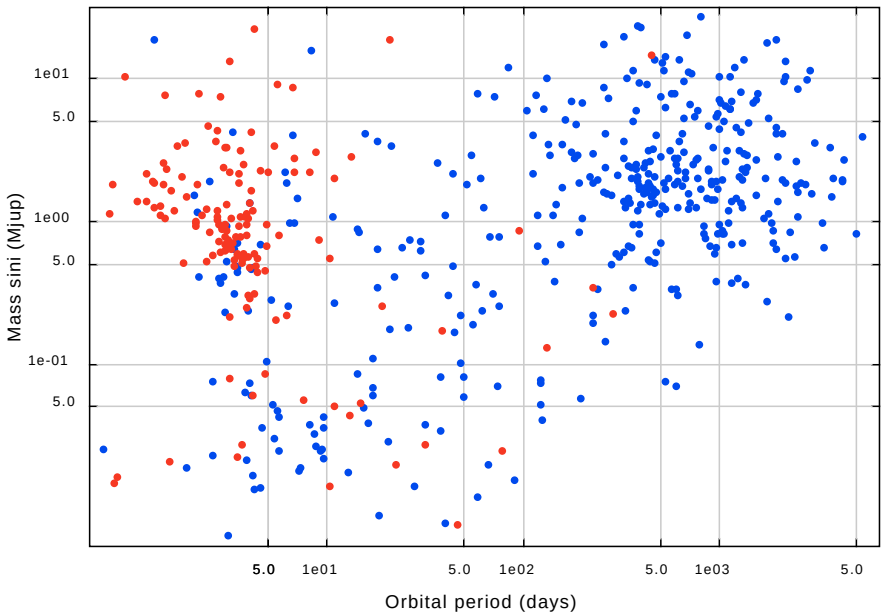

Figure 2: Exoplanets discovered through transit technique (red dots) and RV technique (blue points) as distributed in the orbital period P vs. *projected* planetary mass $M_p \sin i$ plane. Updated: May 2012.

where water is expected to exist in a liquid state (Kane & Gelino 2012).

The weak point of this technique is the fact that it is not possible to break the degeneracy between M_p and $\sin i$ only by means of RV measurements: a massive planet on a nearly face-on orbit could yield the same $M_p \sin i$ signal of a light planet whose orbit is seen edge-on. Moreover, no information can be gathered about the *size* of the planet, needed to infere its density and to give a hint about its internal composition.

The discovery of low-mass planets (i.e., with a mass equal or smaller than the arbitrary transition boundary $M_p \sim 30 M_\oplus$ between gaseous giants and icy/rocky solid planets) was made possible by the introduction of a new class of ultra-stable spectrographs, capable to achieve long-term RV accuracy of the order of ~ 1 m/s. The discovery parameter space (Fig. 2) is now being filled with new classes of short-period Neptunian ($10 < M_p < 30\ M_\oplus$) and so-called "super Earth" planets ($M_p < 10\ M_\oplus$). The pioneering instrument in this field is HARPS, mounted in 2003 on the ESO 3.6m telescope at La Silla, Chile and still carrying out its scientific program (Pepe et al. 2000). HARPS-N, an improved HARPS twin currently under commissioning at the italian Telescopio Nazionale Galileo (TNG), will push even farther the HARPS performances, extending the coverage to the northern emisphere.

1.1.2 *Transits*

Photometric transits are the second most successful method of discovery (Fig. 1, red histogram), and the fastest growing one at the present Winn (2010). This technique exploits planetary systems having a particular geometric alignment: those whose orbital planes are seen nearly edge-on ($i \simeq 90°$), and cross fully or partially the disk of their host stars as seen from the Earth. We can assume that, at visible wavelenghts, the planetary disk is essentialy dark and opaque. In this case, during the transit, a tiny dimming of the star light is observed, caused by the small fraction of photosphere occulted by the planet. By knowing the planetary orbital/physical parameters and the limb darkening properties of the star, the amount of dimming as a function of time can be precisely modeled by analytic functions, the most employed being that by Mandel & Agol (2002). In first approximation, however, the photometric dimming at its maximum (called transit *depth*) is

$$\delta \simeq \left(\frac{R_p}{R_\star}\right)^2 \simeq 0.01 \left(\frac{R_p}{R_{jup}}\right)^2 \left(\frac{R_\odot}{R_\star}\right)^2 \text{ mag} \tag{4}$$

that is, about 0.01 mag for a Jupiter analog around a solar twin, and only 80 μmag for a Earth-sized planet. Things get better on low-main sequence stars, since δ is strongly dependent on the stellar radius. A planet hosted by a M0V red dwarf will yeld a transit four times deeper than the same planet around a G2V.

The first planetary transit ever detected (the hot Jupiter HD 209458b; Charbonneau et al. 2000; Henry et al. 2000) was already discovered with RV measurements, and purposely monitored at the inferior conjunction. After that, many dedicated wide-field surveys have been implemented to detect transits, the most successful being SuperWASP (Pollacco et al. 2006) and HATNet (Bakos et al. 2002). Similarly to what was noted about RV techniques, most discoveries published so far are of giant planets, whose signal is well within reach of ground-based photometry (red dots in Fig. 2). The handful of Neptune-sized or super-Earth planets discovered from the ground are indeed hosted by K- and M-type stars, whose small radius raises δ above the empirical ~ 0.003 mag detection threshold presently imposed by night-to-night systematic errors in ground-based photometry. Photometry is of course much more efficient than spectroscopy in terms of photons, and thus able to probe planets on fainter stars. The difference is made clear by comparing the magnitude of the host stars: known RV planets peak at $V \sim 8$, while transiting planets peak at $V \sim 11.5$ (Fig. 3, blue and red points respectively).

A big leap forward has been made with the introduction of space-based photometric surveys, first by the French satellite CoRoT (Auvergne et al. 2009) and then by the Kepler Mission (Borucki et al.

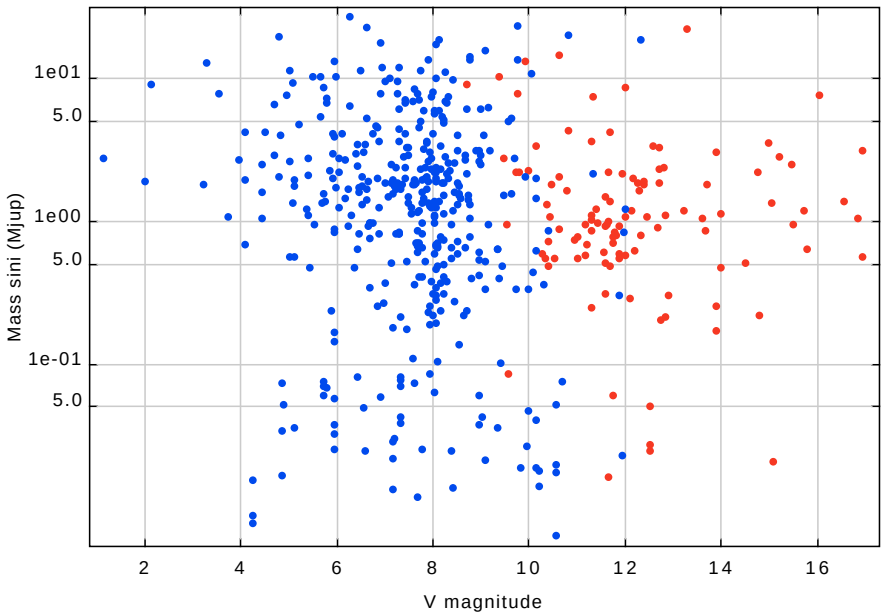

Figure 3: Exoplanets discovered through transit technique (red dots) and RV technique (blue points) as distributed in the host-star magnitude V vs. *projected* planetary mass $M_p \sin i$ plane. Updated: May 2012.

2010), which sets the current state-of-art in its field. Kepler is 0.95-m Schmidt telescope which monitors a single $\sim$ 105 deg^2 field of view between Lyra and Cygnus. Time coverage is nearly continuous and lasting from May 2009: the mission has been recently extended through 2016. Some of the most striking results are the first planetary system with more than one transiting planet (Kepler-9, Holman et al. 2010), a multiple system with six transiting low-mass planets (Kepler-11, Lissauer et al. 2011), and the first small-size candidate planet in the HZ of a solar-type star (Kepler-22b, Borucki et al. 2012), still awaiting confirmation and mass estimate.

The most limiting factor of the transit tecnique is that only a small fraction of planetary systems are expected to yeld transits, given that the chances of a suitable orbital alignment are of the order of R_p/a, where a is the semimajor axis (Winn 2010). That is, only $\sim$ 10% of "hot" planets ($P < 10$ days), and 0.5% of Earth analogs can be caught transiting. This geometrical factor strongly biases detections made by transit technique towards large planets on short-period orbit, just in the same way RV techniques are biased towards massive, short-period planets. As M_p and R_p are correlated, this is reflected in the (M_p, P) parameter space, where a large fraction of planets discovered by transits could be classified as hot Jupiters (red dots in Fig. 2). Another drawback of transit photometry is that it cannot provide us with any hint about the planetary mass. For this reason, transits (yielding R_p, i and precise P) and RV measurements (yelding $M_p \sin i$ and e) are higly complementary, and represent the current "golden standard" to

confirm and characterize a candidate. Both techniques together give access to the real –unprojected– mass M_p of the planet, and hence to its density along with a first estimate of what it is made of: gases, ices, or rocks.

Transiting planets are also valuable because of the opportunity they give us in studying their atmospheres (Seager & Deming 2010). By performing differential spectrophotometry between off-transit and in-transit observations, we can detect signatures of molecules and atoms in the planetary atmosphere, because during transits some star light is scattered and selectively absorbed through the atmospheric limb (so-called *trasmission spectroscopy*; Charbonneau et al. 2002).

Most transiting planets are expected to be also periodically eclipsed by the stellar disk (a phenomenon called "occultation" or "secondary transit"), though for some eccentric orbits occultations could not occur at all (Winn 2010). The depth of an occultation provides useful information about the albedo of the planet (at visible wavelengths) or about its surface temperature (in the infrared), as demonstrated for the first time by Charbonneau et al. (2005). *Occultation spectroscopy*, in analogy with transmission spectroscopy, yields a differential measurement of the reflection spectrum of the planet. The latter has been suggested by Seager & Deming (2010) as one of the most accessible technique to study exoplanetary atmospheres in the the near future..

1.1.3 *Direct Imaging*

To detect an exoplanet by resolving its image is the most direct method of discovery (Seager 2011a, p. 111). Yet, it is extremely challenging due both to the tiny angular separation from its host star (well below the typical atmospheric seeing for most known planets), and to their extreme flux ratio ($F_p/F_\star \sim 10^{-8}$ for a Jupiter-like planet in the visible region). The achievement of the required performances is a major technological effort, involving advanced coronographic techniques and adaptive optics (AO).

The first direct imaging discoveries were announced in 2008 by different teams (Marois et al. 2008; Kalas et al. 2008; Lagrange et al. 2009) both exploiting ground- and space-based facilities. All these targets share common properties: they are long-period planets in nearby systems (i. e., with a relatively large angular separation) hosted by very young stars. Their young age implies a large temperature, thus a most favorable planet/star contrast. This planetary class is virtually undetectable with RV or transits, thus direct imaging is highly complementary method.

1.1.4 *Microlensing*

During a so-called *microlensing* event, the light of a background star is gravitationally distorted by a closer foreground star, which acts as a lens (Paczynski 1991). This phenomenon follows the laws of general relativity and is time-dependent, due to the proper motion of the "lens" star. The lensed image cannot be spatially resolved, but it is possible to infer the system geometry by modeling time-resolved photometric observations. The light curve for a single-lens event, showing a sudden brightening on a timescale of few days, can be compared against predictions by models (Gould & Loeb 1992). During so-called "high-magnification events", the brightening spans several magnitudes, and significant deviations from the single-lens model could be due to additional bodies around the lens star.

Microlensing is pretty efficient in detecting planets of small mass and at large separations. For instance, OGLE-2005-BLG-390Lb was announced to be a 5.5 $M_\oplus$ super-Earth at 2.5 AU from its host star (Beaulieu et al. 2006). The planetary signal on this faint, distant, unresolved star would be undetectable with RV or transits, thus microlensing adds a valuable amount of information on the parameter space, as pointed out by statistical studies (Cassan et al. 2012). On the other hand, microlensing gives no or limited information on most parameters (including e, i, R_p) and relies on a single, non-repeatable event for which follow-up observations are unfeasible.

1.1.5 *Astrometry*

The center of a star is, in general, offset from the barycenter of the system if one or more additional bodies are present, and celestial mechanics is able to predict the motion of the photocenter around the center of mass once the orbital parameters of the perturbers are known. By inverting the problem, accurate astrometric measurements could be exploited to infere the presence of planets (Sozzetti 2005). The underlying dynamical laws are similar to those employed to derive the stellar RV wobble, with the important difference that the astrometric signal is dependent on the position of the star (instead of velocity). If we measure the semimajor axis a in AU and the distance d from the Sun in pc, the observed astrometric shift in arcsec for a single planet in circular orbit is

$$\alpha = \frac{M_p}{M_\star}\frac{a}{d} \tag{5}$$

or, using more handful mass units:

$$\alpha[\text{mas}] \simeq \frac{M_p/M_{jup}}{M_\star/M_\odot}\frac{a}{d} \tag{6}$$

The astrometric method is biased towards planets on large separation (provided that observations span a time range large enough to sample the orbital period) and are not limited to edge-on orbits, being on the contrary more efficient with systems oriented face-on. Thus astrometry and RVs together could reveal the "real" mass M_p and reconstruct the full orbital solution of the planet.

On the other hand, even assuming a 1 M_{jup} planet at 1 AU around a close solar-type star ($d \sim 10$ pc, 1 $M_\odot$) the maximum observable astrometric signature is about 0.1 mas, too small to be measured by ground-based techniques and challenging even with space-based telescope like HST. The most promising targets are close, very late-type stars (M dwarfs) hosting massive planets. The only astrometrically detected planet known so far is indeed GJ 876b, previosly discovered by RVs (Benedict et al. 2002).

Most claims of exoplanetary discoveries made through astrometry have been disproved by subsequent follow-ups (the most recent being that published by Pravdo & Shaklan 2009). Yet, future space mission such as GAIA are expected to yeld hundreds or thousands of discoveries of giant planets (Dzigan & Zucker 2012).

1.1.6 *Timing Techniques*

Just like for RV and astrometric methods, timing techniques exploit the motion of the host star with respect to the barycenter of the planetary system. By measuring a strictly periodic signal originated from the star, the period is expected to display apparent changes ΔP due to variations of path covered by light. This effect is also known as LTE (light travel effect). For a circular orbit with semimajor axis a and inclination i, the maximum period variation is

$$\Delta P = \frac{1}{c} \frac{M_p}{M_\star} a \sin i \tag{7}$$

that is, with more familiar units,

$$\Delta P[s] = \frac{1}{2} \frac{M_p/M_{jup}}{M_\star/M_\odot} a[AU] \sin i \tag{8}$$

Many types of periodic signals can be exploited:

1. Collimated radio pulses from fast-rotating neutron stars (pulsars). This is the technique employed to discover the first confirmed planetary system, around the millisecond pulsar PSR 1257+12 (Wolszczan & Frail 1992). Since then only other two pulsars were discovered to host planets.

2. Stellar oscillations (g-modes) from white dwarfs or sdB stars. Unlike pulsars, which need to be monitored with radiotelescopes, these oscillations can be measured with conventional photometry by employing a network of small/medium-sized optical

telescopes. The first planet announced, V 391 Pegasi b, is long period gas giant ($M_p \sim 3.2\ M_{jup}$, $a = 1.7$ AU) orbiting a sdB star. At least another similar system have been discovered (around NY Vir) and an extensive monitoring of compact dwarfs is ongoing (EXOTIME project). (Silvotti et al. 2007).

3. Minimum light instants of detached eclipsing binaries (dEB). Like the previous case, dEB timing is in principle well within reach of ground-based photometry. After the first discovery made by Lee et al. (2009) of a multiple system on HW Vir, similar claims were published (and, sometimes, disputed) on six other systems.

It has been suggested that present and future photometric space missions (CoRoT, Kepler, Plato) will be very fruitful in detecting planets by employing the dEB timing technique (Schwarz et al. 2011). Yet, no claim was made so far.

1.2 TRANSIT TIMING VARIATIONS

The Transit Timing Variation technique (TTV) is somewhat different from the other timing methods discussed in the previous section, because it involves a system where at least one planet must transit. In addition, timing deviation might be due not only to LTE effects, but also to planet-planet gravitational perturbations, both short-term and secular (Fabrycky 2010).

By monitoring a known transiting planet by high-precision photometry, the central instant T_0 of each individual transit can be estimated. The gravitational perturbation of a previously-unknown third body, not necessarily transiting, can cause significant variations of the orbital period P (Holman & Murray 2005). The effect is greatly increased if the perturber is locked in a low-order mean-motion resonance with the transiting planet (Agol et al. 2005). Most of this thesis is about the TASTE project, started in 2010 to search for TTVs with several ground-based, medium-class facilities on a sample of carefully selected targets (Nascimbeni et al. 2011a). The main tool of TTV analysis is the so-called $O-C$ (*observed* $-$ *computed*) diagram: each measured T_0 is subtracted from the value predicted by a linear ephemeris in the form $T_0 = T_{ref} + NP$, where epoch N is the number of transits elapsed since a reference time T_{ref}, being P the mean orbital period of the monitored planet. In absence of perturbation, a "flat" $O-C$ is expected within the error bars.

The TTV technique has been proven to work by several results from the Kepler mission. Some candidate transiting planets in multiple systems, for instance, were validated through TTV analysis (Lissauer et al. 2011). Other confirmed TTV systems include Kepler-19c, the first non-transiting planet discovered through transit timing (Bal-

lard et al. 2011). Unfortunately, the orbital parameters of Kepler-19c have been not uniquely determined: various dynamical mechanisms match the amplitude, period, and shape of the measured signal. Finally, KOI-872.02 (now renamed Kepler-46c) is the first non-transiting, TTV-detected planet whose parameters are inferred within reasonable error bars (Nesvorný et al. 2012).

In the past few years, some authors have claimed TTV detections also from ground-based facilities, but none is confirmed so far. Among these claims, WASP-10b (Maciejewski et al. 2011), WASP-5b (Fukui et al. 2011), the intriguing case of HAT-P-13b (Pál et al. 2011; Nascimbeni et al. 2011c; Southworth et al. 2012), and WASP-3b (Maciejewski et al. 2010). It is known that the impact of red noise on high-precision transit photometry is still not fully understood. This will be largely discussed throughout this thesis, in particular in Chapter 4. In most cases, careful dynamical modeling and additional follow-up is required to confirm the hypothesis and to constrain the mass and period of the possible perturber(s). As stressed out by Meschiari & Laughlin (2010) and Payne & Ford (2011), photometric TTVs and RVs are highly complementary in breaking degeneracies that are common in the inverse dynamical problem. The *inversion problem* (that is, deriving the properties of the perturbers from the observed $O-C$ diagram) is particularly tricky when dealing with non-transiting, non RV-detected perturbers. Among others, Meschiari & Laughlin (2010), Boué et al. (2012), and Veras et al. (2011) discussed how to deal with degeneracies and other issues arising during the inversion procedure.

From a heuristic point of view, the first step of a TTV detection is the finding of a particular periodicity in the $O-C$ diagram. Several techniques are able to deal with irregularly sampled data with nonuniform weights, and minimize aliasing effects due to the window function: for example the Generalised Lomb-Scargle periodogram (GLS; Zechmeister & Kürster 2009) and the "Fast χ^2" algorithm (Fχ^2; Palmer 2009). It is worth noting that Veras et al. (2011) demonstrated that some orbital configurations, especially close to (but not exactly in) mean-motion resonances, can induce quasi-periodic or even chaotic TTVs. In other non-exotic configurations, the periodicity would manifest itself only at time scales > 10 yr (Veras et al. 2011). Also when more than one perturber is present and their orbital periods are not commensurable, as in the case of our inner Solar System, the resulting TTV would be in general aperiodic (Holman & Murray 2005). We will face this problem in Chapter 4, where a possible non-periodic TTV is measured.

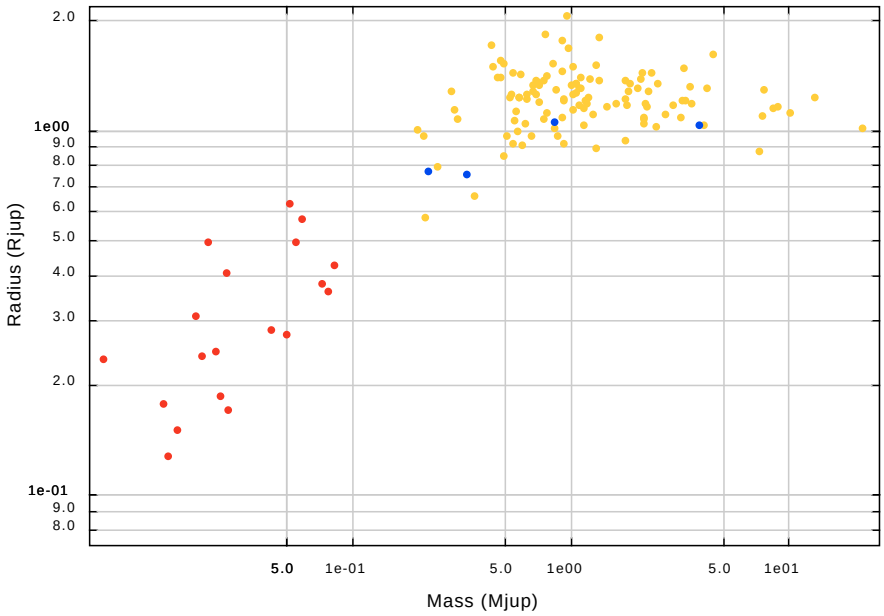

Figure 4: Known exoplanets in the planetary radius R_p/R_{jup} vs. *projected* planetary mass $(M_p \sin i)/M_{jup}$ plane. Points are color-coded according to planetary class: low-mass planets (red, $M_p < 30M_\oplus$), "hot giants" (yellow, $M_p > 30M_\oplus$, $P < 10$ days), "cool giants" (blue, $M_p > 30M_\oplus$, $P > 10$ days). Updated: May 2012.

2

DESIGN AND IMPLEMENTATION OF THE TASTE PROJECT

In this chapter I will describe the design and implementation of the TASTE project, as originally conceived to be operated at one single facility (the 1.82m telescope at the Asiago Observatory). I will discuss the technical requirements, the criteria adopted for the selection of the target sample, the observing strategy, and the first version of the STARSKY pipeline, optimized to carry out differential photometry on defocused images. I will present the first two light curves of the "hot Jupiters" HAT-P-3b and HAT-P-14b gathered by TASTE, and demonstrate that they achieve the accuracy required to detect Earth-mass perturbers through TTVs, if locked on low-order orbital resonances such as 3:2 or 2:1.

This chapter is based on: V. Nascimbeni, G. Piotto, L. R. Bedin, M. Damasso (2011) *TASTE: The Asiago Search for Transit timing variations of Exoplanets. I. Overview and improved parameters for HAT-P-3b and HAT-P-14b*, A&A, 527, A85.

2.1 INTRODUCTION

Among the techniques developed to discover exoplanets, the photometric transit method is one of the most promising having already discovered more than 100 planets. Transits also give us the unique opportunity of a nearly complete characterization of an extrasolar planetary system, by measuring orbital and physical parameters that would otherwise be inaccessible: the planetary radius R_p, the orbital inclination i, the "real" planetary mass M_p (which cannot be provided by the radial velocities alone), and hence the average density (ρ_p).

The great opportunities provided by transits however exist with some disadvantages. In order to obtain a light curve of a typical target with a significant signal-to-noise ratio (S/N), an extremely high photometric precision needs to be reached and sustained for several hours. Many systematic trends can arise from various sources. Known as *correlated* or *red noise*, this effect plagues to a variable extent the ground-based photometry in particular (Pont et al. 2006) and specific techniques have been developed to deal with it (e.g., Tamuz et al. 2005). The simultaneous requirement of both precision and stability makes a sub-millimagnitude light curve a real challenge for ground-based instruments.

In spite of these difficulties, even exoearths might be within the reach of ground-based facilities. Several indirect methods for detecting them have been proposed. One of these is *Transit Time Variation* (TTV) analysis. In principle, a single planet on a Keplerian orbit should be seen to transit at very regular time intervals. However, if there were a second planet (not necessarily transiting) in the same system, it would gravitationally perturbate the orbit of the transiting one, breaking its strict periodicity and varying the measured mid-transit time relative to the expected one (Holman & Murray 2005). The amplitude of the TTV is dependent upon the mass of the perturber (more massive planets leading to a larger effect) and is strongly enhanced if the hidden planet is locked in a low-order orbital resonance with the primary, such as 1:2 or 2:3 (Agol et al. 2005). In that case, even a terrestrial planet could be responsible for a TTV on the order of tens or hundreds of seconds. It should be noted that such resonant orbits have already been detected with the radial velocity (RV) method in some planetary systems (Tinney et al. 2006).

Many ground-based projects about TTV analysis are currently ongoing. The most notable are RISE[1] (Steele et al. 2008), which published null TTV detections of TrES-3b and HAT-P-3b (Gibson et al. 2009, 2010), and The Transit Light Curve Project (Holman et al. 2006). Most of these works use an instrumental setup that is specifically designed to get high-precision light curves with a short cadence, sometimes of a few seconds. A very high sampling rate is required to accurately determine the instant at which the mid-transit occurs. Systematic trends have to be carefully corrected, because they can perturb the light curve from its ideal symmetric shape, biasing the estimated timing and, possibly, mimicking a TTV (Gibson et al. 2009). Despite the efforts of these and other authors, achieving a timing accuracy $\lesssim$10 s is still an ambitious target, typical values ranging from 15 to 30 s for the most accurate published works.

Interestingly, even though five years have elapsed since the first TTV study (Steffen & Agol 2005), no clear evidence has so far been found for a genuine perturbation by a previously unknown planet, although we note that Holman et al. (2010) announced the Kepler discovery of a pair of giant planets orbiting the same star in a 2:1 resonance, and showing an impressive TTV signature (120–240 s). Some ambiguous results have instead been reported for OGLE-TR-111 (Pont et al. 2004; Díaz et al. 2008) and a (yet unconfirmed) claim for WASP-3b (Pollacco et al. 2008) was published by Maciejewski et al. (2010). Perhaps small planets in orbital resonances are less common than previously expected by migration models such as that of Cresswell & Nelson (2006), which would be by itself a significant result. We note that the timing precision reached by most of the earlier studies

1 http://telescope.livjm.ac.uk/Info/TelInst/Inst/RISE/

was around 50–100 s, and that the effects of red noise were then more poorly understood than they are today.

Compared to TTV, *Transit Duration Variation* (TDV) analysis is a more recently developed method, whose theory is more subtle. A periodic change in the transit duration may arise from the presence of a satellite, or *exomoon*, which makes the planet oscillate around the planet-satellite barycenter along its path (Kipping 2009a); in addition, a periodic TTV signal is expected for the same reason. Here TTV and TDV are strictly complementary: a $\pi/2$ phase difference between the two signals is the expected distinctive signature of an exomoon, and the ratio of their amplitudes allows the satellite mass and its distance from the planet to be determined separately (Kipping 2009b). For the most part, timing surveys are focused only on the TTV. A tricky problem in determining the duration is that it is very dependent upon the limb darkening (LD) parameters, which are poorly constrained. Moreover, the LD is wavelength-dependent, making the comparison of TDV data extracted with different instrumental setups prone to systematics.

Our primary aim is to collect a database of high-precision light curves that will be suitable for a simultaneous TTV/TDV analysis, optimizing every task from the observation/calibration setup to the data extraction with fully home-made software tools, optimized for this specific program. Our survey is based on data collected at the Asiago Observatory[2]. Some feasibility tests were also performed at the Osservatorio Astronomico della regione autonoma Valle d'Aosta[3] (OAVdA) observatory, which hosts a 0.81m telescope as its main instrument. Once the necessary fine tuning are completed, it will be useful as an auxiliary facility for our program, improving the efficiency of our survey.

In this first paper of this series, we present preliminary results, describing in detail: the strategy, facility, observations, data reduction, and analysis. We demonstrate that —even at this early stage— our photometry and time resolution are competitive compared with those derived by instruments of the same class. Two targets of our survey are shown as examples, and we present improved orbital and physical parameters of the recently discovered HAT-P-14b (Torres et al. 2010) and of HAT-P-3 (Torres et al. 2007), based on our new data.

2.2 TARGET SELECTION

For each studied exoplanet, a TTV/TDV analysis requires the construction of a homogeneous database of photometric high-precision light curves (RMS: ~1 mmag), all calibrated in time, at a high-accuracy level ($\lesssim$1 s). Thus, it is necessary to perform a careful selection of the

2 http://www.pd.astro.it/asiago/

3 http://www.oavda.it/

Table 1: The selected sample of targets for the TASTE project, and their parameters.

name	M_p/M_J	R_p/R_J	P (d)	dur (min)	i (°)	RA	DEC	V	depth	$TTV_{2:1}$ (s)	TTV_m (s)	V-TDV_m (s)	T-TDV_m (s)
WASP-11	0.46	1.05	3.72	159	88.50	030929	+304025	11.9	0.018	485	4.13	8.17	0.06
HAT-P-9	0.78	1.40	3.92	206	86.50	072040	+370826	12.3	0.012	302	2.67	6.43	0.18
XO-5	1.08	1.09	4.19	193	86.80	074652	+390541	12.1	0.011	234	2.59	5.51	0.17
XO-2	0.57	0.97	2.62	162	88.58	074807	+501333	11.2	0.011	276	2.38	6.81	0.02
HAT-P-13	0.85	1.28	2.92	194	83.40	083932	+472107	10.6	0.007	206	1.89	5.80	0.35
HAT-P-3	0.60	0.89	2.90	123	87.24	134423	+480143	11.9	0.012	291	2.60	5.10	0.12
HAT-P-12	0.21	0.96	3.21	140	90.00	135734	+432937	12.8	0.020	906	6.22	12.54	0.00
HAT-P-14	2.23	1.15	4.63	131	83.50	172028	+381432	9.98	0.006	125	1.52	1.99	1.23
HAT-P-5	1.06	1.26	2.79	175	86.75	181737	+363718	12.0	0.012	158	1.59	4.61	0.08
WASP-3	1.76	1.31	1.85	137	85.06	183432	+353942	10.6	0.011	63	0.74	2.52	0.05
HAT-P-1	0.52	1.23	4.47	160	86.28	225747	+384030	10.4	0.013	511	4.10	6.77	0.41
HAT-P-6	1.06	1.33	3.85	203	85.51	233906	+422758	10.5	0.009	219	2.13	5.16	0.22

The first ten columns give the name of the target, the planet mass M_p and radius R_p (both in jovian units), the orbital period P (in days), the transit duration (in minutes), the orbital inclination i (in degrees), the 2000.0 RA and DEC, the V magnitude of the host star, the transit depth (in flux). In the last four columns, we reported the expected TTV & TDV effects in seconds caused by a 1 $M_\oplus$ exoplanet in a 2:1 resonant external orbit ($TTV_{2:1}$) and to a 1 $M_\oplus$ exomoon at one third of the Hill radius (TTV_m and the V- and TIP- components of the TDV_m).

targets, based on both observational and physical criteria. Among the 81 transiting exoplanets known at the time of the submission (`exoplanet.eu` database), we assigned a rating to each candidate by taking into account the following observational constraints:

- declination $\delta > +0°$;
- magnitude of the host star $9 < V < 13$;
- orbital period $P \lesssim 5$ days;
- total duration $d \lesssim 200$ minutes;
- transit depth $\gtrsim 5$ mmag;
- the presence of suitable reference star(s) within the field of view of our detectors.

As demonstrated by our tests on the Asiago 1.82m telescope, this first set of requirements gives us the chance to collect each season a reasonable number of full transits with a high sampling rate and a high S/N.

Targets lying within the CoRoT or Kepler fields were excluded; targets discovered more than four years ago, or for which accurate TTV/TDV studies have been already published, were assigned a lower ranking. The last two criteria take into account the probability of a large TTV/TDV effect (both periodic or secular) being detected by space missions or previous ground-base studies. In addition, we evaluated other factors specific to the detectability of the TTV/TDV signal:

- the computed $TTV_{2:1}$ effect induced by a 1 $M_\oplus$ exoplanet in a 2:1 resonant external orbit (Agol et al. 2005);
- the computed TTV_m effect induced by a 1 $M_\oplus$ exomoon at one third of the Hill radius (Kipping 2009a), which can be conservatively assumed to be the allowed region for a stable satellite;
- the computed TDV_m effect induced by the same exomoon, for both the V (velocity change) and the TIP (impact parameter) components of the perturbation discussed by Kipping (2009b).

Targets with $TTV_{2:1} < 30$ s were excluded. Among the remainder, a higher priority was set for targets with a total $TDV_m > 5$ s. We briefly discuss in Section 2.5.5 how a TTV/TDV signal will be detected.

Finally, a sample of twelve exoplanets was selected. The list sorted in order of RA, along with a summary of their parameters can be seen in Table 1. Few targets were added to the list, as backup choices or because of their interesting properties, though they do not fully comply with the selection criteria. For instance, HAT-P-14b is quite a massive planet, but its highly "grazing" configuration makes it very

sensitive to changes in the transit duration. On the other hand, two targets were included because a TTV is expected by previous studies: the above-mentioned WASP-3b and HAT-P-13b, for which a TTV is predicted by the perturbation of a known – but non-transiting – outer planet (Bakos et al. 2009).

2.3 INSTRUMENTAL SETUP AND OBSERVATIONAL STRATEGY

The facility used for the present work is the Asiago Astrophysical Observatory, located at Mount Ekar (elevation: 1366 m) in northern Italy. Its 1.82m Cassegrain is the largest optical telescope within Italian territory.

The instrument for imaging at the 1.82m is the Asiago Faint Object Spectrograph and Camera (AFOSC), a focal-reducer type camera. Its $8.5' \times 8.5'$ field of view is large enough to allow a careful selection of the stars to be used as reference sources in differential photometry. When used as an imager, AFOSC is equipped with a set of standard Bessel UBVR filters, and a Gunn i filter.

The CCD detector was recently upgraded, by installing a 2k×2k pixels thinned, back-illuminated E2V 42-20, which provides a ~90% quantum efficiency in the R band spectral region. Its pixel size implies a $0.26''$/pixel scale, which severely oversamples the stellar profiles considering the typical seeing of the site. Despite the thermoelectrical cooling, usually set at -60 °C, the measured dark current is quite low, peaking at 0.2 e^-/s/pix in the hottest regions. The cosmetics are very good, with only a bad column starting from a hot pixel group. The 500 MHz read-out mode provides a 2.7 e^-/ADU gain and a ~7.6 e^- read-out noise (RON), which may seem quite high compared to the current standards but does not represent an obstacle for our project because it is in a shot-noise (and scintillation-) limited regime (as we later illustrate).

The camera controller software has been customized to meet our needs for a very high sampling rate. Binning factors of up to 4×4 are available, which help us to lower the readout time while at the same time decreasing the readout noise. For the same reason, sub-windowing is used when only a part of the field is necessary to image a suitable set of reference stars. Significant effort has been devoted to shortening as much as possible the dead technical time between consecutive frames. The total overhead is now 3.4 s when reading a full frame, and 2.2 s for one quarter of a 1024×1024 frame. This performance allows us to achieve a sampling of about 7 s and 5 s, respectively, while keeping a duty-cycle >50%.

We ran tests of the accuracy of the mechanical shutter. For exposures as short as 1s, the effective integration time is repeatable to within 0.05 s and the travel time is regular to about two parts in 10^4, allowing sub-millimagnitude photometry. However, we do not wish

to reach such short exposures, since the duty-cycle would get very low (<20%) and a non-negligible fraction of the overall S/N of our light curve would be lost, nullifying the advantages of a fast sampling. When a target is too bright to be imaged with $\geqslant 2$ s exposures, we choose instead to apply a slight defocus to avoid saturation. The defocusing technique also minimizes systematic errors caused by a non-perfect flat field correction (Southworth et al. 2009a,b). The 1.82m autoguide is not accurate enough to keep the stars on the same physical pixel during the whole series, but our data analysis will take into account the motion of the centroids as a possible source of systematic errors.

Only a good *pre-reduction strategy* would guarantee the extremely precise photometry required by the goals of the project, and much of the efforts are devoted to this task. Even very small instrumental drifts (over a timescale of just a few hours) could easily reach amplitudes of a few mmag. Bias, dark, and flat-field frames are taken just before and after the photometric series. In this way, at the data-reduction stage it becomes possible to linearly interpolate between the pre- and post- master-bias, -flats, and -darks to "customize" the calibration frames for each individual scientific frame of the time series. The master-bias, master-flat, and master-dark frames collected on each night are also stored for a long-term calibration analysis, in order to highlight any change or drift that may be correlated with seasonal trends (such as temperature) or the detector decay (cosmetics).

Even when taking the greatest care, smooth gradients on the order of $\lesssim$5% are evident when comparing dome flats with a more accurate sky flat. Therefore, sky flats, taken at both the sunset and dawn twilights and then interpolated, provide a more effective means of flat-fielding our data. Dome flats are taken in any case, not only as a backup means of performing the flat-field calibration, but also to check for short-period variations in sensitivity. Even when dealing with the highest quality flats, accuracy at low spatial frequencies is challenged by "sky concentration", tipically affecting focal reducers (Andersen et al. 1995) where scattered light is directed preferentially at the center of the field. As we later show, a very smooth gradient is not a problem as long as the tracking drifts are carefully monitored and constrained to within a few pixels.

2.4 OBSERVATIONS

After a tuning phase that lasted some months mostly involving hardware/software tests and closed-dome calibrations, the first scientific observations on real transits were performed in February 2010, namely for XO-3b (Johns-Krull et al. 2008) on 2010 February 13, and WASP-12b (Hebb et al. 2009) on 2010 February 14[4]. In both cases, clouds and

4 Dates for the observing nights are reported as "evening dates".

Table 2: Summary of the observed transits at the 1.82m Asiago telescope.

target	date	UT obs. time	airmass	filter	exptime (s)	sampling (s)	frames	notes
XO-3	2010 Feb 13	19:03—22:08	1.05—1.29	R	2, 1.5, 1	5—6	2238	partial, clouds
WASP-12	2010 Feb 14	20:36—23.59	1.04—1.28	R	2, 1.5	5—6	2310	partial
HAT-P-14	2010 Mar 12	01:25—04:53	1.34—1.01	R	2	5.4	2247	complete
HAT-P-3	2010 Apr 07	23:23—03:31	1.00—1.24	R	2	5.0	2882	complete

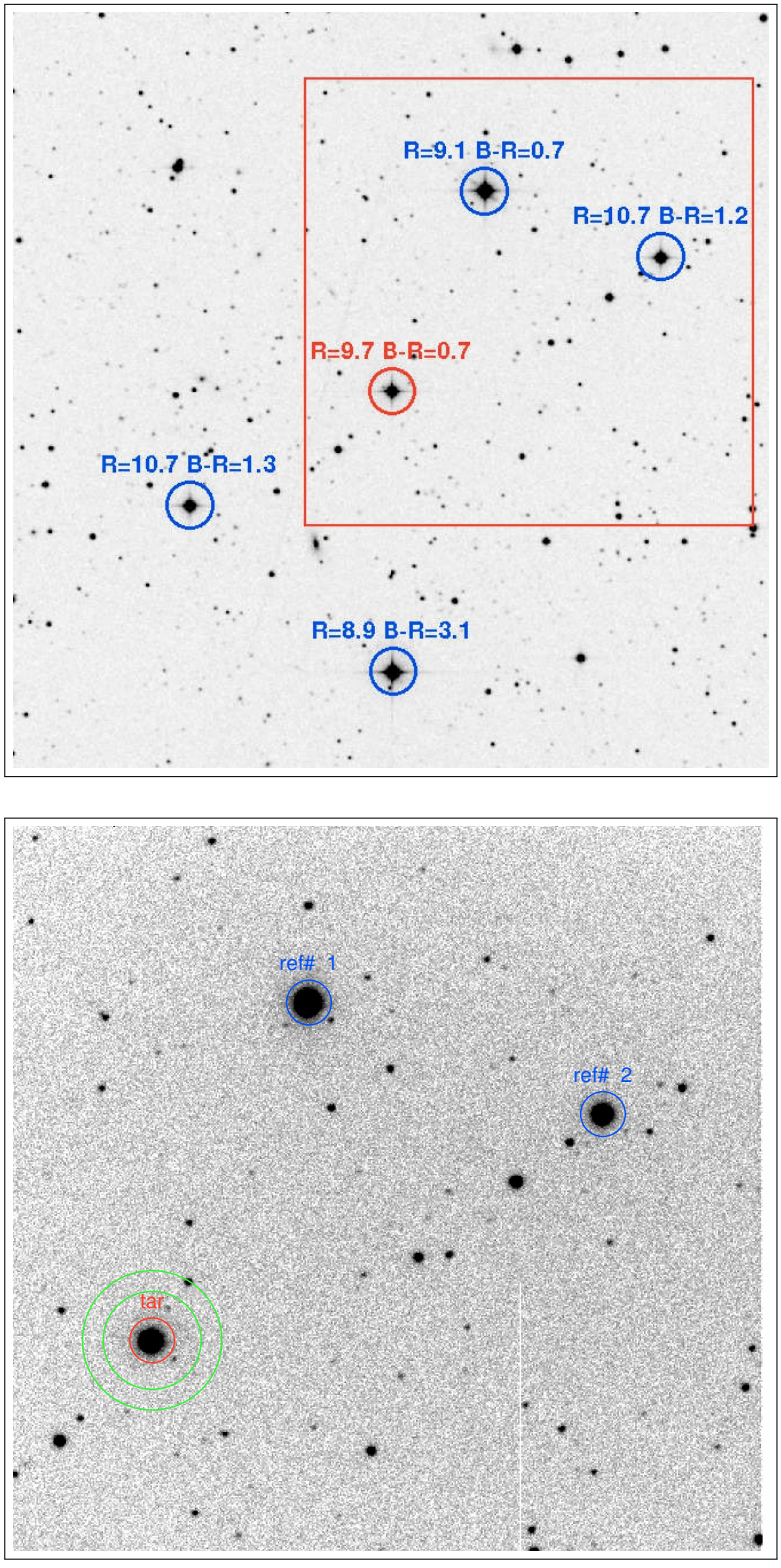

Figure 5: (*Upper panel*): A $15' \times 15'$ image from PSS2-red centered on HAT-P-14 (red circle) North is up, East is to the left. For reference, the blue circles highlight the brightest stars in the field (corresponding numbers give their R magnitude and $B - R$ color). The AFOSC full-frame FOV (red square) is also shown. (*Lower panel*): Example of the typical image quality obtained with AFOSC on a 2 s single frame during the 2010 Mar 12 run. The two main reference stars are marked with blue circles. The two green circles indicate the annulus within which the local sky was estimated.

high humidity prevented a full transit from being monitored. However, a data analysis of that light curves revealed some problems (such as dome turbulence, hardware/software bugs) for which later countermeasures were taken. All the observations reported here were carried out with the AFOSC R filter. The log of the observations shown in Table 2.

The first complete light curve was measured for HAT-P-14b on the night of 2010 March 12. HAT-P-14b is a "hot Jupiter" discovered by Torres et al. (2010), orbiting a slightly evolved F dwarf ($V = 9.98$). This planet is more massive and eccentric than the average of its class. In addition, its grazing inclination generates a V-shaped light curve, which differs from the usual U-shaped ones. That transit was the first one available, just 24 h after its publication, with an ingress and egress time predicted by Torres et al. (2010) at 2:16 and 4:28 UT of 2010 March 12. A $V = 9.39$ reference star lies $4.4'$ from HAT-P-14. The reference star has a color very similar to the target. We chose the full-frame readout in order to include a third $V = 10.53$ star to be used as a cross-check source. They are labeled #1 and #2 in the finding chart of Fig. 5, respectively. The sky was photometric during the entire series. Astronomical twilight was expected at 3:51 UT, but observations lasted until the autoguide was possible, at nearly the end of the nautical twilight. The series was stopped at 4:54 UT after 200 min without interruptions; 2247 frames (in 4×4-binning mode) were collected. A high but quite stable seeing (~$2.5''$) and a slight defocusing allowed for constant 2 s exposure times and a 37% duty-cycle. In addition to the dome flats, twilight flats were taken at dawn.

Finally, a complete transit of HAT-P-3b was observed during the night of 2010 April 7. HAT-P-3 is a $V = 11.86$ K dwarf, which hosts a quite light (0.60 M_J) transiting hot Jupiter with a short period of $P \sim 2.9$ days (Torres et al. 2007). The transit of HAT-P-3b exhibits a depth that is twice as large (0.013 mag) as that of HAT-P-14b. The field is very poor, allowing only one star with a significant flux ($V \sim 10.9$) and a $B - R$ color not too different from that of the target (1.4 versus 0.8), at about $6.8'$. To reduce our overhead, we chose to read only a 90×500 pixel CCD window (4×4 binned). Seeing was excellent (FWHM $\lesssim 1''$), so stars were defocused at about $2''$ FWHM to prevent saturation of the brighter one. A full time-series covering 70 min of pre-ingress and 60 min of post-egress was taken, with a constant 5 s time sampling. The focus had be adjusted twice during the series, because of the slow thermal expansion of the secondary mirror. In the end, 2882 frames were collected, with an overall duty-cycle of 40%.

2.5 DATA REDUCTION AND ANALYSIS

To mantain full control of the error budget and extract the maximal amount of information from the available data, we implemented

and used independent software tools specifically developed for this project. The resulting pipeline, coded in Fortan 77/90 for the most part, is usable but still in active development. As a crosscheck, its output is frequently compared with that obtained using other publicly available softwares.

The key concept of our pipeline is the use of a fully empirical approach to perform every task, from the pre-processing, passing through the light curve extraction, to the estimate of the transit parameters along with their associated errors. We care about keeping our code as flexible as possible, so that future data sets coming from a different instrumental setup could be treated with minimal changes.

2.5.1 *Aperture photometry with* STARSKY

For our typical observing conditions (highly variable PSF due to seeing and defocus, lack of stellar crowding), the method of choice is differential aperture photometry, which allows us to normalize the flux of the target with a "reference flux" constructed by combining one or more reference stars. Given the small size of our field, this differential measure automatically cancels out first-order systematic trends, such as transparency variations. We carry out this task with a code named STARSKY. The final aim of our empirical approach is to obtain a light curve whose *measured* scatter is as small as possible.

Each frame is calibrated using the supplied master-bias, -flat, and -dark. These master frames are linearly interpolated when two given epochs (before and after the observations) are available, accordingly to our pre-reduction strategy. A precise centroid and an estimate of the FWHM of the stellar profiles is then computed by a Gaussian fit for each target or reference star in an input list. The sky level is estimated over an annulus either as a k-σ clipped median or by fitting a plane with an iterative k-σ rejection. The k factor is tunable, $k = 3$ usually being the best choice. The annuli are dynamically adjusted for each frame i by multiplying the input values of the inner and outer radii by the quantity $B_i/\langle B_i \rangle$, that is the mean FWHM of the profiles, normalized by its median over the full time-series.

After the sky is subtracted, fluxes are evaluated by summation over a set of user-defined circular apertures; partial pixels are handled by numerical integration of the fraction of pixel area falling inside a given aperture. We considered "optimal" extraction (Naylor et al. 1998) as a possible alternative to classical aperture photometry, but the high spatial variability of the PSF prevented us from such a choice. Anyway, the advantages of that approach would have been partly nullified by the very low contribution of the background noise to the typical S/N of our sources.

The expected total noise for each source is given theoretically by Merline & Howell (1995) as

$$\sigma = \frac{1}{N_\star}\sqrt{N_\star + n_{pix}\left(1+\frac{n_{pix}}{n_B}\right)\left(N_S + N_D + N_R^2\right) + \sigma_s^2} \quad , \tag{9}$$

where $N_\star$ is the total number of photons collected from the star, and N_S, N_D, and N_R the average photons per pixel coming from the sky, the dark current, and the readout noise, respectively. These quantities are assumed to have been estimated over an aperture covering n_{pix} pixels and the sky over an annulus covering n_B pixels. The σ_s term is the contribution from the atmospheric scintillation, given by Dravins et al. (1998) as

$$\sigma_s = 0.09\, N_\star \frac{X^{3/2}}{D^{2/3}\sqrt{2t}} \exp\left(-\frac{h}{8}\right) \quad , \tag{10}$$

where X is the airmass, D the diameter of the telescope in cm, t the exposure time in s, h the observatory altitude in km. In the typical observing conditions that we have to deal with (bright targets, short exposures, almost negligible dark current), the noise budget is largely dominated by photon "shot" noise and scintillation. Figure 6 shows how, in typical conditions, scintillation is dominant for bright targets ($R \lesssim 11$), while shot noise is dominant for faint targets ($R \gtrsim 11$). Readout noise is nearly negligible in our magnitude range.

Once we compute the "absolute" fluxes of each source along with the associated expected errors, we need to combine the flux from the reference stars to be used as optimal "reference flux" for our differential photometry. For each reference star i of flux F_i —and for each image— we chose to calculate the reference flux F_i^0 as the weighted mean of the instrumental magnitudes of all the other reference stars $F_{j\neq i}$. This averaging technique was proven to be formally correct by Broeg et al. (2005). During the first iteration, the weights $w_i = 1/\sigma_i^2$ are set according to the expected amount of noise given by Eq. (9). A differential light curve is constructed by normalizing the raw flux F_i to the reference flux F_i^0. The scatter $\tilde{\sigma}_i$ of each differential light curve is estimated as the 68.27^{th} percentile of the residuals from its median value, after the outliers have been rejected with an iterative 4-σ clipping algorithm. Then we iterate the process of re-evaluating the reference flux F_i^0 by using this time the *measured* scatters $\tilde{\sigma}_i$ for the weights w_i, constructing a new differential light curve F_i/F_i^0, and so forth, until convergence is reached.

To detect possible systematic trends or intrinsic variability among the reference stars, two diagnostics are computed for each light curve:

- `dsys`, the ratio $\tilde{\sigma}_i/\sigma_i$ of the measured photometric scatter to the expected amount of noise given by Eq. (9).

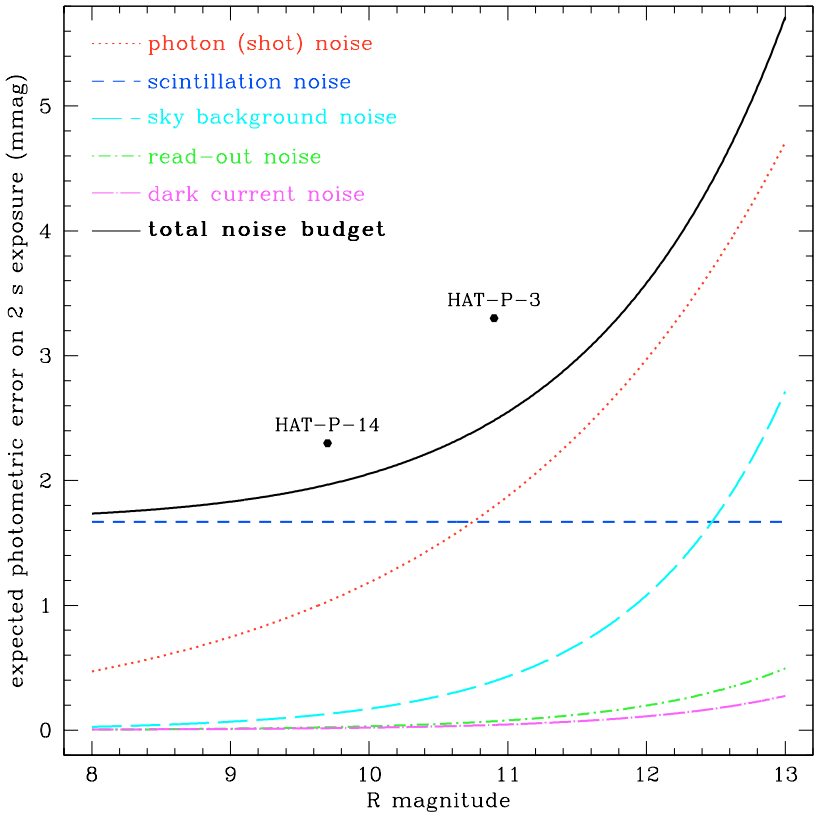

Figure 6: Expected noise budget in mmag of a single 2 s exposure taken at the Asiago 1.82m telescope under typical observing conditions (4×4 binning, airmass 1.2, 7″ aperture), as function of the R magnitude of the target. Measured off-transit scatters are shown for the observed light curves of HAT-P-14 and HAT-P-3.

- psys, the ratio of the $\tilde{\sigma}_i$ to the same scatter measured after a low-order polynomial (whose degree is user-defined) has been fitted and subtracted from the whole light curve.

In the ideal case, i.e. without systematics and unknown sources of random errors, we would get $\texttt{dsys} = \texttt{psys} = 1$. A situation in which $\texttt{dsys} \gg 1$, $\texttt{psys} \simeq 1$ is indicative of short-period systematics and/or an underestimated budget noise, while $\texttt{psys} \gg 1$ reveals long-term systematic trends (as these might also depend, for example, on airmasses). For the initial set of reference stars, the reference flux $F_\star^0$ is computed by combining all their fluxes and used to normalize the light curve of the target $F_\star$, and the off-transit scatter $\tilde{\sigma}_\star$ is then evaluated. The reference star(s) with the highest values of dsys and psys are removed from the list of the valid reference stars and $F_\star^0$ is re-evaluated without them, to check whether the off-transit measured $\tilde{\sigma}_\star$ decreases. If so, dsys and psys are calculated for the remaining reference stars and a new selection is done, iterating until $\tilde{\sigma}_\star$ is minimized. Given the small number of reference stars in our fields, each light curve is visually inspected to search for unexpected behaviour.

We incorporate an additional routine to perform empirical systematic correction. We search for orrelations between the fluxes F_i/F_i^0 and relevant quantities such as airmass, (x,y) centroid positions, FWHM of the stellar profiles and other relevant parameters, which we then fit with low-order polynomials and subtract. A systematic correction is again considered effective if the out-of-transit $\tilde{\sigma}_\star$ decreases when it is applied. A further cross-check is performed by sorting the stars by their $B - R$ colors to see whether dsys and psys are higher for stars bluer or redder than average, as we would expect in the case of color-dependent systematics.

Finally the light curve of the target is normalized to one by dividing it by its off-transit median flux, after a 4-σ iterative clipping, as explained above. The error bar associated with each photometric point is assigned in this way: the expected noise for all the stars is computed using Eq. (9), the error is then propagated to the reference flux for the target $F_\star^0$ and to the differential flux $F_\star/F_\star^0$. This is an important step, because often the error in the estimate of the reference flux is not negligible when compared with that on the raw flux of the target, especially when dealing with faint and/or an insufficient number of reference stars. Neglecting the uncertainities in the reference sources, indeed, ensures that σ in Eq. (9) is underestimated. The presence of red noise would also lead to an underestimated σ.

2.5.2 *Light curve fitting*

To extract the best estimate of the transit parameters, we need to fit a suitable model to our light curves. The details of the fitting process can appreciably affect the results. It is even trickier to obtain a real-

istic estimate of the errors in the fitted quantities, i.e. taking into account the role played by systematic errors and input parameters that must be held fixed at a constant value (above all, the limb darkening coefficients). All the light curves in this work were fitted with the JKTEBOP code[5] (Southworth et al. 2004), which was originally developed for the analysis of detached binary systems, of which planetary transits are a special case; it has already been used in several works about high-precision transit photometry (Southworth 2008) and also specifically for TTV analysis (Coughlin et al. 2008). The package models the two components of the system as biaxial ellipsoids and performs a numerical integration in concentric annuli over the surface of each component to estimate the flux coming from the system. It then fits the model to the data with a Levenberg-Marquardt (L–M) least squares algorithm. We chose JKTEBOP among other commonly used modeling/fitting algorithms (such as those based on the analytic light curves from Mandel & Agol 2002) because it does not rely on small/spherical planet approximations, it converges rapidly toward a reliable solution (Giménez 2006), minimizes the correlation between the fitted parameters (Southworth 2008) and includes several routines for the estimation of realistic errors.

JKTEBOP can compute the limb darkening (LD) effect with several different non-linear laws, as a simple linear dependence has been proven to be not accurate enough when dealing with high precision light curves (Southworth et al. 2007). We chose to use a quadratic LD law, labeling with u_1 the linear term and u_2 the quadratic term. These two quantities are strongly correlated and therefore difficult to fit simultaneously; we instead usually fix u_2 to its theoretical value, i.e. attempt to find only the u_1 term. In some cases this second strategy may also deliver unphysical results for u_1 (e. g. negative values) and so both u_1 and u_2 have to be fixed. We take the theoretical LD coefficients by interpolating over the grid tabulated by Claret (2000) with the ATLAS model, using the $\log g$, $T_{\rm eff}$, and [M/H] estimated for the host star from the highest quality available spectroscopic follow-up.

Since the internal errors in the L-M fit are known to be too optimistic, JKTEBOP also includes some subroutines to estimate realistic uncertainties in every fitted parameter, using Monte Carlo and bootstrapping methods (Southworth 2008). We chose one of the most conservative approaches, i.e. the uncertainties given by a "prayer bead" empirical algorithm, also known as "residual-permutation" (RP). The RP algorithm evaluates a best-fit solution to the N data points, and the residuals of the fit are then all cyclically shifted to the next data point; a new fit is next found and the new residuals are shifted again, this iteration continuing until the residuals return to the original position (that is, after N fits). The errors are then evaluated based on the final distribution of the fitted parameters. This algorithm auto-

5 http://www.astro.keele.ac.uk/~jkt/codes/jktebop.html

matically takes into account the effects of both red noise and random errors (Jenkins et al. 2002). Its main advantage over the other Monte Carlo Markov Chain and bootstrapping methods is that it propagates over the light curve the photometric features of the *actual* correlated noise, without being sensitive to the choice of an averaging time or to a specific error-rescaling method. We also perform Monte Carlo tests for comparison, to check whether the errors estimated by the two different methods are consistent with each other. In our analysis, we always choose the most conservative error. As shown in the discussion, we performed thorough cross-checks to assess the reliability of the parameters and the associated uncertaintes derived by JKTEBOP.

We have already begun to implement from scratch an independent pipeline that will replace JKTEBOP for our purposes, i.e. following the same flexible and empirical approach that characterizes `STARSKY`. Once completed and tested, it will allow us to perform the entire data reduction and analysis with fully customized and optimized tools.

2.5.3 *HAT-P-14b*

At $V = 9.98$, $R \sim 9.7$, HAT-P-14 is the brightest star in the sample surveyed by TASTE. In our AFOSC field of view, only two stars provide a non-negligible flux compared to the target, and can be chosen as primary reference stars: they are named `ref#1` ($R \sim 9.1$) and `ref#2` ($R \sim 10.7$) in the right panel of Fig. 5. In addition, light curves were extracted for another eleven stars, with $12.8 \lesssim R \lesssim 16$ and $0.6 \lesssim (B-R) \lesssim 2.3$, just to check for systematic errors depending upon colors or upon (x,y) position.

For the inner and outer sky annuli we chose an initial value of 33 and 47 binned pixels, respectively (one 4×4 binned pixel $\simeq 1''$), to be dynamically adapted to each frame as explained in Sec. 2.5.1. The aperture fluxes of the stars were evaluated over 20 different circular apertures, their radii being equally spaced between 4.0 and 20.0 pixels. The two available master-bias (taken just before and after the series) were interpolated for each frame, while flat fielding was performed with a constant master-flat taken at the morning twilight. We verified that dark correction is not necessary – in fact, its sole effect on photometry is to add noise. Measured background levels and raw aperture fluxes confirm that the sky was photometric. The typical gaussian FWHM of the profiles was quite stable through the series at about $2.5''$, because of a mix of atmospheric seeing and slight defocus. The telescope guide drifted slowly and monotonically by about $1.6''$ in 200 minutes, mostly along the RA axis.

The algorithms used for the iterative rejection of the reference stars (described in Section 2.5.1) simplify in this case to only three possible choices: `1`, `1+2`, and `2`. When using `ref#2` as a single reference source, the off-transit light curve of HAT-P-14b shows clear short- and long-

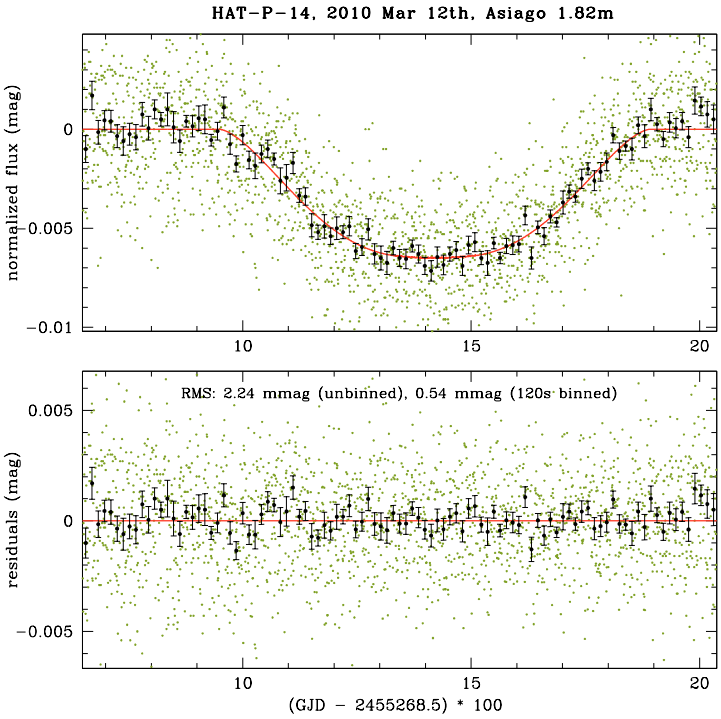

Figure 7: *Top:* Light curve for HAT-P-14b ($V \sim 9.98$, $\Delta V = 0.007$), observed on March 13, 2010 with the Asiago 1.82m. Unbinned points are shown in green and 120s-binned points in black. Off-transit magnitude has been set to zero. *Bottom:* residuals after the best-fit model is subtracted.

term systematic errors, as confirmed by the `dsys` and `psys` diagnostics. The brighter `ref#1` has instead `dsys` $\simeq$ `psys` $\simeq 1$ for most of the aperture sizes. We note that the color $(B-R)_{\#1} = 0.7$ matches exactly the target, while $(B-R)_{\#2} = 1.2$. To summarize, `STARSKY` selected the flux from `ref#1` enclosed by a 7.2 pixel aperture as the best reference flux. The differential light curve obtained for HAT-P-14 is shown with green points in the upper panel of Fig. 7.

Using JKTEBOP, we chose to fit the light curve by fixing both the LD coefficients at their theoretical values of $u_1 = 0.33$ and $u_2 = 0.09$, which were computed assuming the stellar parameters given by Torres et al. (2010) of $T_{\rm eff} = 6600$ K, $v_{\rm mic} = 0.85$ km/s, $\log g = 4.25$, and $[{\rm Fe/H}] = +0.11$. Attempts to fit u_1 failed, as our single light curve does not provide enough S/N for such a shallow transit. As soon as additional time series for HAT-P-14b are collected, a simultaneous fit will allow us to get an empirical estimate for u_1 and u_2.

The final fitted model is plotted as a red line in Fig. 7. When the model is subtracted from the data, the unbinned light curve shows an RMS scatter of 2.2 mmag. Once the points are binned to 120 s (i.e. ~ 22 frames per bin), the scatter decreases to 0.54 mmag, showing only a small amount of red noise. The errors do not show any significant

correlation with airmass, seeing, or positions, therefore no systematic correction was applied. In spite of an increase in the sky level of about two order of magnitudes, the systematics were tightly constrained to within 1 mmag even in the last part of the curve, when twilight occurred. The fitted parameters are reported in Table 3, along with the 1-σ errors estimated by the residual-permutation algorithm.

2.5.4 *HAT-P-3b*

As reported above, the field surrounding HAT-P-3 ($V = 11.86$, $R \sim 10.9$, $B - R = 1.6$) is extremely sparsely populated, containing only one suitable reference star: TYC 3466-1158-1 ($R \sim 10.6$, $B - R = 1.4$). The narrow $1.5' \times 8'$ stripe we analyzed lacks in sources brighter than $R = 17$, leaving us with no other possible reference stars. The inner and outer sky annulus radii were set to 30 and 47 binned pixels, dynamically adjusted throughout the series; we used 20 circular apertures for the star fluxes, equally spaced between 4.0 and 10.0 pixels.

As for HAT-P-14, we interpolated the bias correction for each frame, while a constant master-flat correction was applied, taken at the morning twilight. The sky was photometric; the FWHM of the profiles changed through the series in the range $1.5''$-$2.3''$, because of the afore mentioned thermal focus drift (Sec. 2.4) and the consequent adjustments. At the same time, the shape of the PSFs changed noticeably, becoming asymmetric in the second part of the series. The telescope guide drifted monotonically by about $3.6''$ in 250 minutes, along both axes. Reflecting the change of scale due to the focus adjustments, we noticed a small differential drift, which caused the relative distance between the two main stars to change by about $0.8''$.

TYC 3466-1158-1 turned out to be a good choice, showing no long-term systematic trends (`psys` $\simeq 1$) similar to those expected from differential extinction. However, `dsys` $= 1.24$ indicates that there is a non-negligible level of short-term systematics, probably owing to small pixel-to-pixel residual errors in the flat-field correction, combined with the PSF unpredictable (also spatial-) variability, which led to changes in the photometric zero point. An intrinsic microvariability of TYC 3466-1158-1 is a possible cause that should not be ruled out. In addition, a part of the S/N that would be achievable on HAT-P-3 is inevitably lost because of the paucity of reference flux. `STARSKY` selected 6.1 pixels as the best aperture. The differential light curve obtained for HAT-P-3 is shown with green points in the upper panel of Fig. 8.

The light curve was fitted by fixing both the LD coefficients at their theoretical values $u_1 = 0.47$, $u_2 = 0.24$, which werecomputed assuming the stellar parameters given by Torres et al. (2007) of $T_{\rm eff} = 5185$ K, $v_{\rm mic} = 2.0$ km/s, $\log g = 4.61$, and [Fe/H] $= +0.27$. Attempts to fit u_1 failed, as our single light curve does not provide enough S/N.

Table 3: Fitted parameters for HAT-P-14b (top panel) and HAT-P-3b (bottom panel).

HAT-P-14b planet parameters

	Torres10	This work
P (days)	4.627669 ± 0.000005	4.627682 ± 0.000003
T_c (BJD)	$54{,}875.28938 \pm 0.00047$	$55{,}268.64237 \pm 0.00031$
$R_p/R_\star$	0.0805 ± 0.0015	0.0834 ± 0.0014
b ($a \cos i/R$)	$0.891^{+0.007}_{-0.008}$	0.93 ± 0.03
i (deg)	83.5 ± 0.3	84.21 ± 0.16

HAT-P-3b planet parameters

	Torres07	Gibson10	This work
P (days)	2.899703 ± 0.000054	2.899738 ± 0.000007	2.899737 ± 0.000004
T_c (BJD)	$54{,}218.7594 \pm 0.0029$	$54{,}856.70118 \pm 0.00018$	$55{,}294.56148 \pm 0.00014$
$R_p/R_\star$	$0.1109^{+0.0025}_{-0.0022}$	$0.1098^{+0.0010}_{-0.0012}$	0.1094 ± 0.0011
b ($a \cos i/R$)	$0.51^{+0.11}_{-0.13}$	$0.576^{+0.022}_{-0.033}$	0.574 ± 0.018
i (deg)	87.24 ± 0.69	$86.75^{+0.22}_{-0.21}$	86.75 ± 0.10

The columns show the orbital period P, the central instant of the transit T_c, the ratio of the radii $R_p/R_\star$, the impact parameter b, and the orbital inclination i. Comparison with the previous estimates is given. The reported 1-σ errors are estimated by the residual-permutation algorithm. A constant amount of 2 400 000 has been subtracted from all the BJDs.

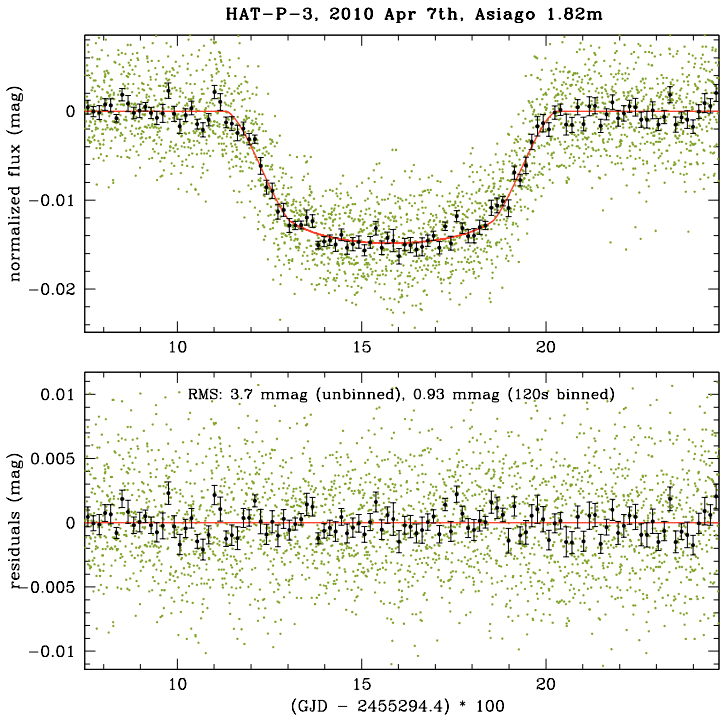

Figure 8: *Top:* Light curve for HAT-P-3b ($V = 11.86$, $\Delta V = 0.013$), observed on April 7, 2010 with the Asiago 1.82m telescope. Unbinned points are shown in green and 120s-binned points in black. Off-transit magnitude has been set to zero. *Bottom:* residuals after the best-fit model is subtracted.

The final fitted model is plotted as a red line in Fig. 8. When the model is subtracted from the data, the unbinned light curve shows an RMS scatter of 3.7 mmag. Once the points are binned to 120 s (i.e. $\sim$ 24 frames per bin), the scatter decreases to 0.93 mmag. Though a small amount of systematic noise was detected, it does not show a significant correlation with airmass, seeing, or positions, therefore no correction was applied. As for HAT-P-14, the increase in the sky level near the end of the series does not cause significant trends: even in the last few minutes, the binned points are well within 2-σ off the model. The fitted parameters are reported in the Table 3, along with the 1-σ errors estimated by the residual-permutation algorithm.

2.5.5 *TTV analysis*

When TASTE begins to accumulate multiple transits for a given target, a search for TTV will be carried out using specially developed software tools, now still at the development stage.

In principle, at least three measurements are needed to detect a TTV. In a "real world case", the signal could be multimodal, noisy, and/or unevenly sampled, and the number of observed points required for a TTV detection is strongly dependent on the signal itself. Previous works (Gibson et al. 2009, among others) have shown that it is risky to rely only on unexpectedly large amounts of scatter in the (O $-$ C) diagrams. The solid detection of a TTV requires instead the identification of periodic structure in the timing residuals. For typical targets, a number of transits between 5 and 10 is sufficient to place very stringent upper limits on the system. The TTV signals of Kepler-9b ($\sim$ 2 min) and Kepler-9c ($\sim$ 4 min) are the only ones detected so far (Holman et al. 2010), which were sampled, respectively, with 6 and 9 observed transits with a timing accuracy of about 80 s (that is, working at S/N$\sim$ 2–3).

If the O $-$ C residuals for a given TASTE target show an anomalous scatter (reduced $\chi^2 \gg 1$), possible periodicities will be searched for by a periodogram, folding the residuals over the significant frequency peaks. Even in the case of null detection, upper limits will be estimated by fitting synthetic TTV signals to our data. These will be calculated by integrating the equations of motion on a grid of eccentricities, masses, and periods of the hypotetical perturber and mapping the χ^2 over the parameter space.

2.6 DISCUSSION

The overall photometric performances of our system met our expectations. The scatter measured in the whole light curve of our targets is in good agreement with the theoretical expected amount of noise, as shown in Fig. 6. This holds both for HAT-P-14 and HAT-P-3, which

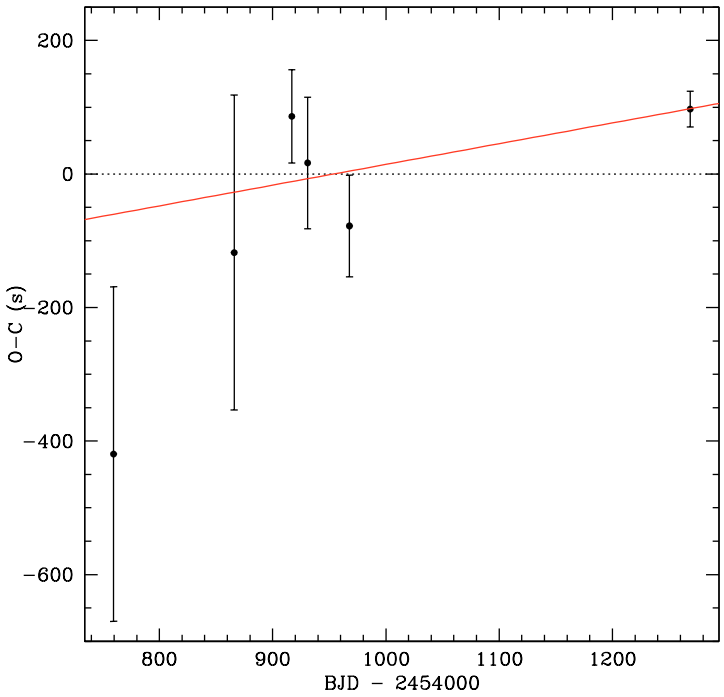

Figure 9: $O-C$ diagram for the central time of the HAT-P-14b transit. The last point is from TASTE (2010, Mar 12), the others from Torres et al. (2010) from which the C ephemeris is taken. The red line is the weighted fit for our refined ephemeris.

are, respectively, the brightest, and close to the faintest magnitude limits of our surveyed sample. In particular, the noise measured for HAT-P-14 ($\sim$ 0.5 mmag on 120 s bins) is indicative of a very small amount of systematic error, and of the same order as achieved by state-of-the-art photometry with medium class telescopes (e.g., see Southworth et al. 2009b, with data acquired in a much better site).

HAT-P-14b was very recently discovered and no specific TTV studies for it have yet been performed. The shallowness and grazing shape of its transit make it one of the most difficult targets in our sample. The $O-C$ diagram (observed minus computed) for the transit central times, relative to the ephemeris published by Torres et al. (2010) is shown in Fig. 9; we plotted the five measurements made by Torres et al. (2010), as well as the first TASTE point. The improvement with respect to the original data and due to our 25 s timing accuracy is remarkable. Because of the better accuracy and the longer than one-year baseline, we were able to improve the ephemeris by using all the weighted available points.

Our best-fit value for the relative radius $R_p/R_\star$ of HAT-P-14b is $\sim$ 4% larger than that reported by Torres et al. (2010), though the two estimates are consistent to within 1-σ. Despite the lower scatter in our light curve, we cannot so far improve the precision in $R_p/R_\star$ over

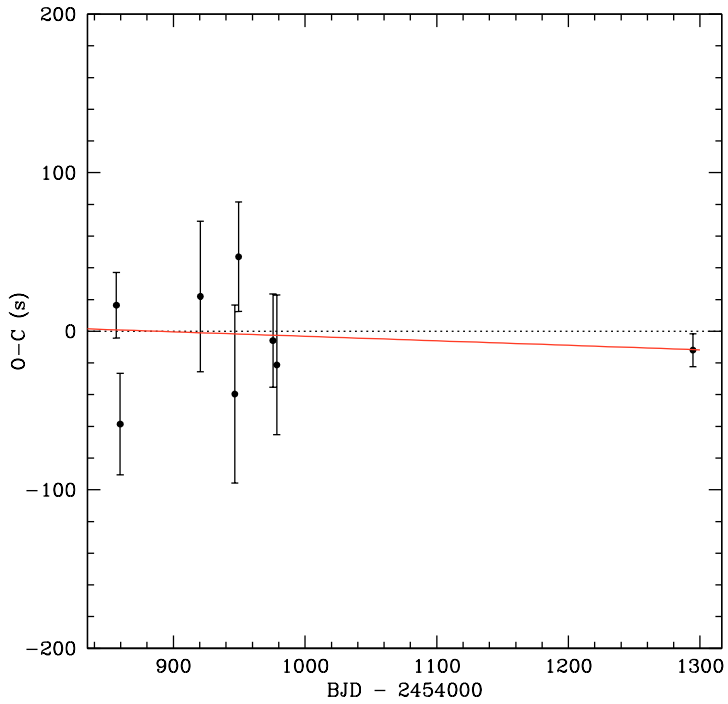

Figure 10: O − C diagram for the central time of the HAT-P-3b transit. The last point is from TASTE (2010, Apr 7), the others from Gibson et al. (2010) from which the C ephemeris is taken. The point by Torres et al. (2007) is omitted. The red line is the weighted fit for our refined ephemeris.

the previous measure, which is based on a simultaneous fit of five transits. We instead refined the other orbital parameters, which are in good agreement with Torres et al. (2010) except for our derived inclination i, which is slightly larger [6].

As for HAT-P-3b, a TTV null detection was found recently, and published by Gibson et al. (2010), placing a constraint on planets with masses higher than 0.33 and 1.81 $M_{\oplus}$ (in inner and outer 2:1 resonances, respectively). The very accurate ephemeris that they calculated (which accumulated only ∼ 90 s of uncertainty at our epoch) allows us to cross-check very strictly the timing accuracy we reached. Our estimated error (∼ 11 s) is smaller by a factor 2–5 than the RISE single measurements. Our measure is indeed well within the range predicted by the previous ephemeris, as can be seen from Fig. 10. Our improved ephemeris is therefore nearly unchanged except for the smaller error on both P and T_c. The other parameters are in excellent agreement with the results by Gibson et al. (2010), with uncertainties that are similar overall.

6 After the submission of the present paper, an additional study of HAT-P-14b appeared on `astro-ph` (Simpson et al. 2010).

To assess the reliability of our analysis, we performed a cross-check by analyzing with JKTEBOP the seven light curves of HAT-P-3b used by Gibson et al. (2010) in their TTV study. We corrected the raw light curves by fitting the out-of-transit flux with a linear function, as described by the authors. We then fixed both the LD quadratic coefficients at the values used in that study and ran JKTEBOP by estimating the errors with the RP algorithm. As an additional test, we also determined the central times by fitting a Mandel & Agol model with a L–M least squares algorithm. The results are shown in Fig. 11, where we plotted the difference between our timings and those published, for each of the seven RISE transits. Our measurements are fully consistent with the results of Gibson et al. (2010), as are the associated error bars. The three transits that display the largest deviation are problematic in various ways (Fig. 12): two are partial transits with a strong variation in scatter during the series (RISE #2, RISE #3), while the third displays clear systematic errors in the out-of-transit part (RISE # 7). Even the highest quality RISE curves (#1, #5), despite their smaller scatter, display an amount of red noise that is larger than that detected on the TASTE transit, as can be seen by binning each curve and comparing the resulting RMS with the one expected by a $\sqrt{t_{exp}}$ scaling law.

2.7 CONCLUSIONS

The primary aim of the TASTE project is to collect a library of high-precision, short-cadence light curves for a selected sample of transits, by performing differential photometry at the Asiago 1.82m telescope. The focus of the project is on the search for TTV and TDV effects induced by other planets (or moons) in the limited number of monitored systems. An important additional advantage is the opportunity to perform a long-term photometric follow-up, leading to an extremely precise characterization of each target, as done e.g. by the TLC project (Holman et al. 2006). By keeping in mind both of the above-mentioned goals, a careful selection of the targets was performed, as described in Section 2.2.

Many improvements are still possible, above all increases in the duty-cycle, which was only $\sim 40\%$ for the two time series that have been presented in this work. Recent tests have demonstrated that, when reading a narrow CCD window, a further reduction of the technical overhead from 3–3.5 s to about 1.6 s is possible. This would lead to a $\gtrsim 70\%$ duty-cycle (for 4 s exposures) for most of our surveyed targets, decreasing the photometric scatter on average by 30–35%. The real-time computing of our photometry will also allow us to perform a nearly-instant correction of the small tracking drifts that we mentioned in Section 2.5, minimizing any residual systematics caused by an imperfect flat-field correction.

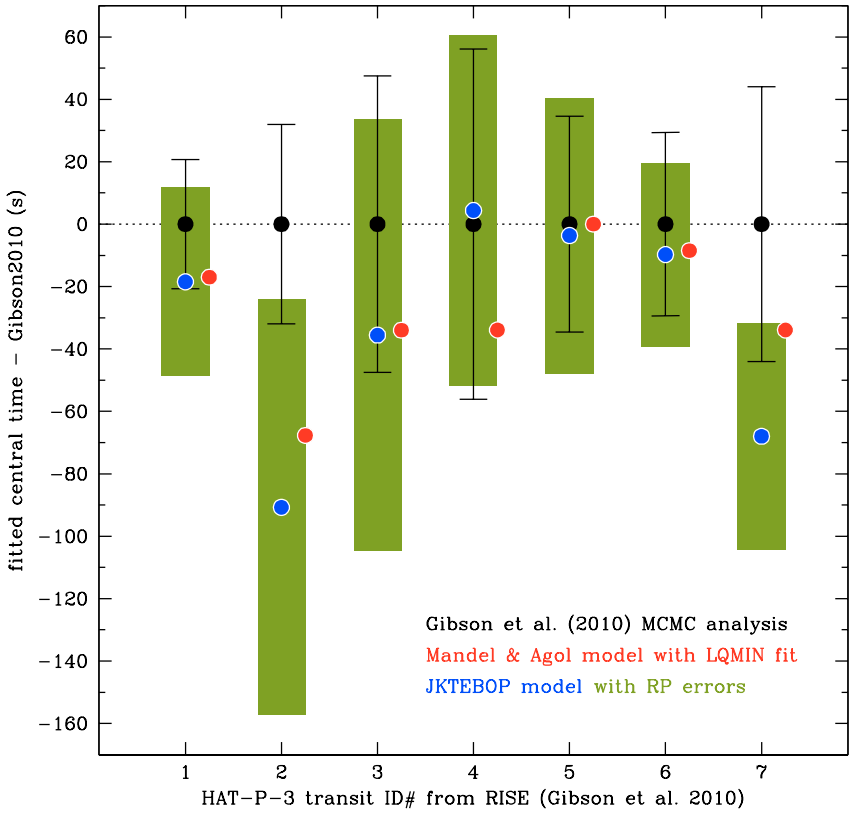

Figure 11: Central times measured on seven light curves of HAT-P-3 collected by Gibson et al. (2010). Comparison between the values published in the original study (black circles and error bars) and those found by our re-analysis with JKTEBOP (blue circles with green error bars from RP algorithm) and a Mandel & Agol model (red circles, slightly displaced on the right for clarity). The numbering of the RISE transits is consistent with Fig. 12.

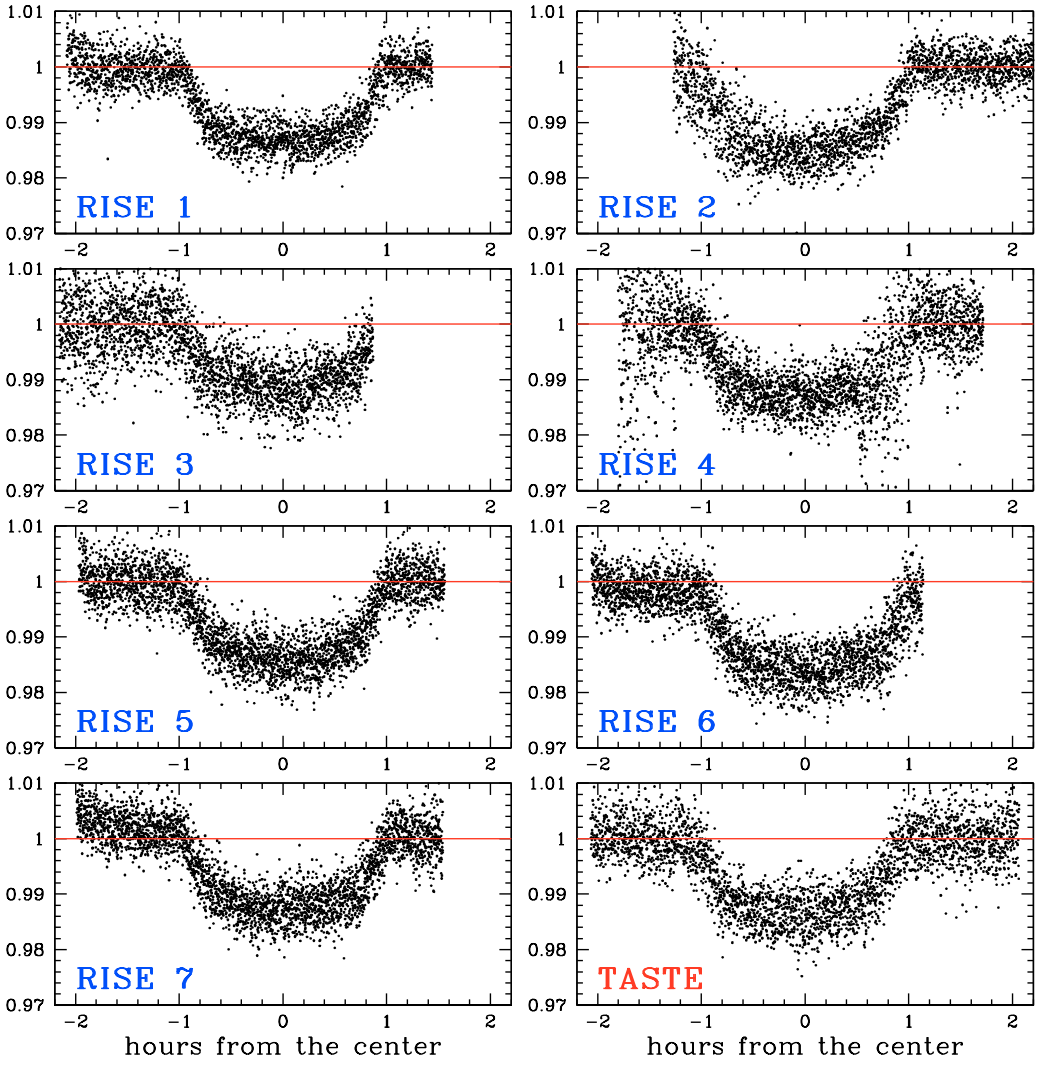

Figure 12: Raw light curves for seven transit of HAT-P-3b by Gibson et al. (2010) (RISE#1, . . . , RISE#7) and the TASTE transit shown in Fig. 8. The light curves are shown in the same scale and without binning.

The fine tuning of our instrumental setup will proceed in step with the additional improvement of our photometric code and the implementation of a brand new independent software tool for the light curve analysis. However, the first results reported here already show the feasibility of our project. We have already began to collect light curves for two targets in our sample (HAT-P-14b and HAT-P-3b), which will define the "zero epoch" of our analysis. In both cases, the achieved photometric precision is very close to the theoretical limits, and the systematics are constrained to well within the millimagnitude. The overall measured scatter is close to that of the present optimal value achievable 1-2 m class telescopes, as obtained by long-cadence photometry on similar targets. The timing accuracy that we have reached, estimated by JKTEBOP algorithms, demonstrates that TASTE is very competitive compared to the performances of other similar projects. With only one transit available for each target, we have been able to derive a refined ephemeris and an independent parameter estimate for both targets.

Acknowledgements

We thank M. Fiaschi for the support in the optimization for our purposes of AFOSC data acquisition software, and L. Malavolta for the night support during the observations of HAT-P-14b and HAT-P-3b.

3

A NEW OBSERVATIONAL STUDY OF HAT-P-13B

In this chapter I will present the first observational TTV study published by the TASTE collaboration. This work was prompted by a paper of Pál et al. (2011), who claimed the detection of a sizeable TTV in the transits of HAT-P-13b (an interesting hot Jupiter hosted by a multiplanetary system). I will show that TASTE data are in agreement with the Pál et al. (2011) measurements, supporting –along with other archival data– the possible presence of a periodic TTV signal. I will point out how subsequent works (Southworth et al. 2012, Fulton et al. 2012) demonstrated that most past timing measurements were published with underestimated errors caused by neglected red noise, thus disproving the previously claimed TTV for this system.

This chapter will be based on: V. Nascimbeni, G. Piotto, L. R. Bedin, M. Damasso, L. Malavolta, L. Borsato (2011) *TASTE II. A new observational study of transit time variations in HAT-P-13b*, A&A, 532, A24.

3.1 INTRODUCTION

Photometric transits represent a great opportunity to discover and characterize extrasolar planets. They are, for instance, the only direct method to estimate the planetary radius and to constrain other important physical and orbital parameters (Winn 2010). In principle, a single planet orbiting the host star in a Keplerian orbit is expected to transit at strictly periodic time intervals, unless it is perturbed by a third body (Holman & Murray 2005). By performing accurate measurements of the central instant time of a known transiting planet, it would be possible to detect deviations from a linear ephemeris, and to infer the parameters of the perturber (Agol et al. 2005). Such a search for other bodies via transit time variations (TTV) is very sensitive to low-mass planets when they are locked in low-order orbital resonances. In these orbits, even earth-mass perturbers would cause TTVs of the order of a few minutes, i.e. easily detectable with ground-based techniques.

In the past few years, some authors have claimed to have detected TTVs using ground-based facilities, for instance from WASP-3b (Maciejewski et al. 2010), WASP-10b (Maciejewski et al. 2011), and WASP-5b (Fukui et al. 2011), though none have been confirmed so far. In contrast, the Kepler mission found undisputable mutual TTVs for the double transiting system Kepler-9b,c (Holman et al. 2010) and for five among six planets transiting on Kepler-11 (Lissauer et al. 2011),

which has lead to the validation of those planets, as well as a deep characterization of their planetary systems.

Pál et al. (2011) claimed to have detected an unusually large TTV in HAT-P-13b. The G4V star HAT-P-13 hosts a multiple planetary system, and was the first multiple system discovered with a transiting planet. HAT-P-13b is a classical "hot jupiter" ($M = 0.85 M_j$, $R = 1.28 R_j$) transiting every $\sim$ 2.91 days, while HAT-P-13c is an outer, massive companion ($M \sin i \sim 15 M_j$, $P = 428.5$ days) detected only with radial velocity (RV) measurements (Bakos et al. 2009). A 2010 multi-site campaign designed to detect the transit of HAT-P-13c yielded a null result with a 65-72% significance level (Szabó et al. 2010). A long-term RV trend of HAT-P-13 was observed by Winn et al. (2010) and interpreted as evidence of a third companion with an even longer orbital period, still to be constrained.

The TTV claimed by Pál et al. (2011) appears to be a sudden deviation of the timings of three transits (by 3.3, 5.5, 8.4 σ) from the linear ephemeris evaluated using the previous data. All the three newly added points are consistent with each other. The "switch" has an amplitude of the order of $\sim$ 0.015 days (Fig. 14, top left panel). This would make it the largest TTV claimed from the ground. The presence of the outer companion HAT-P-3c does not explain such a perturbation, as its expected TTV would have an amplitude of a few seconds and a $\sim$ 430 d period, while the measurements before 2011 are in agreement with a constant ephemeris. An intriguing possibility is that this behaviour is induced by a long-period, massive companion on a very eccentric orbit. Eccentric perturbers are known to cause sudden "spikes" in an otherwise constant $O - C$ diagram (Holman & Murray 2005).

Unfortunately, the available data allow us to constrain the orbital parameters of neither the hypotetical perturber, nor its mass. The transit of HAT-P-13b is shallow ($\Delta m \sim 0.008$ mag) and long ($d \sim 194$ min), i.e. very difficult to monitor. Few measurements were made before 2011, and most with an estimated timing accuracy $\gg 1$ min. Two out of three transits from Pál et al. (2011) show a considerable amount of systematic errors, and one is partial, lacking the egress. Their detection urgently needs a confirmation: if confirmed, efforts should be made to monitor other transits of HAT-P-13b in the near future, to assess the parameters and the nature (substellar or planetary) of the perturber.

In this Paper, we report five new high-precision light curves of HAT-P-13b, observed in January and February 2011 with the Asiago 1.82m telescope. Four of those transits are consecutive, and their estimated timing accuracy is the highest ever achieved for this target. We confirm the deviation with respect to the ephemeris from Szabó et al. (2010) reported by Pál et al. (2011). No ephemeris with a constant period can be fitted to the data with an acceptable χ^2. The observed

Table 4: Summary of the observed transits of HAT-P-13b at the Asiago 1.82m telescope.

eve. date	UT obs. time	airmass	exptime (s)	cadence (s)	duty-cycle	frames	notes
2011 Jan 2	19:46—23:40	1.63—1.03	8	9.7	83%	1451	clouds
2011 Jan 31	23:08—04.18	1.00—1.58	3, 5	6.6	75%	2810	clear
2011 Feb 3	21:07—03:30	1.05—1.00—1.23	5	6.7	75%	2902	some veils
2011 Feb 6	18:53—23:40	1.29—1.00—1.01	4, 5	5.8	71%	2940	clear
2011 Feb 9	17:29—22:31	1.57—1.00	4, 5	6.0	72%	3011	clear, twilight

The columns give: the "evening date" of the observation, the UT time span of the photometric series, the airmass evolution, the exposure time and the average net cadence in s, the overall duty-cycle, the number of frames gathered, and the sky conditions at the time.

deviation is still highly unconstrained. We note that a long-period, sinusoidal TTV can be fitted to the $O-C$ points, with only one significant outlier.

3.2 OBSERVATIONS

All the observations reported here were made as part of the TASTE (The Asiago Search for Transit timing variations of Exoplanets) project (Nascimbeni et al. 2011a). TASTE is collecting high-precision, short-cadence light curves for a selected sample of transiting exoplanets, to discover low-mass planetary companions or exomoons with the TTV/TDV method (transit time/duration variation). We refer to that paper for a detailed description of our instrumental setup, observing strategy, and data reduction/analysis. HAT-P-13b is among the sample we are following.

We collected five transit light curves of HAT-P-13b using the AFOSC imager with its new E2V 42-20 CCD detector mounted at the Asiago 1.82m telescope[1]. An observation log is shown in Table 4. All the observations were made using a standard Cousins R filter and 4×4 binning. We employed binning and windowing to speed up the readout and decrease as much as possible the technical "dead" times between the exposures. We achieved an average $> 70\%$ duty-cycle and a < 10 s net cadence for all our photometric series. We acquired both sky- and dome flat-field frames during each night; bias and dark frames were taken at both the beginning and the end of a light curve to constrain possible instrumental drifts.

Stellar profiles were defocused to $\sim 4-6''$ FWHM (that is, over ~ 1300 physical pixels) in order to minimize systematic errors arising from imperfect flat-field correction, guiding drifts, and pixel-to-pixel inhomogeneity. The $9' \times 2'.6$ CCD window that we read included HAT-P-13 as well as the main reference star TYC 3416-1608-1, a star with a magnitude and colour similar to HAT-P-13 ($V_T = 10.80$ versus (vs.) 10.50 and $B_T - V_T = 0.81$ vs. 0.52).

3.3 DATA REDUCTION AND ANALYSIS

We performed differential aperture photometry on HAT-P-13 using STARSKY (Nascimbeni et al. 2011a), an independent pipeline that we specifically developed for the TASTE project. This code is designed to keep under control any possible source of systematic errors, and implements a fully empirical, iterative approach to identify and correct them. The output light curve is the one with the smallest effective RMS. Specific diagnostics are evaluated at each iteration to constrain the amount of correlated noise. The final, detrended light curves are shown in Fig. 13, both unbinned and binned over 120 s intervals. The

1 http://www.pd.astro.it/asiago/

Table 5: Best-fit values of the central instant T_0 for the five reported new transits of HAT-P-13b.

N_{tr}	BJD T_0 (LS)	BJD T_0 (RP)	ΔT_0+	ΔT_0-
269	2455564.39839	2455564.39892	0.00089	0.00271
279	2455593.56110	2455593.56085	0.00114	0.00115
280	2455596.47625	2455596.47610	0.00299	0.00311
281	2455599.39230	2455599.39252	0.00046	0.00105
282	2455602.31031	2455602.31038	0.00167	0.00166

The columns give: the "event number" N_{tr} for the transit following the ephemeris by Bakos et al. (2009), the central instant of the transit T_0 as estimated by a simple least squares fit (LS) and by the residual-permutation technique (RP), and the associated 1-σ uncertainties ΔT_0 (in days) as given by the RP distribution. BJD times are calculated from UTC.

photometric RMS scatter is in the range $\sigma_u = 1.7 - 2.9$ mmag for the unbinned points and the range $\sigma_{120} = 0.6 - 1.1$ mmag for the 120 s bins. Three of the light curves in Fig. 1 represent the most accurate light curves of HAT-P-13b published so far.

We ran the JKTEBOP code version 25 (Southworth et al. 2004) to fit a transit model over our light curves. We used a quadratic law for limb darkening, fixing both the linear and the quadratic term u_1, u_2 to the theoretical values interpolated from the Claret (2000) tables, for the stellar parameters of HAT-P-13 derived by Bakos et al. (2009). Three of the remaining parameters of the transit (inclination i, ratio, and sum of the fractional radii R_a/R_b, $R_a + R_b$) were estimated by fitting the two highest quality light curves (2011 Jan 3 and Feb 6). We then fixed i, R_a/R_b, $R_a + R_b$ to these respective values, and fitted each individual transit only for the central instant T_0. Since the formal errors derived by the least squares routine are known to be far too optimistic, we took advantage of two techniques implemented in JKTEBOP to estimate realistic errors: a Monte Carlo test (MC) and a bootstrapping method based on the cyclic permutations of the residuals (RP or "prayer bead" algorithm, Southworth 2008). The errors from the RP algorithm are significantly larger, suggesting a non-negligible amount of red noise in our light curves. We therefore adopted conservatively the RP 1-σ errors in our analysis. The best-fit T_0 for each transit, converted from UT to barycentric Julian date (BJD), are shown in Table 5 along with their estimated uncertainties.

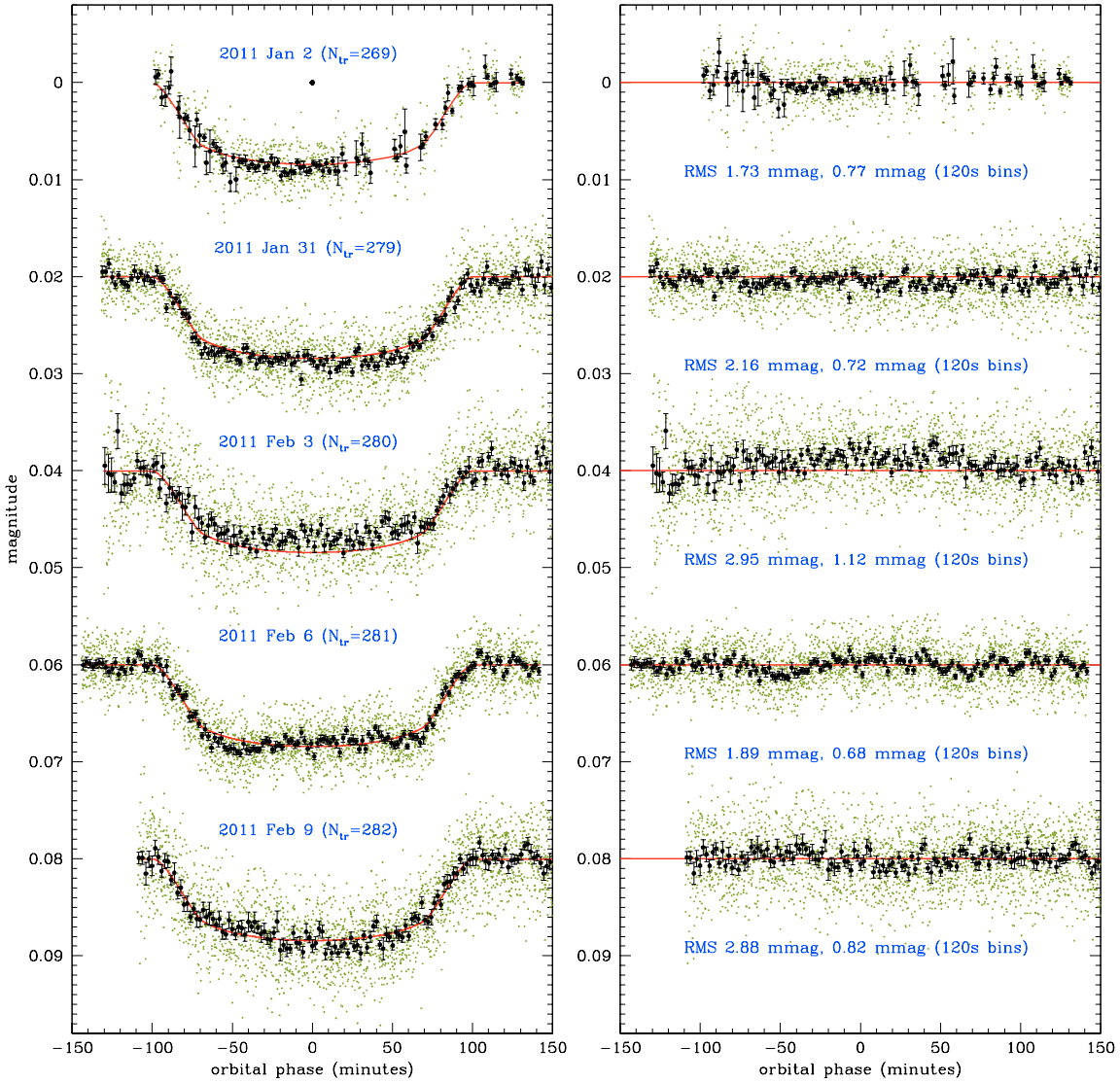

Figure 13: (*Left*): Light curves of HAT-P-13b taken at the Asiago 1.82m telescope, for the five transit summarized in Table 5. The unbinned photometric points are plotted in green, the 120-s binned points are plotted in black. The red line is the best-fit model fitted by JKTEBOP. Transits have been offset by intervals of 0.02 mag for clarity. (*Right*): photometric residuals around the best-fit model.

Our five timings points are very close in time to each other, four of them being consecutive transits ($N_{tr} = 258, 259, 260, 261$). They are consistent within the RP errors with a constant ephemeris ($O - C$ = +88, +0, −89, −79, +55 s) that has a standard deviation of 78 s (= 0.00090 d). This is also an external approximate upper limit for our timing precision, and agrees well with the uncertainties ΔT_0 that we estimated.

In the top left panel of Fig. 14, we plotted our five new data points, along with the ones available from the literature (Bakos et al. 2009; Szabó et al. 2010; Pál et al. 2011) in a $O - C$ diagram using as a reference the ephemeris given by Pál et al. (2011). We confirm the timings of Pál et al. (2011), with additional, more precise measurements. Our transits collected in January/February 2011 lie, respectively, 8.1σ, 13σ, 5.5σ, 22σ, and 8.9σ from the linear ephemeris fitted to the previous data. It is clear that an updated linear ephemeris cannot be fitted to all the available points with an acceptable χ^2. No significant trend in the $O - C$ diagram is visible for the 2011 transits (Fig. 14, top right panel).

The two transits shown as red squares in the plots were observed under non-optimal weather conditions. During the first transit, "sky was photometric during the transit, but it was foggy in the evening and from 40 min after the egress phase". During the second, "cirri were present that significantly affected the V band data, but the R light curve was well reconstructed" (from Szabó et al. 2010). Following a suggestion by an anonymous referee, we checked whether a linear ephemeris can be properly fitted by ignoring these two data points (Fig. 14, bottom left panel). All of the first four transits by Bakos et al. (2009) lie at $O - C < 0$ (two by more than 1σ), while the second three transits lie at $O - C > 0$ (all by more than 1σ), suggesting a systematic trend. In any case, it seems unlikely that both the Szabó et al. (2010) data points are outliers, as they deviate in the same direction by a consistent amount (12.4 min = 8.6σ, and 9.1 min = 3.2σ respectively). They also come from observations carried out 108 days apart, made with two different telescopes by professional astronomers. As a cross-check, we also tried to compare the timings presented by Bakos et al. (2009), Szabó et al. (2010), and Pál et al. (2011) and by ourselves with data collected by amateurs available from the Exoplanet Transit Database (ETD). None of those twenty-two light curves are reliable for our analysis, being plagued to various extents by systematic errors: more than half of these data points deviate by more than 1-σ from a linear ephemeris. Though this TTV needs to be confirmed in a future season, present observational evidence points towards an indication of an anomaly in the periodicity of the transit.

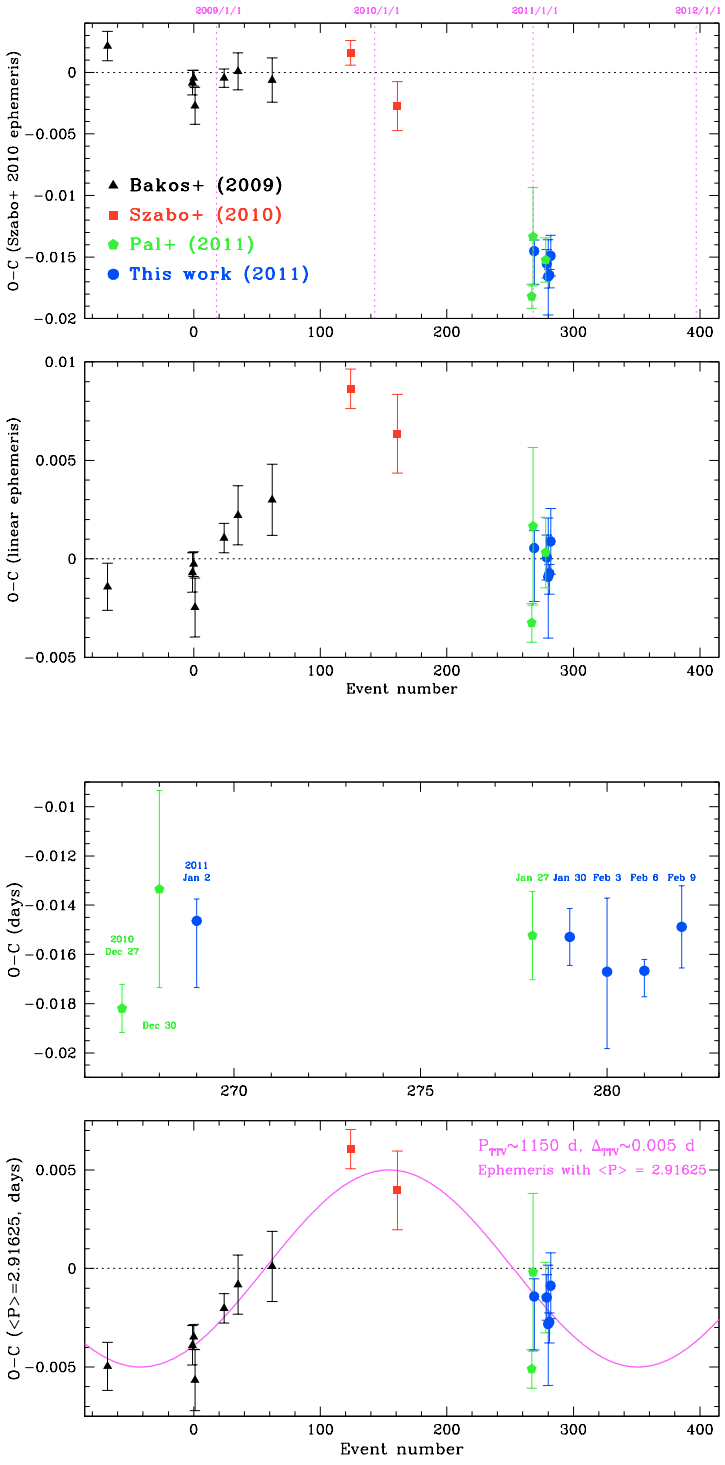

Figure 14: *Top left:* $O-C$ diagram following the Pál et al. (2011) linear ephemeris. The new points from TASTE (Table 4) are plotted in blue filled circles. *Bottom left:* $O-C$ diagram following a linear ephemeris, fitted ignoring the two data points (red squares) from Szabó et al. (2010). *Top right:* Same as top left, zoomed on the transits collected in Jan-Feb 2011. *Bottom right:* the $O-C$ diagram folded over an ephemeris with $\langle P \rangle = 2.91625$ days, perturbed by a sinusoidal TTV with a period of $P_{TTV} = 1150$ days and an amplitude $\Delta_{TTV} = 0.005$ days.

We consider for a moment that the claimed TTV is real. As this TTV appears as a sudden switch of the ephemeris, Pál et al. (2011) suggested that this deviation in the $O-C$ diagram could be interpreted as a "spike" caused by a long-period eccentric pertuber that is now near periastron. Examples of these systems can be found in the synthetic $O-C$ diagrams plotted by Holman & Murray (2005). This could explain why the 2008-2010 timing points are consistent with a linear ephemeris: such a perturber would have been far from HAT-P-13b, and its perturbative effects well within the measurement error. However, we note that the problem is still highly unconstrained, owing to the large errors and the uneven sampling of the previous measurements. Follow-up observations are required to constrain the mass and the orbit of the perturber without huge degeneracies in the parameter space. In particular, we propose 1) to search for any unpublished measurements performed in March–November 2010, when the rising part of the spike could have been sampled and 2) to schedule new observations in October 2011–April 2012 , to check whether the perturbation is still active, or the new timing points return to the original mean ephemeris.

To demonstrate that the measurements are consistent with different scenarios, we note that a periodic TTV cannot be excluded, in spite of the conclusions of Pál et al. (2011). We folded the $O-C$ diagram over an ephemeris that had an average period $\langle P \rangle = 2.91625$ days and had been perturbed by a sinusoidal TTV with an amplitude $\Delta_{TTV} = 0.005$ days and a period $P_{TTV} = 1150$ days (Fig. 14, last panel). This solution would be perfectly consistent with the available data, with only one outlier (the 2010 Dec 27 transit by Pál et al. 2011, 2.57σ from the best-fit solution), and compatible with the presence of an outer, coplanar, non-eccentric $5M_{\oplus}$ perturber locked in a 3:2 mean-motion resonance with HAT-P-13b, following the analytical approximations by Agol et al. (2005). This body could not have been detected by the RV measurements carried out so far. The observations that will be taken in October 2011–April 2012 will allow us to discriminate at least between this scenario and the "eccentric perturber" hypothesis, as a return to the original constant ephemeris would not be compatible with a periodic perturbation.

Acknowledgements

We thank A. Cunial and M. Fiaschi for the night support during the observations of HAT-P-13b. This work was partially supported by PRIN INAF 2008 "Environmental effects in the formation and evolution of extrasolar planetary system". V.N. acknowledges support by STScI grant DDRF D0001.82432.

4

A HOMOGENEOUS STUDY OF WASP-3B

In this chapter I will present the first TASTE work based on observations made at IAC facilities, namely a new study of the hot Jupiter WASP-3b from six high-precision light curves secured at the IAC-80 telescope. I will describe the thorough (re-)analysis carried out on both archival and our data, employing homogeneous techniques and software tools, with the goal of deriving auto-consistent planetary parameters and timing measurements. I will show that our ensemble data set is not in agreement with the periodic TTV previously claimed by Maciejewski et al. (2010). Instead, I will demonstrate that the measured TTV scatter is indeed statistically significant, though it does not show any significant periodicity. Hence I will discuss the possible causes for that behavior, and present an updated ephemeris and improved orbital/physical parameters for this target.

This chapter will be based on: V. Nascimbeni, A. Cunial, S. Murabito, P. V. Sada, A. Aparicio, G. Piotto, L. R. Bedin, A. P. Milone, A. Rosenberg, L. Borsato, M. Damasso, V. Granata, and L. Malavolta (2012) *TASTE III. A homogeneous study of transit time variations in WASP-3b*, A&A, submitted.

4.1 INTRODUCTION

Most of the extrasolar planets discovered so far are massive, gaseous giant planets. The present trend is to probe smaller and smaller masses, with the final aim of detecting temperate "super-Earths" or Earth-sized rocky planets (1-10 $M_\oplus$, 1-3 $R_\oplus$) around solar-type stars. The signal expected from a true Earth analog orbiting a Sun twin is extremely small: $\sim$ 80 ppm for the photometric transit, and $\sim$ 10 cm/s for the radial velocity (RV) Doppler shift. In the conventional framework both measurements are required to derive the planetary mass and radius (M_p, R_p), i.e. the basic quantities necessary to confirm the planetary status of the transiting body, and to characterize it. Achieving a photometric precision of $\sim$ 20 ppm (4σ) over the timescale of a transit is within reach of space-based telescopes only, while a long-term $\lesssim$ 20 cm/s RV accuracy is still too ambitious even for the most stable spectrographs, like HARPS. A few indirect techniques have been developed to get estimate of M_p (or upper limits to it) for a non-transiting planet without the need of RV measurements, the most promising being the Transit Timing Variation (TTV) method.

By monitoring a known transiting planet by high-precision photometry, the central instant T_0 of each individual transit can be estimated.

The gravitational perturbation of a previously-unknown third body, not necessarily transiting, can cause a significant variation of the orbital period P (Holman & Murray 2005). The effect is greatly increased if the perturber is locked in a low-order mean-motion resonance with the transiting planet (Agol et al. 2005). The TASTE project was started in 2010 to search for TTVs with several ground-based, medium-class facilities on a sample of carefully selected targets (Nascimbeni et al. 2011a).

The TTV technique has been proven to work by several results from the Kepler mission. Some candidate planets in multiple systems, for instance, were validated through TTV analysis (Lissauer et al. 2011). In the past few years, some authors have claimed TTV detections also from ground-based facilities, but none is confirmed so far. Among these claims, WASP-10b (Maciejewski et al. 2011), WASP-5b (Fukui et al. 2011), the intriguing case of HAT-P-13b, that was monitored also by TASTE (Pál et al. 2011; Nascimbeni et al. 2011c; Southworth et al. 2012), and the subject of the present investigation: WASP-3b (Maciejewski et al. 2010).

WASP-3b is a typical "hot Jupiter" (1.31 R_{jup}, 1.76 M_{jup}) hosted by a F7-8 dwarf discovered by Pollacco et al. (2008), with a considerably short period $P \simeq 1.8468$ days. Analyzing an $O-C$ (*Observed − Calculated*) diagram computed by comparing the T_0 of fourteen transits with the value predicted by a linear ephemeris, Maciejewski et al. (2010) claimed the detection of a sinusoidal modulation with a period of $P_{TTV} \simeq 127.4$ days and a semi-amplitude of ~ 0.0014 days $\simeq 2$ min. They proposed to interpret this signal as induced by an outer perturber, identifying three possible orbital solutions in the range 6-15 $M_\oplus$ and $P = 3.03$-3.78 days. No independent confirmation of this claim has been published so far, though both Littlefield (2011) and Sada et al. (2012) discussed the consistence of their data with that TTV modulation.

In this paper we present (Section 4.2) eleven unpublished transits of WASP-3b: six of them have been gathered at the IAC-80 telescope and five at the UDEM 0.36m (Universidad de Monterrey, Mexico). We also sifted the literature in search of all the archival photometric data useful for a TTV study (Section 4.3). In Sections 4.4 and 4.5 we describe how both new and archival light curves, for a total of forty-nine transits, were reduced and analyzed with the same software tools in a homogeneous way, to provide a consistent estimate of the planetary parameters and their uncertainties. This is crucial especially for T_0, whose estimate has been shown to be easily biased by the employed analysis technique (Fulton et al. 2011; Southworth et al. 2012). Besides T_0, we also refined the orbital and physical parameters of WASP-3b, and computed an updated ephemeris (Eq. 18) for any forthcoming study on this target. In Section 4.5.2 we demonstrate that the TTV claimed by Maciejewski et al. (2010) is not supported by our analy-

sis, and probably due to small-sample statistics. Yet, we point out that the revised O − C diagram displays a complex, non-periodic structure and is not compatible with a constant orbital period. Finally, in Section 4.6 we discuss the possible origin of this TTV signal, and show that careful dynamical modeling and additional photometric and RV follow-up is required to confirm the hypothesis and to constrain the mass and period of the possible perturber(s).

4.2 TASTE OBSERVATIONS

4.2.1 *IAC-80 observations*

We observed six transits of WASP-3b between 2011 May 7 and Aug 2, employing the CAMELOT camera mounted on the IAC80 telescope. A log summarizing dates and other quantities of interest is reported in Table 6. Individual transits are identified by an ID code ranging from `N1` to `N6`. IAC80 is a 0.8m Cassegrain reflector installed at the Teide Observatory (Tenerife, Canary Islands) and operated by Instituto de Astrofísica de Canarias (IAC). CAMELOT is a conventional imager with a $10'.4 \times 10'.4$ field of view (FOV), equipped with a E2V 42-40 2048×2048 CCD detector, corresponding to a $0.304''$ pixel scale. The software clock interrogated to save the timestamps in the image headers is automatically synchronized with the GPS time signal.

All the observations were carried out with a standard Bessel `R` filter and the same instrumental setup. Windowing and 2×2 binning were employed to increase the duty-cycle of the photometric series, as described in Nascimbeni et al. (2011a). A $10.4' \times 3.2'$ read-out window was chosen to image the target and a previously selected set of reference stars in a region of the detector free from cosmetic defects. The one-amplifier readout was preferred to prevent gain offsets between different channels. Stars were intentionally defocused to a FWHM of 10-13 binned pixels ($\simeq$ 6.0-8.0″) to avoid saturation and to minimize systematic errors due to intra-pixel and pixel-to-pixel inhomogeneities (Southworth et al. 2009a). Exposure time was set to 20 s (`N1-4`) or 15 s (`N5-6`), resulting in a net cadence τ = 19-25 s and a $\sim$ 75-87% duty-cycle, with the only exception of `N3`. On that night, due to software problems, the images were read unbinned and in unwindowed readout mode, decreasing both signal-to-noise ratio (S/N) and duty-cycle.

The weather was photometric on all nights, except for a few thin veils during `N3`. Our initial goal was to start the series one hour before the first contact of the transit, and to stop one hour after the last contact. Nevertheless, the amount of pre-transit photometry is only a few minutes for the `N4` and `N6` light curves, and the `N1` series was interrupted twenty minutes earlier because of twilight.

Table 6: Summary of the light curves of WASP-3b analyzed in this work.

N	ID	evening date	telescope	band	N_p	τ (s)	σ (mmag)	σ_{120} (mmag)	reference paper	notes
250	G1	2008/05/18	LT-2.0m	$(R+V)$	4799	3.0	3.97	0.63	Gibson et al. (2008)	—
309	G2	2008/09/04	LT-2.0m	$(R+V)$	3900	3.0	3.81	0.61	Gibson et al. (2008)	partial
248	T1	2008/05/15	FLWO-1.2m	Sloan i	403	33.8	1.38	0.73	Tripathi et al. (2010)	partial
262	T2	2008/06/10	FLWO-1.2m	Sloan i	269	33.6	1.16	0.61	Tripathi et al. (2010)	partial
268	T3	2008/06/21	FLWO-1.2m	Sloan i	522	34.2	1.59	0.85	Tripathi et al. (2010)	—
280	T4	2008/07/13	UH-2.2m	Sloan z	276	67.5	0.81	0.61	Tripathi et al. (2010)	—
444	T5	2009/05/12	FLWO-1.2m	Sloan g	224	78.3	1.17	0.95	Tripathi et al. (2010)	—
451	T6	2009/05/25	FLWO-1.2m	Sloan g	238	74.5	1.08	0.85	Tripathi et al. (2010)	—
486	M1	2009/07/28	Rohzen-0.6m	R	283	49.3	2.06	1.32	Maciejewski et al. (2010)	—
499	M2	2009/08/21	Rohzen-0.6m	R	200	72.2	2.36	1.83	Maciejewski et al. (2010)	—
506	M3	2009/09/03	Rohzen-0.6m	R	297	45.8	2.87	1.78	Maciejewski et al. (2010)	—
519	M4	2009/09/27	Jena-0.9m	R	259	59.6	2.72	1.92	Maciejewski et al. (2010)	—
539	M5	2009/11/03	Jena-0.9m	R	258	51.6	2.41	1.58	Maciejewski et al. (2010)	—
629	M6	2010/04/18	Jena-0.9m	R	206	78.0	1.50	1.21	Maciejewski et al. (2010)	—
486	D1	2009/07/28	OAVdA-0.25m	R	353	46.7	2.30	1.43	Damasso et al. (2010)	—
290	C1	2008/07/31	HRI@EPOXI	clear	1157	53.2	0.89	0.59	Christiansen et al. (2011)	—
291	C2	2008/08/02	HRI@EPOXI	clear	958	51.7	1.01	0.66	Christiansen et al. (2011)	—
292	C3	2008/08/04	HRI@EPOXI	clear	985	51.3	1.03	0.67	Christiansen et al. (2011)	—
293	C4	2008/08/06	HRI@EPOXI	clear	1138	51.3	0.98	0.64	Christiansen et al. (2011)	—
294	C5	2008/08/08	HRI@EPOXI	clear	281	52.2	0.97	0.64	Christiansen et al. (2011)	partial
296	C6	2008/08/12	HRI@EPOXI	clear	954	54.6	0.93	0.63	Christiansen et al. (2011)	partial
297	C7	2008/08/13	HRI@EPOXI	clear	640	51.5	1.02	0.67	Christiansen et al. (2011)	—
298	C8	2008/08/15	HRI@EPOXI	clear	852	51.5	1.07	0.70	Christiansen et al. (2011)	—
654	L1	2010/06/04	SC-11″	clear	218	76.8	2.68	2.14	Littlefield (2011)	—
686	L2	2010/08/02	SC-11″	clear	192	113.	2.38	2.31	Littlefield (2011)	—
706	L3	2010/09/08	SC-11″	clear	192	65.5	2.70	1.99	Littlefield (2011)	—
488	Z1	2009/08/01	Weihai-1m	V	323	43.4	7.35	4.42	Zhang et al. (2011)	—
444	S1	2009/05/12	VCT-0.5m	Sloan z	177	94.7	2.25	1.99	Sada et al. (2012)	—
653	S2	2010/06/02	KPNO-2.0m	J	250	71.8	1.50	1.16	Sada et al. (2012)	—
653	S3	2010/06/02	VCT-0.5m	Sloan z	186	91.1	2.23	1.94	Sada et al. (2012)	—
842	S4	2011/05/17	VCT-0.5m	Sloan z	217	87.4	3.52	3.00	Sada et al. (2012)	—
194	E1	2009/04/22	Newton-0.2m	clear	194	74.2	3.36	2.64	ETD obs. Trnka	—
446	E2	2009/05/16	SC-12″	I	181	104.	3.18	2.96	ETD obs. Gregorio	—
653	E3	2010/06/02	SC-12″	R	177	72.7	2.90	2.26	ETD obs. Shadik & Patrick	—
666	E4	2010/06/26	Newton-0.3m	B	266	61.6	3.69	2.64	ETD obs. Garlitz	—
699	E5	2010/08/26	RC-12.5″	R	119	124.	2.62	2.67	ETD obs. Hose	—
838	E6	2011/05/09	Monteboo-0.6m	R	393	35.3	2.55	1.38	ETD obs. Janov	—
849	E7	2011/05/30	RC-12″	V	297	51.2	5.65	3.69	ETD obs. Dvorak	—
837	U1	2008/09/03	UDEM-0.36m	I	467	33.7	4.27	2.26	this work	—
844	U2	2009/06/05	UDEM-0.36m	I	566	34.1	3.78	2.01	this work	—
864	U3	2009/07/25	UDEM-0.36m	Sloan z	383	45.1	4.38	2.68	this work	—
877	U4	2009/08/05	UDEM-0.36m	Sloan z	371	44.2	5.03	3.05	this work	low S/N
884	U5	2010/08/15	UDEM-0.36m	I	471	35.0	3.31	1.79	this work	—
837	N1	2011/05/07	IAC-0.8m	R	678	24.0	1.78	0.79	this work	—
844	N2	2011/05/21	IAC-0.8m	R	742	23.1	1.53	0.67	this work	—
851	N3	2011/06/02	IAC-0.8m	R	412	38.1	2.93	1.65	this work	low S/N
864	N4	2011/06/26	IAC-0.8m	R	566	25.1	1.53	0.70	this work	—
877	N5	2011/07/20	IAC-0.8m	R	785	20.1	2.12	0.87	this work	—
884	N6	2011/08/02	IAC-0.8m	R	694	19.9	2.34	0.95	this work	red noise

The columns give: the transit epoch N assuming $T = T_0 + NP$ and the original ephemeris (Eq. 11) from Pollacco et al. (2008), the ID code, the "evening date" of the observation, the filter employed, the number of unbinned data points, the average net cadence τ in seconds, the photometric scatter σ measured as the 68.27^{th} percentile of the residuals from the best-fit model, the normalized photometric scatter $\sigma_{120} = \sigma\sqrt{\tau/120^s}$, the reference paper or database, and comments.

4.2.2 *UDEM observations*

We observed five transits of WASP-3b between 2008 Sep 3 and 2010 Aug 15 with the Universidad de Monterrey (UDEM) 0.36-m reflector. UDEM is a small private college observatory having Minor Planet Center Code 720 located in the suburbs of Monterrey, México. The data were acquired using standard Bessel I- and Sloan z-band filters with a 1280×1024 pixel CCD camera at 1.0″ pixel scale, resulting in a field-of-view of $\sim 21'.3 \times 17'.1$. The observations were slightly defocused to improve the photometric precision and to avoid saturation. On-axis guiding was used to maintain pointing stability. Exposure times were set to 30 s for I and 40 s for z. All images were binned 2×2 to facilitate rapid readout ($\sim$ 3 s). Each observing session lasted about 4.5 hours in order to accommodate the transit event and also to cover about one hour before ingress and one hour after egress. The computer clock was reset to UTC via Internet at the beginning of every observing session to the nearest second.

4.3 ARCHIVAL LIGHT CURVES

All the available archival data were searched for any light curve useful for a TTV analysis, i.e. complete transits of WASP-3b with a suitable S/N. Partial transits were rejected, except for a few cases with high S/N and low content of "red noise" (Pont et al. 2006). Hereafter we refer to each light curve with the corresponding alphanumeric ID code reported in Table 6. Overall, thirty-eight archival light curves were (re-)analyzed in the present study:

- Gibson et al. (2008): two transits in 2008 (`G1-2`) observed with the RISE camera mounted at the 2.0 m Liverpool Telescope. Both nights were photometric. The second series (`G2`) ended just before the last contact. The RISE camera filter has a custom wideband 500-700nm, approximately covering both the Johnson R and V passbands.

- Tripathi et al. (2010): five transits in 2008/2009 (`T1-5`) from two different telescopes (Fred Lawrence Whipple Observatory FLWO-1.2m and University of Hawaii UH-2.2m) and in three Sloan passbands (g, i, z), gathered to complement their high-precision RV measurements. The first two FLWO i transits (`T1-2`) are partial, the first one missing the first contact by only few minutes.

- Damasso et al. (2010): one complete transit observed in 2009 (`D1`), with a commercial 0.25 m reflector in a nonstandard R band, as part of the pilot study for the APACHE project.

- Maciejewski et al. (2010): six complete transits in the R band from two different telescopes (`M1-3` at Rohzen-0.6m, `M4-6` at

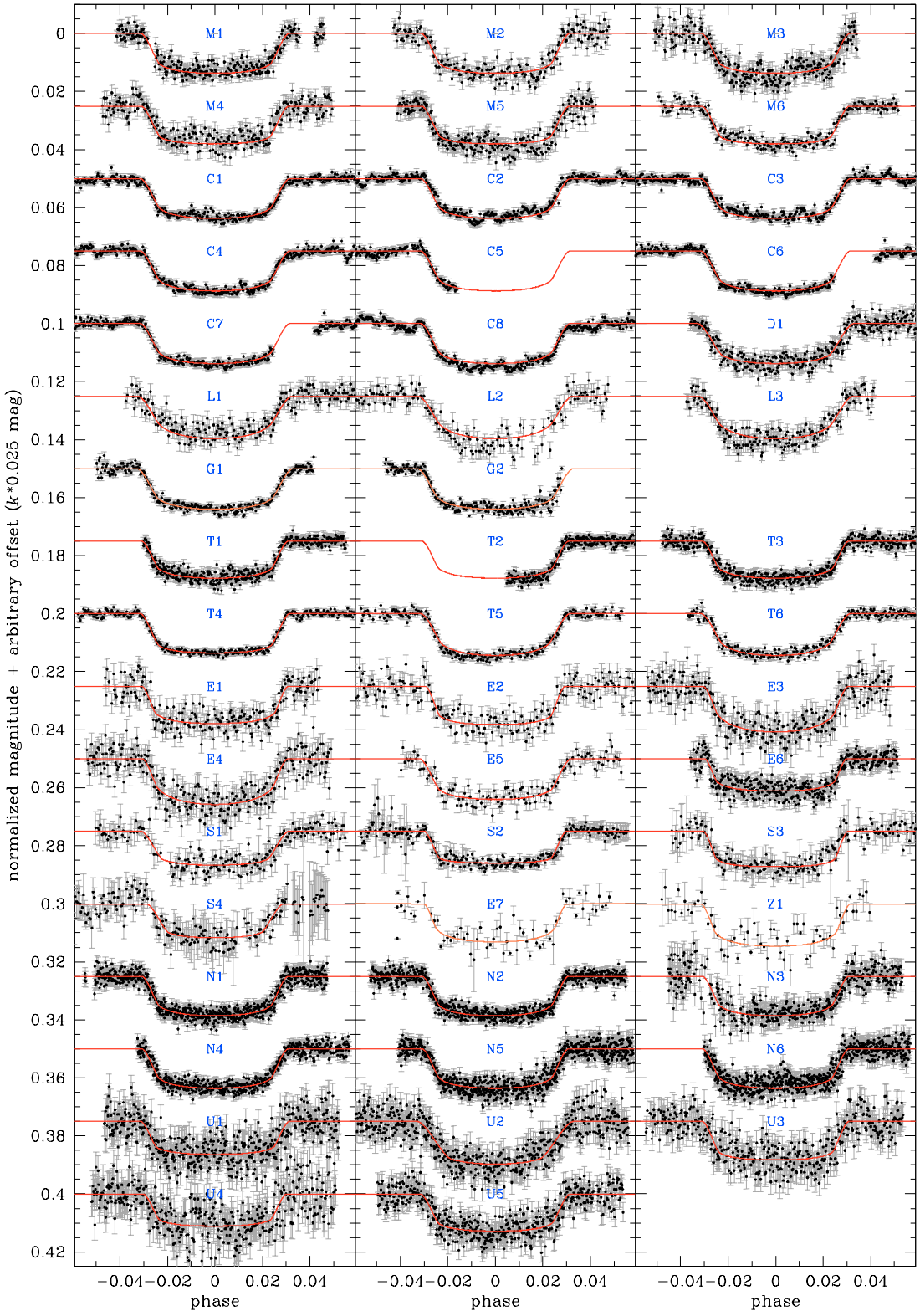

Figure 15: Light curves of WASP-3b analyzed in this Paper. The `ID` code of each transit matches the corresponding entry in Table 6. Data points are plotted with the original cadence, except for `G1`, `G2` and `Z1`, `E7` that are binned respectively on 30 s and 300 s intervals for clarity. The red line is the best-fit model found by JKTEBOP. Transits have been offset in magnitude by integer multiples of 0.025.

Jena-0.9m). The first five observations (M1-5) were carried out on focused images, a practice resulting in a possible increase of the content of red noise.

- Christiansen et al. (2011): six complete (C1-4, C7-8) and two partial (C5-6) transits, extracted from a 18-day photometric series secured by the High Resolution Imager (HRI) mounted on the spacecraft EPOXI, as part of the EPOCh project. No filter was employed.

- Littlefield (2011): three transits observed with a 11″ Schmidt-Cassegrain reflector and without filter (L1-3). These three light curves correspond to the first, third, and fifth one presented in the original paper. The S/N of the other curves is too low for the inclusion in the present study.

- Zhang et al. (2011): one 2009 transit in the V band from the Weihai-1.0m telescope (Z1).

- Sada et al. (2012): four transits secured in 2009-2011 by different telescopes: S1 and S3-4 at the 0.5m Visitor Center telescope at Kitt Peak National Observatory (KPNO), in the Sloan z band; S2 at the KPNO 2.1m reflector in the J band, exploiting the FLAMINGO infrared imager.

Other six light curves from various amateur observers (E1-7) were visually selected and downloaded from the ETD database[1].

The first two follow-up light curves of WASP-3b were published by Pollacco et al. (2008): one transit observed at the IAC80 (alternating V and I filters) and one at the Keele-0.6m (R band), both in 2007. Unfortunately, the original light curves are no more retrievable and we did not include them in this study. A T_0 data point is determined by the first term of their published ephemeris:

$$T_0(BJD_{UTC}) = 2454143.8503^{+0.0004}_{-0.0003} + N \cdot 1.846834^{+0.000002}_{-0.000002} \quad (11)$$

One should be careful, however, as this T_0 (corresponding to 2007 Feb 12) is not an independent measurement of a single transit event. Instead, it comes from an ensemble analysis of SuperWASP, IAC80 and Keele-0.6m data. For this reason we adopted T_0 from Eq. (11) as our first data point in the determination of our new ephemeris, but not in our subsequent TTV analysis (Section 4.5.2).

The epoch N of each reported observation in our set is defined according to the ephemeris in Eq. (11), i.e. as the number of transits elapsed from 2007 Feb 12. Each light curve was calibrated in time by identifying the time standard reported in the data headers (occasionally, contacting the authors) and converting the timestamps to

1 http://var2.astro.cz/ETD (Poddaný et al. 2010)

BJD(TDB), i e. based on Barycentric Dynamical Time following the prescription by Eastman et al. (2010). It is worth noting that most of these observations were not performed with the specific goal of a TTV analysis. Even when the authors report a reliable synchronization source (GPS, NTP, etc.) for their data, it is impossible to carry out an external confirmation of that. The only exception, discussed in Section 4.6, is when two or more independent observations of the same event were performed.

When required, light curves in flux units were converted to magnitudes and normalized to zero by fitting a low-order polynomial function to the off-transit data points. In a few cases, the tabulated photometric errors are severely underestimated, as confirmed by the reduced $\chi^2_r \gg 1$ (χ^2 being defined as the χ^2 divided by the number of degrees of freedom of the fit). We dealt with this by rescaling the errors by a factor of $\sqrt{\chi^2_r}$. When the photometric errors were not published, the error was assumed to be constant and equal to the scatter σ of the off-transit polynomial-corrected curve. We define the scatter as the 68.27^{th} percentile of the residual distribution from the median, after a 5σ iterative clipping. This measurement is much more robust against outliers than the classical RMS.

4.4 DATA REDUCTION

4.4.1 *IAC80 photometry*

The six IAC80 light curves (`N1-6`) were reduced with the STARSKY photometric pipeline, presented in Nascimbeni et al. (2011a,c) but here upgraded with some improvements. The present version v1.1.002 adopts a new, fully empirical weighting scheme to carry out differential photometry. Reference stars were previously weighted by the amount of scatter measured on their light curves after being registered to the total reference magnitude m_i (that is, the weighted mean of the instrumental magnitudes of all the comparison stars; Broeg et al. 2005). That was an iterative process. Instead, the updated version first extracts the off-transit part of the series, then constructs a set of "intermediate" light curves of the reference stars by subtracting the magnitude of each of them to the off-transit magnitude of the target. Ideally, that curves should be flat and their RMS should be equal to the quadratic sum $\sqrt{\tilde{\sigma}^2 + \sigma_t^2}$, being σ_t the theoretical photometric noise expected on the target (calculated as in Nascimbeni et al. 2011a) and $\tilde{\sigma}$ the intrinsic noise of the reference star, defined as at the end of Section 4.3. We therefore estimated the latter as $\tilde{\sigma} = \sqrt{\sigma^2 - \sigma_t^2}$. The individual weights for a given comparison star are then assumed to be $1/\sqrt{\tilde{\sigma}^2}$. The output of this weighting algorithm is checked during every run against two other weighting schemes: 1) equal weights, i.e. unweighted, and 2) using weights derived from the expected the-

oretical noise computed for the reference stars. The DSYS and PSYS parameters (as defined in Nascimbeni et al. 2011c) allow to diagnose "bad" reference stars, and to set their weights to zero. For all the N1-N6 transits, the same set of eleven reference stars was employed for consistence. All of them show no sign of variability or higher-than-expected scatter.

A second improvement to STARSKY is a new algorithm developed to deal with light curves having red noise caused by veils, trails or thin clouds. This happen when the cloud possess a structure at angular scales on the same order of the FOV, and/or it is moving fast. Even differential photometry can be affected by these events, as the change of transparency can affect the target and the reference stars by a different amount. Of course, this systematic effect is correlated on how fast the transparency is changing, and this correlation can be exploited to discard the affected frames. A quantity that we called "numerical derivative of the absolute flux" (NDAF) is evaluated for each frame i of the series:

$$\mathtt{NDAF} = \frac{1}{F_i} \frac{F_{(i+1)} - F_{(i-1)}}{t_{(i+1)} - t_{(i-1)}} \tag{12}$$

being F_i the weighted instrumental flux of the reference stars ($F_i = 10^{-0.4 m_i}$, m_i defined as above), and t_i the JD time at the mid-exposure. When NDAF deviates more than 4σ from its average along the series, the frame is discarded. The first and last frame are ignored by our algorithm.

STARSKY outputs light curves extracted from a set of different photometric apertures. These curves are then detrended by a routine which searches for linear and polynomial correlations between the off-transit flux and several combinations of external parameters such as: the position of the star on the detector, the airmass, the FWHM of the stellar profiles, the mean sky level, the reference flux F_i, and time. Eventually, we chose the light curve with the smallest amount of scatter σ and the lowest level of red noise estimated from the β parameter as defined by Winn et al. (2008). The overall S/N of an observation can be quantified by rescaling the unbinned photometric σ of the light curve (having a net cadence τ) on a standard 120-s timescale, that is by calculating $\sigma_{120} = \sigma\sqrt{\tau/120^s}$. With the only exception of N3, the final IAC80 light curves have $\sigma_{120} = 0.67$-0.95 mmag (Table 6, Fig. 17), only slightly larger than that achieved by Gibson et al. (2008), Tripathi et al. (2010) and Christiansen et al. (2011), with space-based or much larger facilities. N6 shows a large amount of red noise of unknown origin, but probably related to a color-dependent systematic caused by variable atmospheric extinction. For the above-mentioned reasons, N3 and N6 were employed in the determination of our new ephemeris, but not in our TTV analysis (Section 4.5).

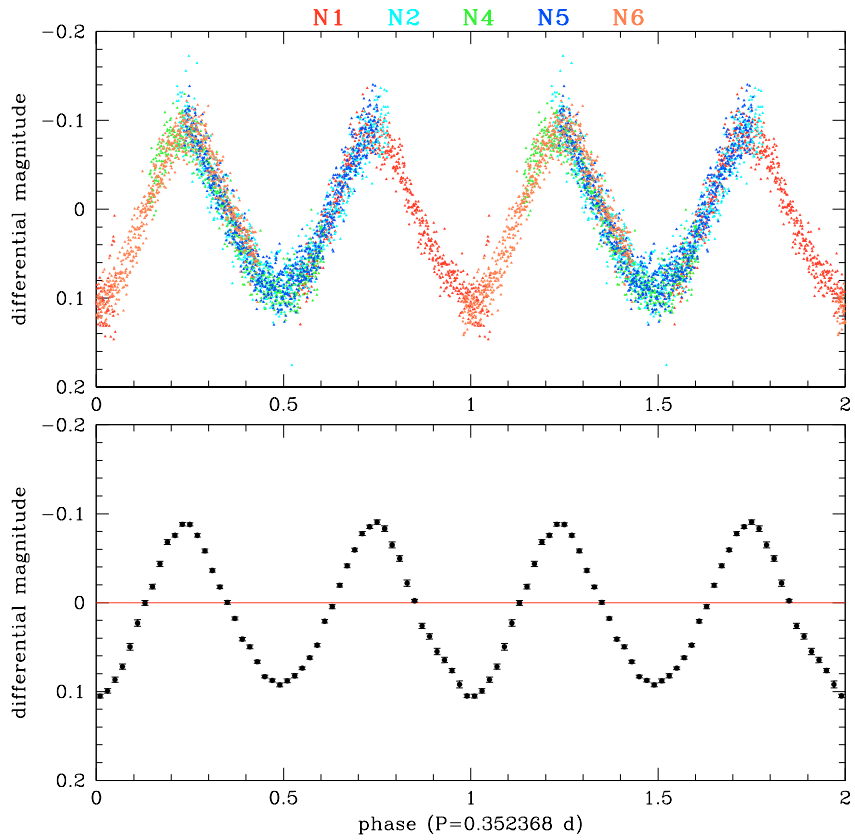

Figure 16: Light curve of a previously unreported R ∼ 15 variable star in the WASP-3 field, classified as a contact eclipsing binary (see text for details). *Top panel:* unbinned data points folded on the best-fit period P = 0.353626 days. Different nights are coded in different colors. *Bottom panel:* same as above, binned on 0.02 intervals in phase.

4.4.2 *A new eclipsing variable*

A star in the WASP-3 field (UCAC3 coordinates: $\alpha = 18^h\,34^m\,07^s.36$, $\delta = +35°\,38'\,59''.6$, epoch 2000.0; Zacharias et al. 2010), initially chosen as reference star, was found to be variable and excluded from the reference list. A complete light curve of this variable was assembled by registering the magnitudes on the `N1-2` and `N4-N6` frames on a common zero point (Fig. 16, upper panel). When folded on the $P \simeq 0.3524$ days peak detected in the Lomb & Scargle periodogram, the binned curve shows a periodical pattern with equal maxima and slightly different minima, typical of contact eclipsing binaries (W UMa-type; Fig. 16, lower panel). We derived the following ephemeris, setting $\Phi = 0$ at the phase of primary minimum and estimating uncertainties through a bootstrapping algorithm:

$$\begin{aligned} T_0(BJD_{TDB}) &= 2\,455\,776.48932 \pm 0.00024 + \\ &\quad + \Phi \cdot 0.3523683 \pm 0.0000018 \end{aligned} \tag{13}$$

This variable star appears to be unpublished, and we submitted it to the International Variable Star Index (VSX J183407.3+353859 identifier). Colors from catalog magnitudes: $V = 15.63$, $R = 14.99$ (NOMAD; Zacharias et al. 2004), $J = 14.64$, $H = 14.34$, $K_s = 14.21$ (2MASS; Skrutskie et al. 2006), and proper motions $\mu_\alpha \cos\delta = -32$ mas/yr, $\mu_\delta = 19$ mas/yr (UCAC3) suggest that this object could be a binary with both components of late-G spectral type.

4.4.3 *UDEM photometry*

Standard dark current subtraction and twilight sky flat-field division process were performed for calibration on each image of the UDEM light curves (`U1-5`). Aperture differential photometry was carried out on the target star and 4-6 comparison stars of similar magnitude ($|\Delta m| \lesssim 1.5$). The apertures used varied for each date due to defocus and weather conditions, but they were optimized to minimize the scatter of the resulting light curves. We found that the best results were obtained by averaging the ratios of WASP-3b to each comparison star. This produced smaller scatter than the method of ratioing the target star to the sum of all the comparison stars. We estimated the formal error for each photometric point as the standard deviation of the ratio to the individual comparison stars, divided by the square root of their number (error of the mean).

After normalizing the target star to the comparison stars and averaging, some long-term systematics as a function of time were found. This is perhaps caused by differential extinction between the transit and comparison stars, which generally have different and unknown

spectral types. This variation was removed by fitting a linear airmass-dependent function to the out-of-transit baseline of the light curve.

4.5 DATA ANALYSIS

4.5.1 *Fitting of the transit model*

We chose to analyze all the new and archival light curves employing the same software tools and algorithms. Our goal was to get homogeneous estimate of the physical/orbital parameters of WASP-3b. In particular we were interested for our TTV analysis in estimating the T_0 of each transit and its associated error in the most accurate way, avoiding biases due to different techniques.

JKTEBOP[2] code version 25 (Southworth et al. 2004) was run to fit a model light curve over our data and to derive the four main photometric parameters of the transit: the orbital inclination i, the ratio of the fractional radii $k_r = R_p/R_\star$, the sum of the fractional radii $\Sigma_r = R_p/a + R_\star/a$ ($R_\star$ is the stellar radius, a the orbital semi-major axis), and the mid-transit time T_0. We set a quadratic law to model the limb darkening (LD) effect, being u_1 the linear term and u_2 the quadratic term.

Southworth (2010a) among others has shown that fixing the values of both u_1 and u_2 should be avoided, as it could lead to an underestimate of the errors. On the other hand, most light curves have a S/N too low to let both u_1 and u_2 free, and the resulting best-fit results can be unphysical. We set the quadratic term u_2 always fixed to its theoretical value interpolated from the tables computed by Claret (2000) (BVR_cI_c bands), and Claret (2004) (Sloan $ugriz$), adopting the stellar parameters of WASP-3 derived by Pollacco et al. (2008). For all the light curves from nonstandard photometry, that is unfiltered CCD photometry (`C1-8`, `L1-3`, `E1`) or from wide-band $R + V$ photometry (`G1-2`), estimating first-guess LD coefficients is not trivial. As for `G1-2`, we interpolated $u_1 = 0.24$ and $u_2 = 0.38$ from the tables by Claret (2000) by taking the average of the values tabulated for the Johnson-V and Cousin-R bands, as done by Gibson et al. (2008). We did the same for `C1-8`, `L1-3`, and `E1`, assuming that the quantum efficiency of a typical unfiltered CCD usually peaks somewhere in between those two bands.

Then one of the three following procedures was applied:

1. On the data sets with a high overall S/N and with two or more transits gathered with the same instrument and filter (`G1-2`; `T1-3`; `T5-T6`; `M1-3`; `M4-5`; `C1-8`; `L1-3`; `N1-5`) we first fitted a model with free i, k_r, Σ_r, T_0 (and u_1 fixed at its theoretical value) to the "best" individual light curves to get a preliminary estimate of

2 http://www.astro.keele.ac.uk/~jkt/codes/jktebop.html

their T_0. For "best" we mean complete transits with high S/N: our choice is summarized in Table 7, fourth column. Then we phased all those curves setting $T_0 = 0$. The free parameters i, k_r, Σ_r, u_1 were fitted again on the stacked light curve, in order to get a high-S/N "reference" model of the transit by integrating the information contained in the whole set. We fixed i, k_r, Σ_r, u_1 to their best-fit values, and fitted a model with only T_0 as free parameter on all the individual transits, including the low-S/N or partial ones.

2. On `T4`, a high-S/N but single light curve, we carried out one simultaneous fit with i, k_r, Σ_r, T_0, and u_1 as free parameters.

3. In all the other cases, the data quality did not allowed us to constrain u_1 to values with physical meaning, thus u_1 was fixed to its theoretical value along with u_2. Each transit was then fitted individually to get i, k_r, Σ_r, and T_0.

The construction of the reference model from the IAC80 best data set (`N1-2`, `N4-5` light curves) is summarized in Fig. 17, as one example. It is worth noting that on average the individual light curves have $\sigma_{120} = 0.75$ mmag, which decreases to $\sigma_{120} = 0.39$ mmag on the stacked data points. The expected noise from Poissonian statistics is $0.75/\sqrt{4} = 0.375$ mmag. By taking also into account that our observations do not cover always the same orbital phases, we are confident that the level of red noise in our photometry is very low.

As the formal errors derived by least squares techniques are known to be underestimated in presence of correlated noise, we took advantage of two techniques implemented in JKTEBOP to estimate realistic errors: a Monte Carlo test (MC) and a bootstrapping method based on the cyclic permutations of the residuals (RP or "prayer bead" algorithm, Southworth 2008). The errors on all parameters obtained with the RP algorithm are on average significantly larger, suggesting a non-negligible amount of red noise in most of the light curves. We thus adopted conservatively the RP results in our subsequent analysis. Mean values and error bars can be estimated in two different ways: 1) as the arithmetic mean of the RP distribution associated to its standard error $\pm\sigma$, and 2) as the median of the RP distribution along with its 15.87^{th} (σ_-) and 84.13^{th} percentile (σ_+). The first estimate assumes a gaussian distribution, while the latter is purely empirical: they should match in absence of red noise.

We adopted as final results the RP median and uncertainties σ_+, σ_- for every fitted parameter except T_0. The estimated T_0 will be analyzed in Section 4.5.2 with periodogram techniques that cannot deal with asymmetric error bars, thus for this parameter we adopted the RP means with gaussian errors $\pm\sigma$. The best-fit values of Σ_r, k_r, i and u_1 modeled on each individual data set are summarized in Table 7. We show also the theoretical value of the linear LD coefficient $u_{1,\text{th}}$

as interpolated from Claret (2000, 2004). On all subsets, u_1 and $u_{1,th}$ are in agreement within $\sim 1\sigma$. This holds even for C1-8, L1-3, and G1, demonstrating that assumptions previously made on nonstandard "clear" or $R+V$ photometry are reasonable.

The transit parameters Σ_r, k_r, and i are purely geometrical and should not depend on wavelength or observing technique. It is then possible to integrate all the information extracted from individual data sets (Table 7) to obtain final quantities of higher precision. We computed the weighted means of all the subset estimate of Σ_r, k_r, and i listed in Table 7, obtaining the result shown in the last but one line of the same table ($\langle$weighted mean$\rangle_1$). As pointed out from previous works (e.g., Southworth 2008), these three quantities are correlated with each other, as it is evident by plotting their individual estimate on planes projected from the three-dimensional parameter space (Σ_r, k_r, i) (Fig. 18). The data point extracted from subset T1,T3 appears as a probable outlier in two correlation plots among three. We re-evaluated the weighted mean after removing that point ($\langle$weighted mean$\rangle_2$ in Table 7). The resulting averages are quite similar to those evaluated without removing the outlier, but the uncertainty on k_r is smaller. We adopt the second mean as final estimate:

$$\Sigma_r = 0.2187 \pm 0.0098 \quad (14)$$

$$k_r = 0.1058 \pm 0.0012 \quad (15)$$

$$i = 84^\circ.12 \pm 0.82 \quad (16)$$

More in general, results obtained from subsets T1-3 (Sloan i) and T5-6 (Sloan g) are slightly but significantly in disagreement with each other, a fact already noted by Tripathi et al. (2010) and then attributed to the presence of residual red noise.

4.5.2 *TTV analysis*

The best-fit T_0 values for each transit, after being uniformly converted to BJD(TDB), are shown in Table 8 along with their estimated $\pm 1\sigma$ uncertainties (second column). For completeness we also tabulated the median value of T_0 estimated from the distribution of the RP residuals (third column of Table 8) along with its 15.87^{th} (σ_-) and 84.13^{th} percentile (σ_+).

We mentioned above that the distribution of the RP residuals around the best-fit value should be symmetric if the noise budget is dominated by independent and random errors, i.e. "white noise". Hence a "skewed" distribution could highlight a non-negligible amount of red noise. The opposite is not always true: short-term systematics do not necessarily lead to skewed RP residual distributions. We parametrized this "skewness" with the ratio Σ between the largest and the smallest error bar σ of a given data point:

$$\Sigma = \max\{\sigma_+, \sigma_-\} / \min\{\sigma_+, \sigma_-\} \quad (17)$$

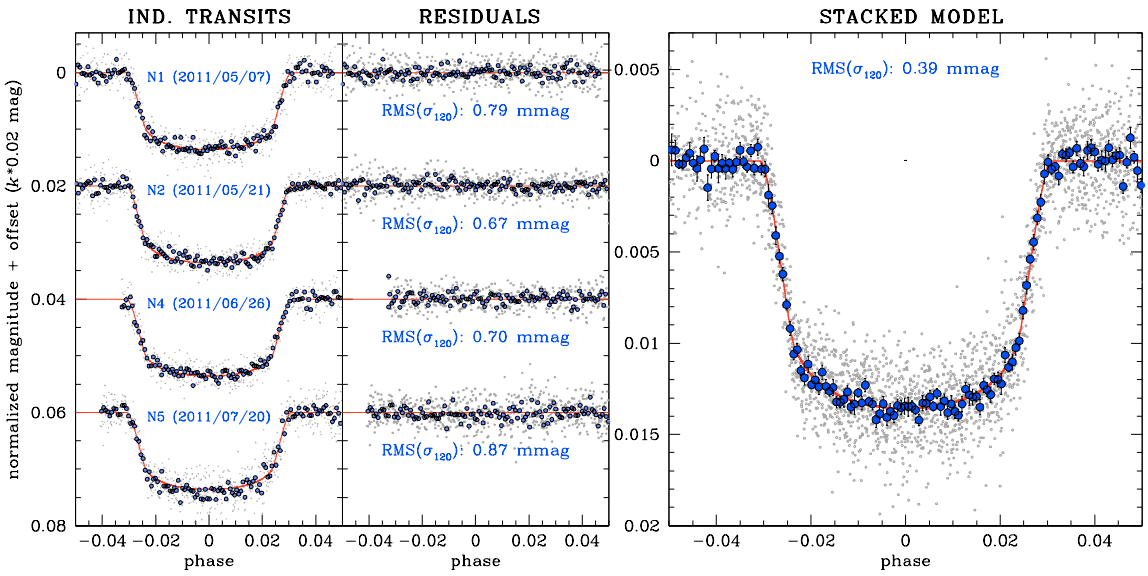

Figure 17: Construction of the best-fit model from the four best light curves of WASP-3b observed at IAC80 (on 2011 May 7, May 21, Jun 26, Jul 20). The ID# of each transit (`N1`, `N2`, `N4`, `N5`) matches the corresponding entry in Table 6. Small gray dots represent the data points with the original cadence, while blue circles are binned on 120 s intervals. The red line is the best-fit from JKTEBOP (Table 7). *Left panel:* individual light curves. Transits have been offset in magnitude by a multiple of 0.02 for clarity. *Middle panel:* Residuals from the best-fit model. The reported scatter is evaluated on the binned points as the 68.27^{th} percentile from the median value. *Right panel:* Stack of all four IAC80 light curves with the best-fit model superimposed. The derived parameters are quoted in Table 7

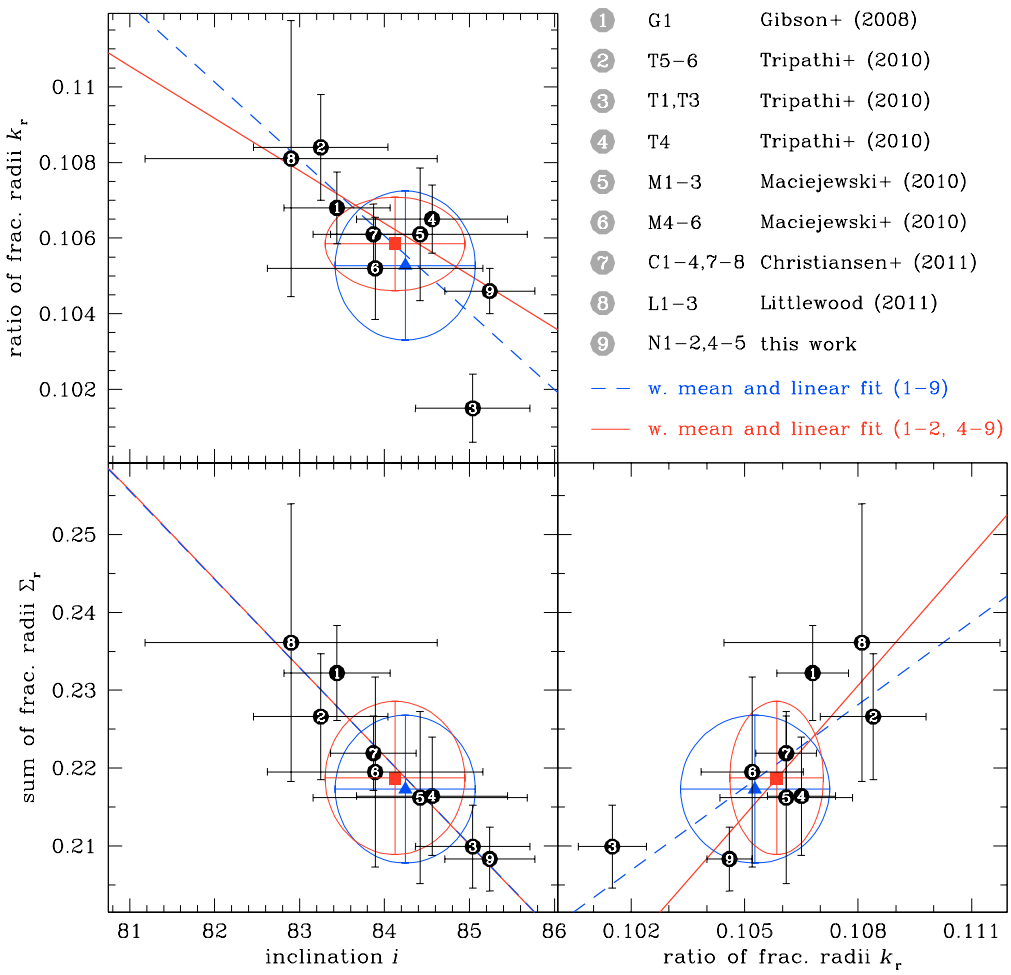

Figure 18: Geometrical parameters of WASP-3b estimated from individual data (sub-)sets (Table 7) plotted as black labeled circles in their two-dimensional parameter space, to highlight the sizeable correlation between Σ_r, k_r, and i. The blue dashed line in each plot is a weighted linear fit of all the points; the blue triangles and the associated error ellipse correspond to the weighted mean $\pm 1\sigma$ computed on the marginal distribution of Σ_r, k_r, and i (last but one row of Table 7). The red continuous line and squares are computed in the same way of the blue ones, but after removing the outlier labeled "3" from the set (`T1,T3`; last row of Table 7).

Table 7: Orbital/physical parameters of WASP-3b estimated from individual data (sub-)sets.

reference paper	N_t	telescope	ID	band	Σ_r	k_r	i	u_1	$u_{1,th}$
Gibson et al. (2008)	1	LT-2.0m	G1	$(R+V)$	$0.2322^{+0.0058}_{-0.0064}$	$0.1068^{+0.0008}_{-0.0011}$	$83°.44^{+0.66}_{-0.59}$	$0.304^{+0.069}_{-0.073}$	0.28
Tripathi et al. (2010)	2	FLWO-1.2m	T5-6	Sloan g	$0.2266^{+0.0079}_{-0.0083}$	$0.1084^{+0.0014}_{-0.0014}$	$83°.25^{+0.82}_{-0.76}$	$0.380^{+0.086}_{-0.094}$	0.42
Tripathi et al. (2010)	2	FLWO-1.2m	T1,T3	Sloan i	$0.2099^{+0.0052}_{-0.0055}$	$0.1015^{+0.0009}_{-0.0009}$	$85°.04^{+0.69}_{-0.66}$	$0.249^{+0.040}_{-0.057}$	0.18
Tripathi et al. (2010)	1	UH-2.2m	T4	Sloan z	$0.2164^{+0.0074}_{-0.0078}$	$0.1065^{+0.0007}_{-0.0011}$	$84°.56^{+0.96}_{-0.82}$	$0.141^{+0.056}_{-0.054}$	0.14
Maciejewski et al. (2010)	3	Rohzen-0.6m	M1-3	R	$0.2162^{+0.0112}_{-0.0109}$	$0.1061^{+0.0014}_{-0.0021}$	$84°.42^{+1.37}_{-1.15}$	$0.221^{+0.130}_{-0.146}$	0.24
Maciejewski et al. (2010)	3	Jena-0.9m	M4-6	R	$0.2195^{+0.0122}_{-0.0122}$	$0.1052^{+0.0014}_{-0.0013}$	$83°.89^{+1.31}_{-1.23}$	$0.095^{+0.128}_{-0.129}$	0.24
Christiansen et al. (2011)	6	HRI@EPOXI	C1-4,C7-8	clear	$0.2219^{+0.0049}_{-0.0047}$	$0.1061^{+0.0008}_{-0.0008}$	$83°.87^{+0.51}_{-0.50}$	$0.270^{+0.046}_{-0.054}$	0.28
Littlefield (2011)	3	SC-11″	L1-3	clear	$0.2361^{+0.0205}_{-0.0152}$	$0.1081^{+0.0033}_{-0.0040}$	$82°.90^{+1.53}_{-1.91}$	$0.455^{+0.158}_{-0.183}$	0.28
this work	4	IAC80	N1-2,N4-5	R	$0.2083^{+0.0040}_{-0.0042}$	$0.1046^{+0.0006}_{-0.0006}$	$85°.24^{+0.56}_{-0.50}$	$0.247^{+0.029}_{-0.028}$	0.24
$\langle$weighted mean$\rangle_1$	–	–	–	–	$0.2173^{+0.0095}_{-0.0095}$	$0.1053^{+0.0019}_{-0.0019}$	$84°.24^{+0.82}_{-0.82}$	–	–
$\langle$weighted mean$\rangle_2$	–	–	–	–	$0.2187^{+0.0098}_{-0.0098}$	$0.1058^{+0.0012}_{-0.0012}$	$84°.12^{+0.82}_{-0.82}$	–	–

The columns give: the reference paper, the number of light curves fitted, the telescope, the ID code of the transits, the filter employed, the fitted sum of the fractional radii ($\Sigma_r = R_p/a + R_\star/a$), the fitted ratio of the fractional radii ($k_r = R_p/R_\star$), the fitted inclination i, the fitted linear limb darkening (LD) coefficient u_1, and the theoretical linear LD coefficient $u_{1,th}$ interpolated from the Claret (2000, 2004) tables. The quoted error bars are derived from the JKTEBOP RP algorithm. The last two rows show the weighted means of all the previous individual estimate (1) and of all of the previous with the exception of the data set T1,T3 (see text for details).

Table 8: Central instants of WASP-3b transits estimated from all the individual light curves.

N	T_0 (mean), BJD(TDB)	T_0 (med), BJD(TDB)	Σ	O − C (s)	$\frac{(O-C)}{\sigma}$	ID	telescope	selected?
(0)	$2454143.85107 \pm 0.00040$	—	1.00	−0.00019	−0.50	-	—	no (baseline ephemeris)
248	$2454601.86671 \pm 0.00026$	$2454601.86673^{+0.00025}_{-0.00028}$	1.12	0.00038	1.48	T1	FLWO-1.2m	no (partial)
250	$2454605.56042 \pm 0.00030$	$2454605.56049^{+0.00020}_{-0.00040}$	2.00	0.00042	1.42	G1	LT-2.0m	yes
262	$2454627.72317 \pm 0.00068$	$2454627.72324^{+0.00121}_{-0.00015}$	8.07	0.00115	1.70	T2	FLWO-1.2m	no (partial)
268	$2454638.80399 \pm 0.00034$	$2454638.80400^{+0.00030}_{-0.00038}$	1.27	0.00096	2.85	T3	FLWO-1.2m	yes
280	$2454660.96479 \pm 0.00015$	$2454660.96480^{+0.00015}_{-0.00015}$	1.00	−0.00025	−1.68	T4	UH-2.2m	yes
290	$2454679.43318 \pm 0.00042$	$2454679.43311^{+0.00055}_{-0.00029}$	1.90	−0.00021	−0.50	C1	HRI@EPOXI	yes
291	$2454681.27967 \pm 0.00034$	$2454681.27963^{+0.00038}_{-0.00031}$	1.23	−0.00055	−1.63	C2	HRI@EPOXI	yes
292	$2454683.12798 \pm 0.00049$	$2454683.12800^{+0.00047}_{-0.00051}$	1.09	0.00092	1.88	C3	HRI@EPOXI	yes
293	$2454684.97524 \pm 0.00040$	$2454684.97521^{+0.00042}_{-0.00038}$	1.11	0.00134	3.36	C4	HRI@EPOXI	yes
294	$2454686.82144 \pm 0.00074$	$2454686.82140^{+0.00102}_{-0.00047}$	2.17	0.00071	0.96	C5	HRI@EPOXI	no (partial)
296	$2454690.51475 \pm 0.00059$	$2454690.51480^{+0.00048}_{-0.00070}$	1.46	0.00035	0.59	C6	HRI@EPOXI	no (partial)
297	$2454692.36168 \pm 0.00056$	$2454692.36173^{+0.00047}_{-0.00064}$	1.36	0.00044	0.79	C7	HRI@EPOXI	yes
298	$2454694.20776 \pm 0.00083$	$2454694.20770^{+0.00090}_{-0.00075}$	1.20	−0.00031	−0.37	C8	HRI@EPOXI	yes
308	$2454712.67641 \pm 0.00064$	$2454712.67637^{+0.00066}_{-0.00062}$	1.06	−0.00000	−0.01	U1	UDEM-0.36m	yes
309	$2454714.52368 \pm 0.00041$	$2454714.52358^{+0.00063}_{-0.00020}$	3.15	0.00042	1.04	G2	LT-2.0m	no (partial)
433	$2454943.53240 \pm 0.00060$	$2454943.53249^{+0.00045}_{-0.00074}$	1.64	0.00161	2.70	E1	Newton-0.2m	yes
444 ⋆	$2454963.84450 \pm 0.00081$	$2454963.84453^{+0.00087}_{-0.00075}$	1.16	−0.00146	−1.81	T5	FLWO-1.2m	yes
444 ⋆	$2454963.84527 \pm 0.00118$	$2454963.84541^{+0.00102}_{-0.00134}$	1.31	−0.00069	−0.59	S1	VCT-0.5m	yes
446	$2454967.53905 \pm 0.00070$	$2454967.53912^{+0.00061}_{-0.00079}$	1.30	−0.00058	−0.84	E2	SC-12″	yes
451	$2454976.77284 \pm 0.00030$	$2454976.77283^{+0.00032}_{-0.00028}$	1.14	−0.00097	−3.23	T6	FLWO-1.2m	yes
457	$2454987.85256 \pm 0.00093$	$2454987.85267^{+0.00071}_{-0.00116}$	1.63	−0.00225	−2.43	U2	UDEM-0.36m	yes
484	$2455037.71878 \pm 0.00086$	$2455037.71877^{+0.00085}_{-0.00086}$	1.01	−0.00058	−0.68	U3	UDEM-0.36m	yes
486 ⋆	$2455041.41172 \pm 0.00035$	$2455041.41172^{+0.00036}_{-0.00035}$	1.03	−0.00131	−3.75	D1	OAVdA-0.25m	yes
486 ⋆	$2455041.41255 \pm 0.00058$	$2455041.41246^{+0.00053}_{-0.00063}$	1.19	−0.00048	−0.83	M1	Rohzen-0.6m	yes
488	$2455045.10565 \pm 0.00106$	$2455045.10557^{+0.00112}_{-0.00100}$	1.12	−0.00105	−0.99	Z1	Weihai-1m	no (low S/N)
490	$2455048.80065 \pm 0.00107$	$2455048.80066^{+0.00104}_{-0.00110}$	1.06	0.00027	0.26	U4	UDEM-0.36m	no (red noise)
499	$2455065.42023 \pm 0.00036$	$2455065.42026^{+0.00038}_{-0.00034}$	1.12	−0.00165	−4.60	M2	Rohzen-0.6m	yes
506	$2455078.34809 \pm 0.00114$	$2455078.34799^{+0.00133}_{-0.00096}$	1.39	−0.00163	−1.44	M3	Rohzen-0.6m	yes
519	$2455102.36030 \pm 0.00084$	$2455102.36037^{+0.00061}_{-0.00107}$	1.75	0.00171	2.04	M4	Jena-0.9m	yes
539	$2455139.29753 \pm 0.00073$	$2455139.29719^{+0.00111}_{-0.00034}$	3.26	0.00224	3.08	M5	Jena-0.9m	yes
629	$2455305.51117 \pm 0.00056$	$2455305.51119^{+0.00049}_{-0.00063}$	1.29	0.00074	1.34	M6	Jena-0.9m	yes
653 ⋆	$2455349.83306 \pm 0.00090$	$2455349.83316^{+0.00085}_{-0.00096}$	1.13	−0.00140	−1.56	S3	VCT-0.5m	yes
653 ⋆	$2455349.83390 \pm 0.00069$	$2455349.83384^{+0.00069}_{-0.00069}$	1.00	−0.00056	−0.81	S2	KPNO-2.0m	yes
653 ⋆	$2455349.83434 \pm 0.00054$	$2455349.83430^{+0.00061}_{-0.00047}$	1.30	−0.00012	−0.22	E3	SC-12″	yes
654	$2455351.68410 \pm 0.00155$	$2455351.68399^{+0.00151}_{-0.00159}$	1.05	0.00280	1.81	L1	SC-11″	no (red noise)
666	$2455373.84289 \pm 0.00045$	$2455373.84285^{+0.00048}_{-0.00043}$	1.12	−0.00042	−0.94	E4	Newton-0.3m	yes
686	$2455410.78073 \pm 0.00173$	$2455410.78083^{+0.00148}_{-0.00199}$	1.34	0.00071	0.42	L2	SC-11″	no (red noise)
693	$2455423.70889 \pm 0.00048$	$2455423.70891^{+0.00050}_{-0.00047}$	1.06	0.00103	2.15	U5	UDEM-0.36m	yes
699	$2455434.78772 \pm 0.00051$	$2455434.78775^{+0.00041}_{-0.00060}$	1.46	−0.00114	−2.25	E5	RC-12.5″	yes
706	$2455447.71600 \pm 0.00117$	$2455447.71628^{+0.00051}_{-0.00184}$	3.61	−0.00071	−0.61	L3	SC-11″	yes (red noise)
837	$2455689.65263 \pm 0.00015$	$2455689.65263^{+0.00014}_{-0.00016}$	1.14	0.00054	3.66	N1	IAC-0.8m	yes
838	$2455691.49899 \pm 0.00064$	$2455691.49899^{+0.00071}_{-0.00056}$	1.27	0.00007	0.11	E6	Monteboo-0.6m	yes
842	$2455698.88476 \pm 0.00160$	$2455698.88463^{+0.00174}_{-0.00147}$	1.18	−0.00149	−0.94	S4	VCT-0.5m	yes
844	$2455702.58052 \pm 0.00028$	$2455702.58051^{+0.00029}_{-0.00028}$	1.04	0.00059	2.12	N2	IAC-0.8m	yes
849	$2455711.81615 \pm 0.00107$	$2455711.81617^{+0.00094}_{-0.00120}$	1.28	0.00204	1.92	E7	RC-12″	no (low S/N)
851	$2455715.50882 \pm 0.00057$	$2455715.50853^{+0.00051}_{-0.00063}$	1.24	0.00105	1.84	N3	IAC-0.8m	no (low S/N)
864	$2455739.51620 \pm 0.00017$	$2455739.51620^{+0.00015}_{-0.00018}$	1.20	−0.00042	−2.49	N4	IAC-0.8m	yes
877	$2455763.52511 \pm 0.00031$	$2455763.52511^{+0.00030}_{-0.00032}$	1.07	−0.00036	−1.19	N5	IAC-0.8m	yes
884	$2455776.45192 \pm 0.00089$	$2455776.45192^{+0.00093}_{-0.00085}$	1.09	−0.00140	−1.58	N6	IAC-0.8m	no (red noise)

The columns give: the transit epoch N assuming $T = T_0 + NP$ and the original ephemeris from Pollacco et al. (2008), the best-fit value for the central instant T_0 of the transit and the associated σ, the median value of the distribution of T_0 from the Residual Permutation (RP) algorithm and the associated errors σ_+ and σ_-, the "skew" parameter $\Sigma = \max\{\sigma_+, \sigma_-\}/\min\{\sigma_+, \sigma_-\}$, the O − C according to the new ephemeris (Eq. 18) in seconds, the O − C in units of σ, the ID code of the light curve, the telescope employed, and comments about whether and why the data point is excluded from the "selected" sample. Simultaneous transits are marked with a star in the first column.

In principle, $\Sigma \simeq 1$ for well-behaved transits, and $\Sigma \gg 1$ for transits dominated by long-term systematics. Table 8 lists Σ for all the employed T_0. We found $1.01 < \Sigma < 1.63$ for the eleven TASTE transits (`N1-6`, `U1-5`). Instead, a few archival data points show unusually large values (e.g., $\Sigma = 8.07$ for `T2`). We investigated this issue by comparing the most significant T_0 published in the literature (`T1-5`; `G1-2`; `C1-8`; `M1-6`) with those derived by our reanalysis (Fig. 19, third panel from the top). We concluded that the vast majority of the published estimate agree within the error bars with ours. Notable exceptions are `T1`, `T2`, and `G2`: they all are *partial* transits, and `T2`, `G2` have also large Σ. This is exactly what we expected. It indeed demonstrates that when a light curve lacks the off-transit part, its normalization becomes tricky, and even a very small difference in the adopted technique can lead to significantly different T_0 measurements. For this reason, partial transits should be included with extreme caution in a TTV analysis. We note that, on average, our error bars are larger than the published ones –sometimes by a factor of two– confirming our concern that most measurements carried out in the past have been published with underestimated errors due to neglected red noise.

We considered two different samples of measurements for our TTV analysis. The first ("`ALL`") includes all the 49 T_0 listed in Table 8, plus the T_0 from the ephemeris Eq. (11) from Pollacco et al. (2008). The second sample ("`SELECTED`") is a high-quality subset of 36 values, selected by excluding Eq. (11) (it does not correspond to an independent measurement of one single transit) and other 13 data points extracted from partial transits or from light curves with a too low S/N or with clear signs of red noise. The transits excluded from `SELECTED` are listed in Table 8 along with the reason for the exclusion.

The first step to plot an $O-C$ diagram is to calculate a "reference" linear ephemeris to predict T_0 at any given epoch. We set the new zero epoch at `N2`, i.e. our most accurate light curve. The `ALL` sample was employed to fit a linear model by ordinary weighted least squares, obtaining

$$\begin{aligned} T_0(\mathrm{BJD_{TDB}}) &= 2\,455\,702.57993 \pm 0.00017 + \\ &\quad + N \cdot 1.8468349 \pm 0.0000004 \end{aligned} \tag{18}$$

The uncertainties have been evaluated from the covariance matrix of the fit, and were both rescaled by $\sqrt{\chi^2_r}$ to take into account the real dispersion of the data points around our best-fit ephemeris. In Fig. 19 are plotted the $O-C$ diagrams for `ALL` (first panel from top) and `SELECTED` samples (second panel, with a smaller baseline). In both diagrams, the reduced $\chi^2_r = 3.7$-4.5 suggests that the measurements are not in full agreement with the linear ephemeris in Eq. (18). Yet, there is no evident periodic pattern in our diagrams. We investigated the possibility that this statistically significant scatter is caused by a

genuine TTV, either the TTV claimed by Maciejewski et al. (2010) or a different one.

We exploited two algorithms to search for periodic signals: the Generalised Lomb-Scargle periodogram (GLS; Zechmeister & Kürster 2009) and the "Fast χ^2" algorithm (Fχ^2; Palmer 2009). Both these techniques are able to deal with irregularly sampled data with nonuniform weights, and minimize aliasing effects due to the window function. In addition to this, Fχ^2 can also search for an arbitrary number of harmonics.

We searched for periodic signals with GLS in the period range P = 4-1000 d, the lower limit being imposed by the Nyquist sampling criterion to avoid aliasing (Horne & Baliunas 1986). The resulting periodograms for both samples are plotted in the fourth panel of Fig. 19. In neither case a prominent peak is visible. The `ALL` and `SELECTED` periodograms are quite similar, and their highest peaks stand at $P(\mathtt{A}) \simeq 6.41$ d and $P(\mathtt{S}) \simeq 11.29$ d, respectively. We folded the $O-C$ diagram on these two periods in the left and right plot of the fifth panel in Fig. 19, respectively. We investigated whether these peaks are statistically significant or not with a resampling algorithm. We generated 10 000 synthetic $O-C$ diagrams with the same temporal coordinates of actual data points, by randomly scrambling the $O-C$ values at each generation. A GLS periodogram was then evaluated on each of them with the same settings of that applied on real data. The power of the highest peak found in the real data for `ALL` and `SELECTED` samples lies respectively at the 12^{th} (-1.17σ) and 38^{th} percentile (-0.31σ) of the distribution of the maximum-power peaks in the synthetic, randomly-permutated diagrams. We conclude that neither peaks can be considered as statistically significant. In particular, the $P(\mathtt{M}) \simeq 127$ days periodicity claimed by Maciejewski et al. (2010) is not consistent with our data. Instead of a peak, the periodogram range where the $P(\mathtt{M})$ peak is expected is characterized by an extremely low GLS power (fourth panel of Fig. 19, blue region).

We set Fχ^2 to search for periodicities with one or two harmonics in the same frequency range. Results from both samples are quite similar to those obtained above with GLS, with non-significant power peaks at periods very close to those previously found in the BLS periodogram.

We carried out our analysis also on a subset of data points corresponding to those analyzed by Maciejewski et al. (2010), by employing the same tools used for our full data set (Fig. 20). When plotted adopting the same frequency limits, the resulting periodogram (and the peak corresponding to the maximum power) match perfectly those published by Maciejewski et al. (2010) (upper right panel of Fig. 20). On the other hand, the upper limit in frequency set by Maciejewski et al. (2010) (0.038 P^{-1}) is too low according to the Nyquist criterion. In the range $0.038 < \nu < 0.5\ P^{-1}$ many other maxima are

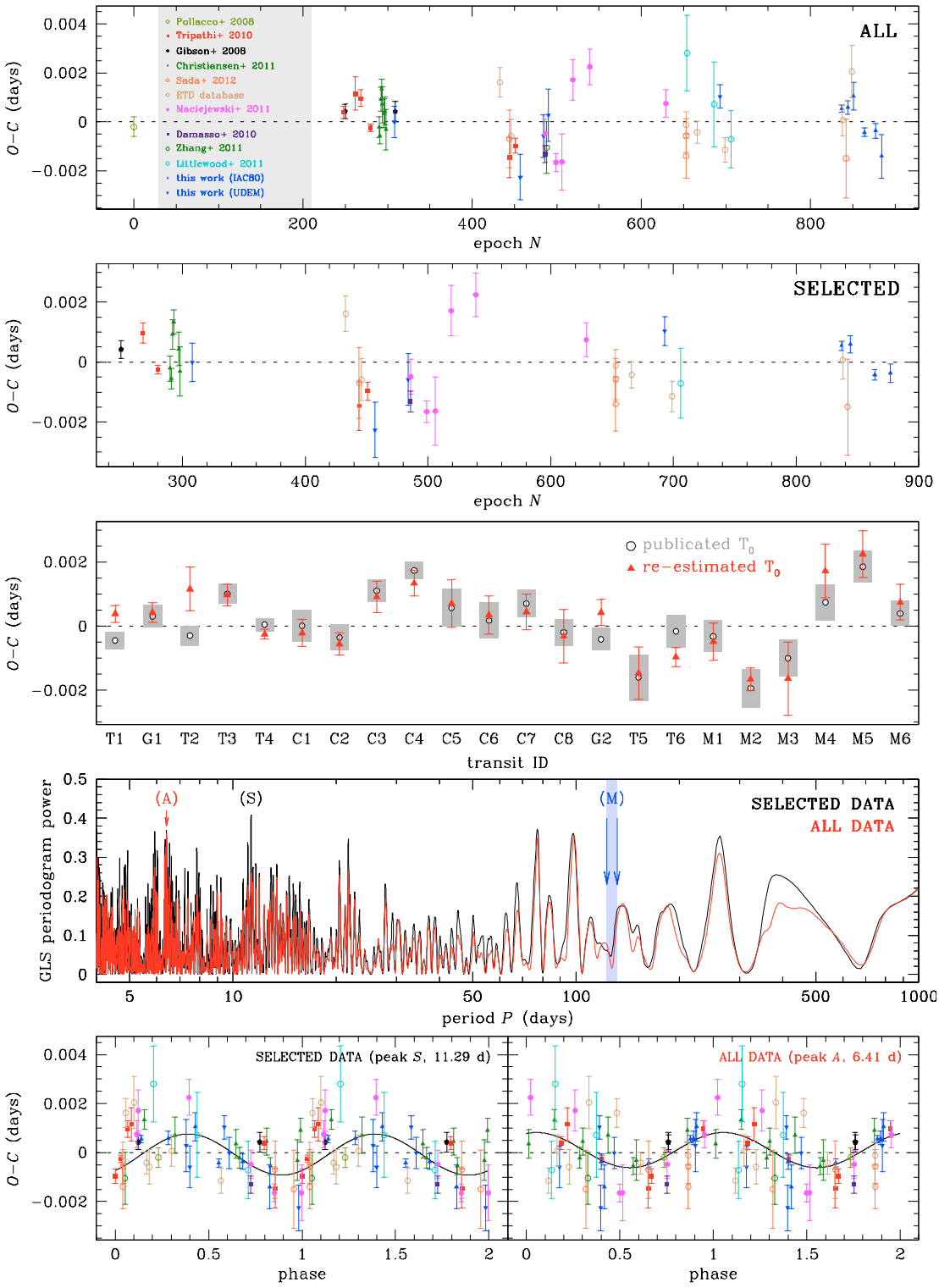

Figure 19: *First panel from the top:* O − C diagram for all the data points tabulated in Table 8. *Second panel:* same as above, for points selected as in the last column of Table 8. *Third panel:* Comparison between the original T_0 published by the respective authors (white circles with gray error bars; Table 6) and as re-estimated in this work (red triangles and bars), for the subset of high-precision light curves identified in the horizontal axis. *Fourth panel* GLS periodogram for the complete sample (red line, highest peak at A) and the selected sample (black line, highest peak at S). The periodicity claimed by Maciejewski et al. (2010) is marked with the M label. *Fifth panel* the O − C diagram folded over the most powerful peak in the SELECTED subset (left plot) and in the ALL data set.

as high as the 0.0145 P^{-1} peak (lower panel of Fig. 20). Following a stastistical test similar to that one described above, we discard that peak as not significant, being due to small-sample statistics.

4.6 DISCUSSION AND CONCLUSIONS

In the present study, we analyzed eleven unpublished light curves of WASP-3b and re-analyzed other thirty-eight archival light curves, all of them with the same software tools and procedures. We derived improved orbital and physical parameters for this target (Table 7), and computed a refined ephemeris (Eq. 18). All the individual measurements of the central instant T_0 have been compared with the new ephemeris to search for changes in the orbital period P of the transiting planet. We concluded that available observations of WASP-3b, spanning more than four years, are not consistent with a linear ephemeris ($\chi^2_r \simeq 4$). A possible explanation for this scatter is the presence of a perturbing body in the WASP-3 planetary system.

It is known that the impact of red noise on high-precision transit photometry is still not fully understood. Previous claims of TTVs have been disproved on this basis (Southworth et al. 2012; Fulton et al. 2011). Could the observed scatter in the $O-C$ diagram of WASP-3b be explained in terms of underestimated observational errors or calibration issues? The absolute time calibration of each archival light curve cannot be independently checked. In principle one should trust the authors about that. However, we point out two main clues supporting the auto-consistence of the overall data, and hence the hypothesis of a genuine TTV:

- on three different epochs ($N = 444$, 486, 653 following the Pollacco et al. 2008 ephemeris) multiple observations of the same transit are available. As they were carried out by different authors at different facilities, they should represent independent measurements of the same quantity. All these data points (marked with a star in the first column of Table 8) agree with each other within their 1σ error bars, suggesting that the uncertainties on T_0 are correctly evaluated by our pipeline;

- some anomalous patterns in the $O-C$ diagrams are confirmed by several different data sets. For instance, nearly *all* the points gathered in 2009 within the range $N = 440$-510 lie ahead of the T_0 predicted by our baseline ephemeris ($O-C < 0$). The only exception is U4, which essentially lies at $O-C \sim 0$ within its error bar. The weighted mean of these twelve measurements from eight different authors is $O-C = -0.00118 \pm 0.00016$ days. This implies a 7.2σ deviation from a constant orbital period. These patterns can also be detected in high-precision data subsets, such as our ones. Among the four best IAC80 transits, the first

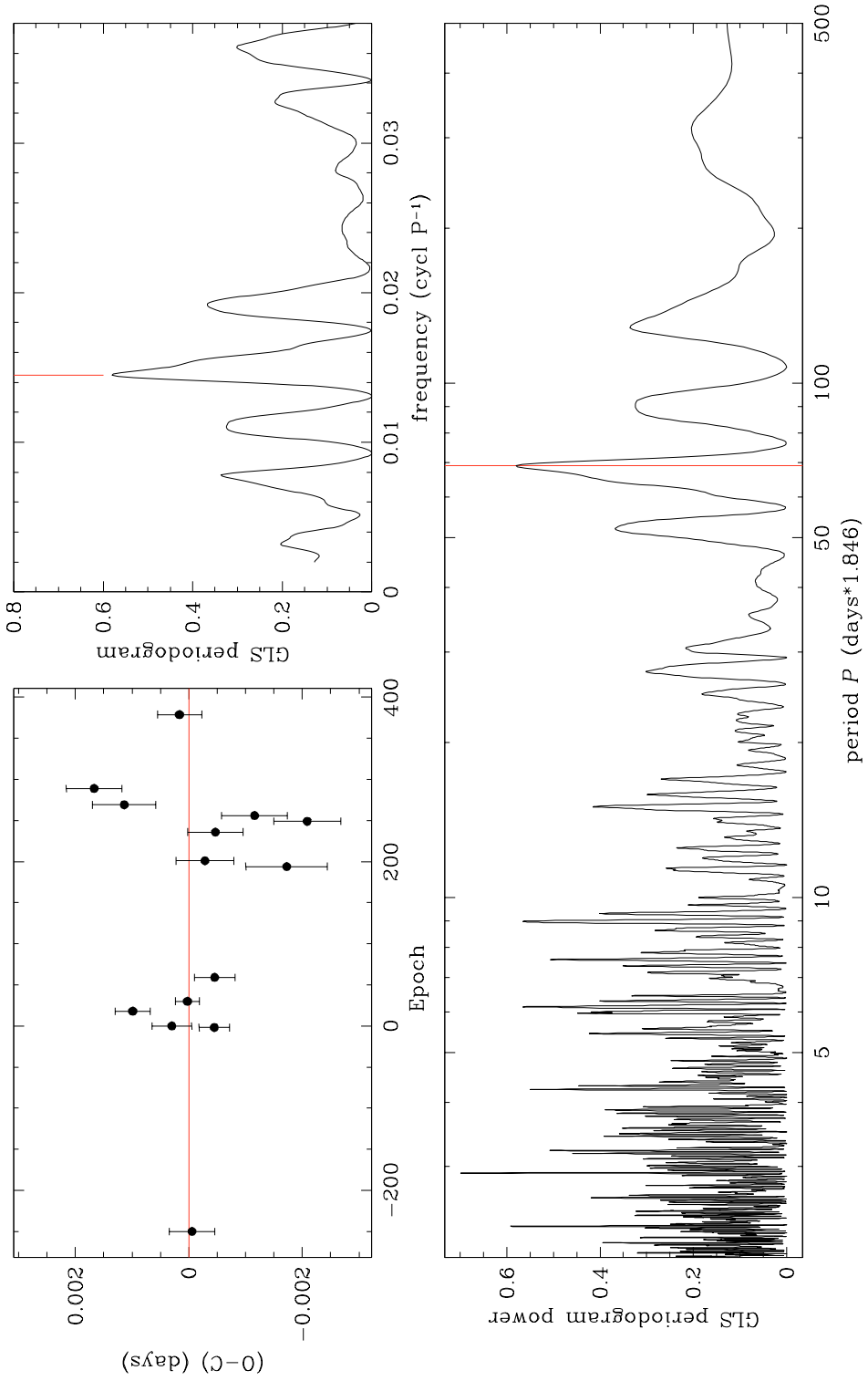

Figure 20: Period analysis carried out on the same set of O − C data points analyzed by Maciejewski et al. (2010). *Upper left panel:* O − C diagram for the selected points. *Upper right panel:* GLS periodogram as a function of frequency ν, adopting the same plotting limits of Maciejewski et al. (2010). *Bottom panel:* GLS periodogram as a function of period, adopting wider limits on frequency according to the Nyquist criterion (see text for details). The red vertical line marks the peak claimed by Maciejewski et al. (2010).

two (N1-2) are delayed by 4.3σ (i.e. $O-C = 48 \pm 11$ s) compared with the prediction, while the second two (N4-5) are ahead of the ephemeris by 2.8σ ($O-C = 35 \pm 13$ s).

The available data thus strongly suggest an intrinsic deviation of the actual transit times from the linear ephemeris expected from a Keplerian two-body transiting system. Our analysis rules out the periodic TTV claimed by Maciejewski et al. (2010), and failed even at detecting any significant periodicity in the updated $O-C$ diagram. Most TTV studies carried out in the past searched for a periodic signal, but here we are dealing with a more complex and non-periodic phenomenon, at least at the time scales we sampled. What kind of dynamical system can induce such a perturbation?

Veras et al. (2011) demonstrated that some orbital configurations, especially close to (but not exactly in) mean-motion resonances, can induce quasi-periodic or even chaotic TTVs. In other non-exotic configurations, the periodicity would manifest itself only at time scales > 10 yr (Veras et al. 2011). Also when more than one pertuber are present and their orbital periods are not commensurable, as in the case of our inner Solar System, the resulting TTV would be in general aperiodic (Holman & Murray 2005).

If WASP-3b belongs to one of the above-mentioned cases, careful dynamical modeling and additional follow-up is required to confirm the hypothesis and to constrain the mass and period of the possible perturber(s). Photometric monitoring is still ongoing within the TASTE project, and high-precision RV measurements are foreseen with HARPS-N. As stressed out by Meschiari & Laughlin (2010) and Payne & Ford (2011), photometric TTVs and RVs are highly complementary in breaking the degeneracies that are common in the inverse dynamical problem.

Acknowledgements

This work was partially supported by PRIN INAF 2008 "Environmental effects in the formation and evolution of extrasolar planetary system". V. N. and G. P. acknowledge partial support by the Università di Padova through the "progetto di Ateneo #CPDA103591". V. G. acknowledges support from PRIN INAF 2010 "Planetary system at young ages and the interactions with their active host stars". Some tasks of our data analysis have been carried out with the VARTOOLS (Hartman et al. 2008) and `Astrometry.net` codes (Lang et al. 2010). This research has made use of the International Variable Star Index (VSX) database, operated at AAVSO, Cambridge, Massachusetts, USA.

5

IMPROVEMENTS OF THE PARAMETERS OF HAT-P-20B AND WASP-1B

In this chapter I will analyze four high-precision light curves caught serendipitously at the Asiago 1.82m telescopes (one of WASP-1b, three of HAT-P-20b). By also re-analyzing the most accurate archival data available, I will derive improved parameters and ephemeris for both targets, which do not show any significant TTV. I will discuss what upper limits can be set from this null detection to the mass of hypotetical perturbing planets.

This chapter will be based on: V. Granata, V. Nascimbeni, G. Piotto, L. R. Bedin, L. Borsato, M. Damasso, L. Malavolta (2012) *TASTE IV. Refined ephemeris and parameters for WASP-1b and HAT-P-20b*, A&A, in preparation.

5.1 INTRODUCTION

Most planets are extremely faint light sources compared to their parent star. In addition to the intrinsic difficulty of detecting such a feeble source, the light from the host star causes a glare that washes it out. For those reasons, only $\sim 4\%$ of the extrasolar planets known up to 2012 have been observed directly and astronomers had to resort to indirect detection methods. One of the most promising is the transit technique paired up to the Transit Timing Variation method (TTV). It is well-known that a planet transiting on its star in a Keplerian orbit produces a signal with a precise cadence only if it is unperturbed by other bodies. If a third companion is present, transits are no longer exactly periodic (Holman & Murray 2005). The mass of the perturber can be inferred by measuring the timing deviations of the central instants of the light curve from the expected ephemeris (Agol et al. 2005).

The TASTE project (originally *The Asiago Search for Transit Timing variations of Exoplanets*; Nascimbeni et al. 2011b) is focused on the TTV method. The aim of the program is to collect a database of high-precision light curves to be analyzed in search for timing variations exploiting the Asiago Observatory[1] (Nascimbeni et al. 2011c) and, more recently, other medium-class facilities around the world.

In this work, we present one new transit light curve of WASP-1b and three more of HAT-P-20b, performing a TTV analysis (never faced so far on these targets) and re-analyzing data published from different authors in order to provide a new reference ephemeris for

1 http://www.pd.astro.it/asiago/

both planets. The new transits were observed with the Asiago 1.82m "Copernico" telescope employing the AFOSC + Andor iKon DW436-BV imager with an E2V 42-20 CCD detector. A complete description of TASTE instrumental setup, observing strategy, data reduction/-analysis process, and the monitored sample can be found in Nascimbeni et al. (2011b). The two serendipitous objects of this study have not been included in the first TASTE sample for different reasons: WASP-1b transits have a duration longer than the 200-minute constraint and HAT-P-20b had not been yet discovered at the time of the first target selection (Nascimbeni et al. 2011b).

WASP-1b was discovered by Collier Cameron et al. (2007) within the SuperWASP survey and its parameters were subsequently refined with follow-up photometry by Charbonneau et al. (2007), Shporer et al. (2007) and Sada et al. (2012). It is a "hot Jupiter" transiting an F7V host star (WASP $V = 11.79$) with a period of $P = 2.51995 \pm 0.001$ days, a radius of $R_p \simeq 1.3\ R_{jup}$, and a derived mass of $M_p \simeq 0.86\ M_{jup}$, as reported in the discovery paper. Its $B - V = 0.75$ color is derived from SIMBAD[2] database.

HAT-P-20b is a massive and extremely dense transiting exoplanet ($M_p \simeq 7.2 M_{jup}$, $R_p \simeq 0.87\ R_{jup}$, $V - I_C = 1.50 \pm 0.12$) orbiting around a $V = 11.339$ K3 central star with a period of $P = 2.875317 \pm 0.000004$. The parent star is the primary component of a visual binary system (Bakos et al. 2011). The secondary component HAT-P-20 B is a red dwarf at $\sim 7''$ from HAT-P-20 A and is fainter by $\Delta R = 1.36$ mag.

In Section 5.2 we briefly summarize our new observations, Section 5.3 describes the archival data and the homogeneous approach applied to all the analyzed light curves, Section 5.4 discusses data analysis, and Section 5.5 presents the results from our study.

5.2 OBSERVATIONS

We observed WASP-1b at the predicted transit time on the night of 2010 November 29, while HAT-P-20b was observed in three different nights, on 2011 February 5, November 28, and December 22. For all four photometric series, we employed a Cousins R filter to maximize the number of detected photons and, at the same time, to minimize both atmospheric extinction and limb darkening effects. We read the detector in 4×4-binning mode in order to increase the readout speed and thus the efficiency. For the same reason the detector was windowed, since the reference stars fill up only a part of the field of view. The chosen CCD window spanned all physical pixels along the x axis and only a portion along y: from $\Delta y = 607$ pixels for the WASP-1b transit to $\Delta y = 599$ pixel for HAT-P-20b. Archival finding-charts for WASP-1 and HAT-P-20 (circled in blue) and reference stars (circled in

2 http://simbad.u-strasbg.fr/simbad/

magenta) are given in Figure 21. The adopted AFOSC-FOV windows are highlighted.

Exposure time was set to 5 s for WASP-1b, and between 2 and 4 s for HAT-P-20b. The average duty-cycle spanned from 47% to 74%, and the resulting cadence 4.3-7.4 s. Despite the auto-guide, in all four observing nights we experienced a pointing drift of about 1 pixel along x-axis and up to more than 2 pixels along y. However, this problem did not affect our photometry as it can be seen in Section 5.3.

Some veils were constantly present during the WASP-1 transit. Stellar images were defocused to a FWHM of $\sim$ 5-8″ pixels to prevent saturation and minimize pixel-to-pixel systematic errors. As for the HAT-P-20b time series, on 2011 February 5 few veils appeared at the end of the observations ($>$ 200 min from the start, after the last contact) and the FWHM of the images was set to $\sim$ 4-6″ pixels. On 2011 November 28 the sky was clear except for the off-transit part after the last contact (150-200 min from the start), and the mean FWHM was 4″ pixels. On 2011 December 22 clouds affected the series in the first 20 minutes before the ingress and during the second half of the transit. FWHM spanned from $\sim$ 4″ to occasionally 7″ pixels due to focus changes. Dome-flat fields and bias frames have been secured both at the beginning and at the end of the scientific series to correct instrumental drifts arisen during the sequences.

The summarizing observation log for WASP-1b is given in the last row of Table **??** for WASP-1b and for HAT-P-20b are given in the last three entries of Table 11. For a detailed explanation of the instrumental setup and observational strategy, refer to Nascimbeni et al. (2011b).

5.3 DATA REDUCTION

Data analysis for both targets was performed using the STARSKY (Nascimbeni et al. 2011b) reduction pipeline, based on differential aperture photometry. The differential approach is necessary in order to correct first-order systematics caused by atmospheric or instrumental sources.

As dark current is negligible on AFOSC for bright targets imaged in very short exposures, we applied only bias and flat-field corrections in the pre-reduction phase. As no instrumentals drifts were noticeable, we constructed master frames by combining bias and flats acquired at two distinct epochs. After sky subtraction, we estimated the target flux for a set of photometric apertures and normalized it to the weighted average of a set of reference stars. Four isolated comparison stars have been selected for WASP-1b and four were chosen for the first and third transit of HAT-P-20b, and only one for the third transit (2011 November 28). As for the latter, the differential light curve of HAT-P-20 A showed a systematic error due to contaminat-

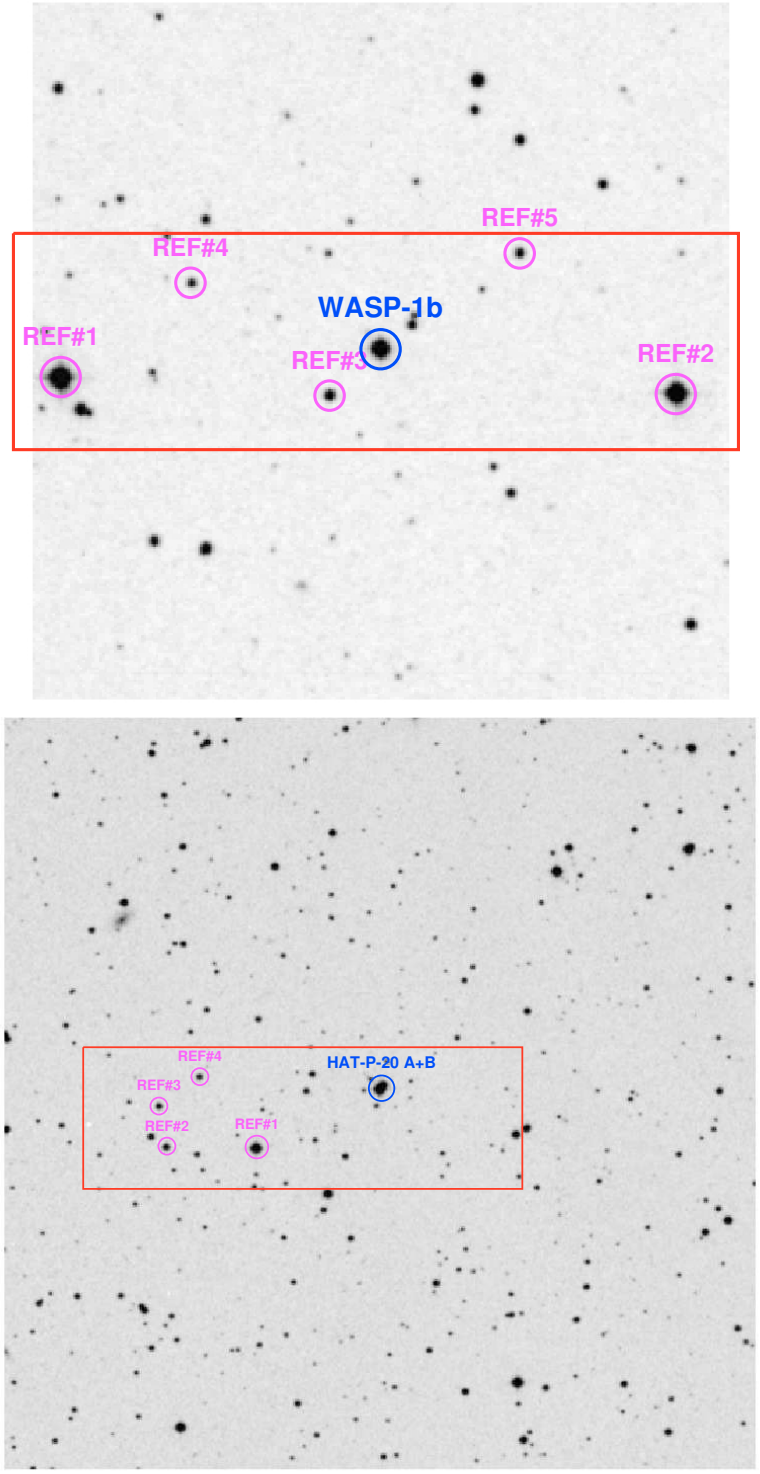

Figure 21: *Upper panel*: An $8' \times 8'$ image from ESO-DSS-DR1 centered on WASP-1 (blue circle). North is on the left, East is up. For reference, the magenta circles highlight the brightest stars in the field used as references. *Lower panel*: A $15' \times 15'$ image from ESO-DSS centered on HAT-P-20 (blue circle). North is up, East is on the right. For reference, the magenta circles highlight the brightest stars in the field used as references. The selected AFOSC windowed-FOV (red square) is also shown in both panel.

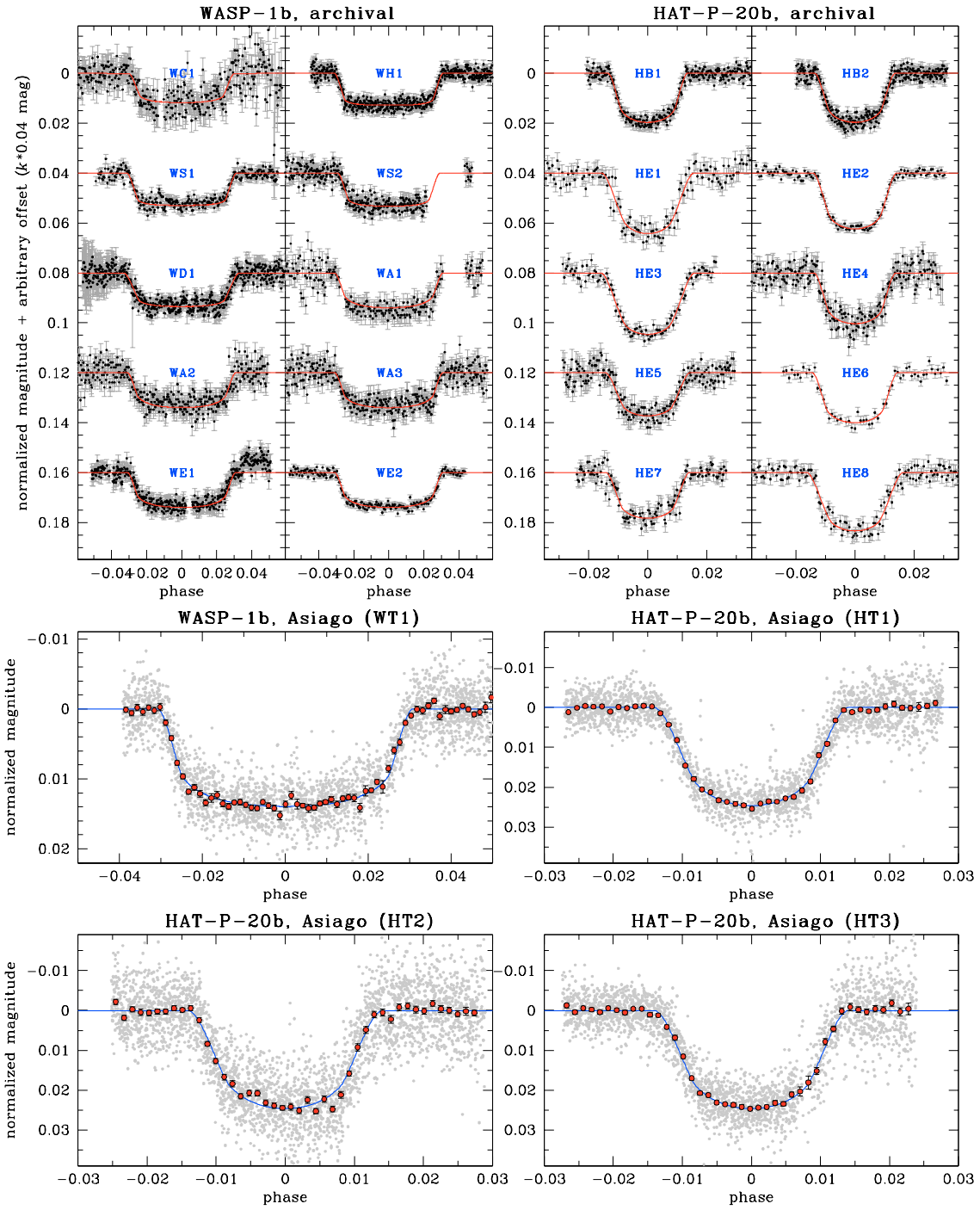

Figure 22: Light curves of WASP-1b and HAT-P-20b analyzed in the present work, plotted as a function of the orbital phase. The ID codes in each title match those defined in Tables 9 and 11 for WASP-1b and HAT-P-20b, respectively. The continuous line is the best-fit model found by JKTEBOP. *Upper half*: archival light curves of WASP-1b (at left) and HAT-P-20b (at right). Data are plotted with a fixed 0.04 magnitude offset for clarity. *Lower half*: new TASTE transits of WASP-1b (`WT1`) and HAT-P-20b (`HT1`, `HT2`, `HT3`) acquired at the Asiago 1.82m Copernico telescope. Gray dots represent the original unbinned points, while red dots are binned on 2-min intervals. Error bars on the latter are computed as the standard photometric error of residuals to the model within each bin.

ing flux coming from the close HAT-P-20 B. We re-evaluated the light curve with an oversized aperture, to include all the light from both sources. Then we estimated the flux ratio between A and B components ($f_B/f_A = 0.1524 \pm 0.0011$, corresponding to a dilution factor of about 87%) and applied a correction to the restore the true transit depth. *Ad hoc* routines handled correction for systematic errors as function of airmass, centroid positions, FWHM, and other quantities of interest, as described in (Nascimbeni et al. 2011b).

Employing `JKTEBOP` code[3] version 25 (Southworth et al. 2004) we fitted a transit model to our light curves fixing the quadratic limb darkening coefficient u_2 to its theoretical value, while linear parameter u_1 was guessed, as proposed by Southworth (2010b). This choice turned out to be the best approach, providing the minimum reduced χ^2 value and estimating realistic uncertainties on fitted parameters. We took theoretical limb darkening coefficients from the `JKTLD` code[4], i. e. interpolating the Claret (2000) tables compiled from the ATLAS atmosphere model. The resulting inclination i, ratio of fractional radii $R_p/R_\star$, and sum of fractional radii $(R_p + R_\star)/a$ were then fitted on photometric series along with u_1 and the central transit time T_0. Based on a residual-shift (also known as "prayer bead") method, the used algorithm takes into account the presence of red noise in the light curve, by propagating any systematic error along the series while preserving its structure. The resulting light curves, normalized to their off-transit magnitude, are shown in Fig. 22 (large panels at bottom) for both targets. For WASP-1b, the photometric scatter is $\sigma_u = 2.6$ mmag (unbinned points) corresponding to $\sigma_{120} = 0.8$ mmag (2-min binned). For HAT-P-20b, σ_u is within the range 3.41-4.99 mmag, while the 2-min binned RMS σ_{120} is within 0.8-1.2 mmag.

Using `JKTEBOP`, we also re-analyzed all the archival data published in the refereed literature, and –after a careful selection– also some light curves by amateur astronomers stored in the ETD[5] and AXA[6] archives. Table 9 and Table 11 summarize relevant informations about the whole data set. A unique three-character ID code is assigned to each light curve. In this analysis we discarded the Szabó et al. (2010) observation of WASP-1b because its published T_0 is in disagreement by $> 6\,\sigma$ with other professional measurements carried out in the same season, as already pointed out by Sada et al. (2012). **?** data of HAT-P-20b are also excluded from this study because they gathered partial transit due to bad weather conditions. In some cases, archival light curves were secured using filters other than R, or without filter (being referred as "Clear" in Tables 9 and 11): in the former case we interpolated the limb darkening coefficients for the corresponding from the Claret (2000, 2004) tables as above; in the latter, we computed

3 http://www.astro.keele.ac.uk/ jkt/codes/jktebop.html

4 http://www.astro.keele.ac.uk/jkt/codes/jktld.html

5 http://var2.astro.cz/ETD/index.php

6 http://nsted.ipac.caltech.edu/NStED/docs/datasethelp/AXA.html

the average value between V and R bands given by Claret (2000), considering that the quantum efficiency of a typical unfiltered CCD peaks somewhere between these bands.

Residual trends in a few archival light curves were removed by subtracting a low-order polynomial fitted over the off-transit part. Where photometric uncertainties are not given in the raw data, the off-transit RMS was adopted as photometric error. Before the fitting procedure, the time coordinate of all light curves has been uniformly converted to the BJD_{TDB} (Barycentric Julian Date in Barycentric Dynamical Time) standard, as prescribed Eastman et al. (2010). This step is crucial if one is seeking for a TTV signal because a comparison between data with different time standards can result in a spurious modulation in the $O-C$ diagram.

The resulting best-fit models are plotted in Fig. 22 for both WASP-1b (left panels) and HAT-P-20b (right panels). In Table 10 and Table 12 we report the newly-estimated best-fit values of T_0 (BJD_{TDB}) for each transit of WASP-1b and HAT-P-20b, respectively; the other fitted parameters i, $R_p/R_\star$, $(R_p + R_\star)/a$, and u_1 are summarized on Table 13.

5.4 DATA ANALYSIS

5.4.1 *TTV analysis*

The construction of an $O-C$ diagram requires a reference ephemeris $T_0 = N \cdot P + T_{ref}$, where T_0 is the predicted transit time at epoch N and T_{ref} an arbitrary "zero" ($N = 0$) epoch.

5.4.1.1 *WASP-1b*

Employing all the T_0 values tabulated in Table 10, we calculated a new linear ephemeris for WASP-1b by weighted ordinary least squares, setting the new zero point T_{ref} at `WT1`, being the most recent and precise transit. A first $O-C$ diagram clearly revealed that the first data point (`WC1`) is a $3.6\,\sigma$ outlier. This could be ascribed to the high level of correlated ("red") noise light curve (Fig. 22), therefore `WC1` was subsequently excluded from our analysis.

After the `WC1` rejection, the re-estimated reference ephemeris for WASP-1b is

$$\begin{aligned} T_0\,(BJD_{TDB}) = (2455530.31970 \pm 0.00016) + \\ + N(2.5199448 \pm 0.0000005) \end{aligned} \tag{19}$$

where the uncertainties on P and T_{ref} were obtained from the covariance matrix of the fit, rescaled by the square root of the reduced χ^2 to take into account the real dispersion of our data. The corresponding $O-C$ data is plotted in the upper panel of Fig. 23. It is noteworthy that $\chi^2_r \simeq 1.09$ for our fit (RMS = 118 s), indicating that error bars

Table 9: Summary of the light curves of WASP-1b analyzed in this work.

N	ID	date	telescope	filter	N_p	τ (s)	σ (mmag)	σ_{120} (mmag)	reference paper	notes
0	WT1	2010/11/29	Asiago-1.82m	R	2640	7.4	2.745	0.684	This work	–
−642	WC1	2006/10/02	KO-0.35m	R	410	74.5	4.321	3.405	Collier Cameron et al. (2007)	low S/N
−605	WH1	2006/09/27	FLWO-1.2m	Sloan z	657	42.0	1.742	1.031	Charbonneau et al. (2007)	–
−602	WS1	2006/10/04	Wise-1.0m	I	270	83.5	1.816	1.515	Shporer et al. (2007)	–
−600	WS2	2006/10/09	Wise-1.0m	I	313	74.9	2.416	1.908	Shporer et al. (2007)	partial
−305	WD1	2008/10/22	KPNO-2.1m	J	636	44.8	2.523	1.541	Sada et al. (2012)	–
−596	WA1	2006/10/19	Finland-0.30m	R	217	120.2	2.934	2.937	AXA obs. Hentunen	–
−453	WA2	2007/10/15	Arizona-0.36m	R	388	70.1	3.412	2.608	AXA obs. Gary	–
−315	WE1	2008/09/26	T1T-1.20m	R	427	51.9	2.273	1.495	ETD obs. Olhert	–
−305	WA3	2008/10/22	Arizona-0.28m	clear	372	71.8	3.254	2.517	AXA obs. Gary	–
−38	WE2	2010/08/25	Calar Alto-1.23m	R	183	118.6	1.053	1.047	ETD obs. Hormuth	–

The columns give: the transit epoch N assuming $T = T_0 + NP$ and the original ephemeris from Collier Cameron et al. (2007), the ID code, the "evening date" of the observation, the filter employed, the number N_p of unbinned data points, the average net cadence τ in seconds, the photometric scatter σ measured as the 68.27^{th} percentile of the residuals from the best-fit model, the normalized photometric scatter $\sigma_{120} = \sigma\sqrt{\tau/120^s}$, the reference paper or database, and comments.

Table 10: Central instants of WASP-1b transits estimated from all the individual light curves.

N	T_0 (mean) BJD_{TDB}	T_0 (med) BJD_{TDB}	Σ	$O-C$ (d)	$\frac{O-C}{\sigma}$	ID	telescope
−642	$2454010.78632 \pm 0.00175$	$2454010.78621^{+0.00186}_{-0.00164}$	1.13	−0.00571	−3.59	WC1	KO-0.35m
−605	$2454005.75274 \pm 0.00038$	$2454005.75269^{+0.00051}_{-0.00026}$	1.95	−0.00036	−0.95	WH1	FLWO-1.2m
−602	$2454013.31335 \pm 0.00045$	$2454013.31332^{+0.00050}_{-0.00040}$	1.25	0.00041	0.91	WS1	Wise-1.0m
−600	$2454018.34984 \pm 0.00282$	$2454018.34975^{+0.00303}_{-0.00261}$	1.16	−0.00299	−1.06	WS2	Wise-1.0m
−596	$2454028.43403 \pm 0.00179$	$2454028.43448^{+0.00227}_{-0.00133}$	1.71	0.00143	0.80	WA1	Finland-0.30m
−453	$2454388.78506 \pm 0.00089$	$2454388.78508^{+0.00096}_{-0.00081}$	1.18	0.00035	0.40	WA2	Arizona-0.36m
−315	$2454736.53888 \pm 0.00182$	$2454736.53887^{+0.00186}_{-0.00178}$	1.05	0.00179	0.98	WE1	T1T-1.20m
−305	$2454761.73594 \pm 0.00066$	$2454761.73598^{+0.00061}_{-0.00071}$	1.17	−0.00060	−0.91	WD1	KPNO-2.1m
−305	$2454761.73804 \pm 0.00102$	$2454761.73793^{+0.00100}_{-0.00103}$	1.03	0.00150	1.48	WA3	Arizona-0.28m
−38	$2455434.56159 \pm 0.00024$	$2455434.56162^{+0.00017}_{-0.00030}$	1.75	−0.00021	−0.88	WE2	Calar Alto-1.23m
0	$2455530.31981 \pm 0.00019$	$2455530.31983^{+0.00016}_{-0.00022}$	1.38	0.00011	0.58	WT1	Asiago-1.82m

The columns give: the transit epoch N assuming $T = T_0 + NP$ and the new ephemeris Eq. 19, the best-fit value for the central instant T_0 of the transit and the associated σ, the median value of the distribution of T_0 from the Residual Permutation (RP) algorithm and the associated errors σ_+ and σ_-, the "skew" parameter $\Sigma = \max\{\sigma_+, \sigma_-\}/\min\{\sigma_+, \sigma_-\}$, the $O-C$ according to Eq. 19 in days, the $O-C$ in units of σ, the ID code of the light curve, and the telescope employed.

Table 11: Summary of the light curves of HAT-P-20b analyzed in this work.

N	ID	date	telescope	filter	N_p	τ (s)	σ (mmag)	σ_{120} (mmag)	reference paper	notes
0	HT1	2011/02/05	Asiago-1.82m	R	2556	5.3	3.564	0.751	this work	–
103	HT2	2011/11/28	Asiago-1.82m	R	3108	4.3	6.291	1.194	this work	red noise?
111	HT3	2011/12/22	Asiago-1.82m	R	2411	5.3	4.302	0.903	this work	–
−242	HB1	2009/03/11	FLWO-1.2m	Sloan i	406	50.8	1.923	1.251	Bakos et al. (2011)	–
−164	HB2	2009/10/21	FLWO-1.2m	Sloan i	339	37.3	2.061	1.149	Bakos et al. (2011)	–
−8	HE1	2011/01/13	SC-0.30m	R	171	142.8	3.330	3.632	ETD obs. Naves	–
−8	HE2	2011/01/13	SC-0.35m	clear	114	138.7	1.249	1.343	ETD obs. Garcia	–
1	HE3	2011/02/08	Newton-0.25m	clear	100	128.3	2.192	2.267	ETD obs. Přibík	–
103	HE4	2012/11/29	Newton-200/1000	clear	282	68.1	3.751	2.825	ETD obs. Trnka	–
104	HE5	2011/12/01	Refractor-0.16m	cclear	196	73.5	3.304	2.586	ETD obs. Ayomamitis	–
129	HE6	2012/02/11	Newton-200/1000	clear	56	244.6	1.841	2.628	ETD obs. Trnka	–
129	HE7	2012/02/11	RC-0.25m	clear	130	96.2	2.562	2.293	ETD obs. Garcia	–
145	HE8	2012/03/28	Refractor-0.1m	clear	129	137.3	2.659	2.844	ETD obs. Carreño	–

See Table 9 for a description of the columns.

Table 12: Central instants of HAT-P-20b transits estimated from all the individual light curves.

N	T_0 (mean) BJD_{TDB}	T_0 (med) BJD_{TDB}	Σ	$O-C$ (d)	$\frac{O-C}{\sigma}$	ID	telescope
−242	$2454902.65764 \pm 0.00019$	$2454902.65761^{+0.00022}_{-0.00016}$	1.38	−0.00008	−0.40	HB1	FLWO-1.2m
−164	$2455126.93245 \pm 0.00019$	$2455126.93245^{+0.00018}_{-0.00020}$	1.11	−0.00012	−0.63	HB2	FLWO-1.2m
−8	$2455575.47974 \pm 0.00076$	$2455575.47973^{+0.00066}_{-0.00086}$	1.30	−0.00253	−3.33	HE1	SC-0.30m
−8	$2455575.48039 \pm 0.00037$	$2455575.48038^{+0.00039}_{-0.00036}$	1.08	−0.00188	−5.09	HE2	SC-0.35m
0	$2455598.48522 \pm 0.00016$	$2455598.48524^{+0.00012}_{-0.00020}$	1.67	0.00040	2.49	HT1	Asiago-1.82m
1	$2455601.35956 \pm 0.00036$	$2455601.35948^{+0.00043}_{-0.00029}$	1.48	−0.00058	−1.61	HE3	Newton-0.25m
103	$2455894.64292 \pm 0.00046$	$2455894.64292^{+0.00047}_{-0.00044}$	1.07	0.00028	0.61	HE4	Newton-0.20m
103	$2455894.64393 \pm 0.00043$	$2455894.64400^{+0.00038}_{-0.00049}$	1.29	0.00129	3.00	HT2	Asiago-1.82m
104	$2455897.51844 \pm 0.00074$	$2455897.51856^{+0.00062}_{-0.00087}$	1.40	0.00048	0.65	HE5	Refractor-0.16m
111	$2455917.64445 \pm 0.00028$	$2455917.64444^{+0.00043}_{-0.00013}$	3.31	−0.00074	−2.64	HT3	Asiago-1.82m
129	$2455969.40139 \pm 0.00061$	$2455969.40138^{+0.00062}_{-0.00061}$	1.02	0.00047	0.76	HE6	Newton-0.20m
129	$2455969.39959 \pm 0.00054$	$2455969.39959^{+0.00056}_{-0.00052}$	1.08	−0.00133	−2.47	HE7	RC-0.25m
145	$2456015.40859 \pm 0.00034$	$2456015.40857^{+0.00033}_{-0.00035}$	1.06	0.00257	7.55	HE8	Refractor-0.1m

See Table 10 for a description of the columns.

are well estimated and that residuals are in nearly perfect agreement with a random distribution ("white noise"). The newly inferred P is in perfect agreement with values published in the past, though with a much smaller associated error.

We conclude that no TTV is detectable for WASP-1b within the noise level allowed by all available data. To confirm this conclusion, we carried out a further analysis by employing the Generalised Lomb-Scargle periodogram (GLS, Zechmeister & Kürster 2009). We chose to span the period range 6-300 days, to avoid aliasing. The periodogram plot is shown in the second panel from the top of Fig. 23; harmonics of the orbital period up to $9:1$ are marked with vertical dashed lines. As expected from a white noise distribution, no strong peak of spectral power is present on the whole frequency range.

5.4.1.2 *HAT-P-20b*

The case of HAT-P-20b is more complex. We computed a new reference ephemeris in the same way described above, adopting our most accurate transit light curve (HT1) as T_{ref} ($N = 0$) and employing all the data points reported in Table 12:

$$\begin{aligned} T_0(BJD_{TDB}) = (2455598.48482 \pm 0.00032) + \\ + N\,(2.8753186 \pm 0.000002) \end{aligned} \tag{20}$$

Again, uncertainties on both quantities were rescaled by $\sqrt{\chi^2_r}$. The resulting $O-C$ diagram (third plot from the top in Fig. 23) is significantly scattered, being $\chi^2_r \simeq 13.$ for the whole data set. Even focusing the analysis only on transits observed by professional astronomers (HB1, HB1, HT1, HT2, and HT3, black and blue points of Fig. 23) the observed points are in disagreement with the linear ephemeris model ($\chi^2_r \simeq 6.7$). As discussed in Section 5.3, our HT2 transit is slightly affected by red noise and this could bias the corresponding value of T_0. Nevertheless, both HT1 and HT3 possess a negligible amount of red noise and both deviate off the model by $\sim 2.5\sigma$, in opposite directions. Two data points from amateur light curves (HE2 and HE8) deviate by even more ($\sim 5\sigma$ and $\sim 7.5\sigma$). No clear pattern among the residuals is detectable by eye.

The GLS periodogram for the whole HAT-P-20b data set (fourth panel of Fig. 23) shows several power peaks, none of them being particularly prominent. If one folds the $O-C$ diagram on the frequency with the largest spectral power (corresponding to $P \simeq 28.3$ days) the resulting χ^2_r value decreases from ~ 13 to a more acceptable value of ~ 3, suggesting that a genuine pseudo-sinusoidal TTV of semi-amplitude ~ 0.0017 days (~ 150 s) could be a possible explanation for this behaviour (Fig. 24). However, we warn that the above-mentioned peak falls on a 9:1 harmonic of the orbital period (being possibly due to aliasing) and that other peaks output similar results. This is a consequence of the fact that, with only four high-S/N measurements, our

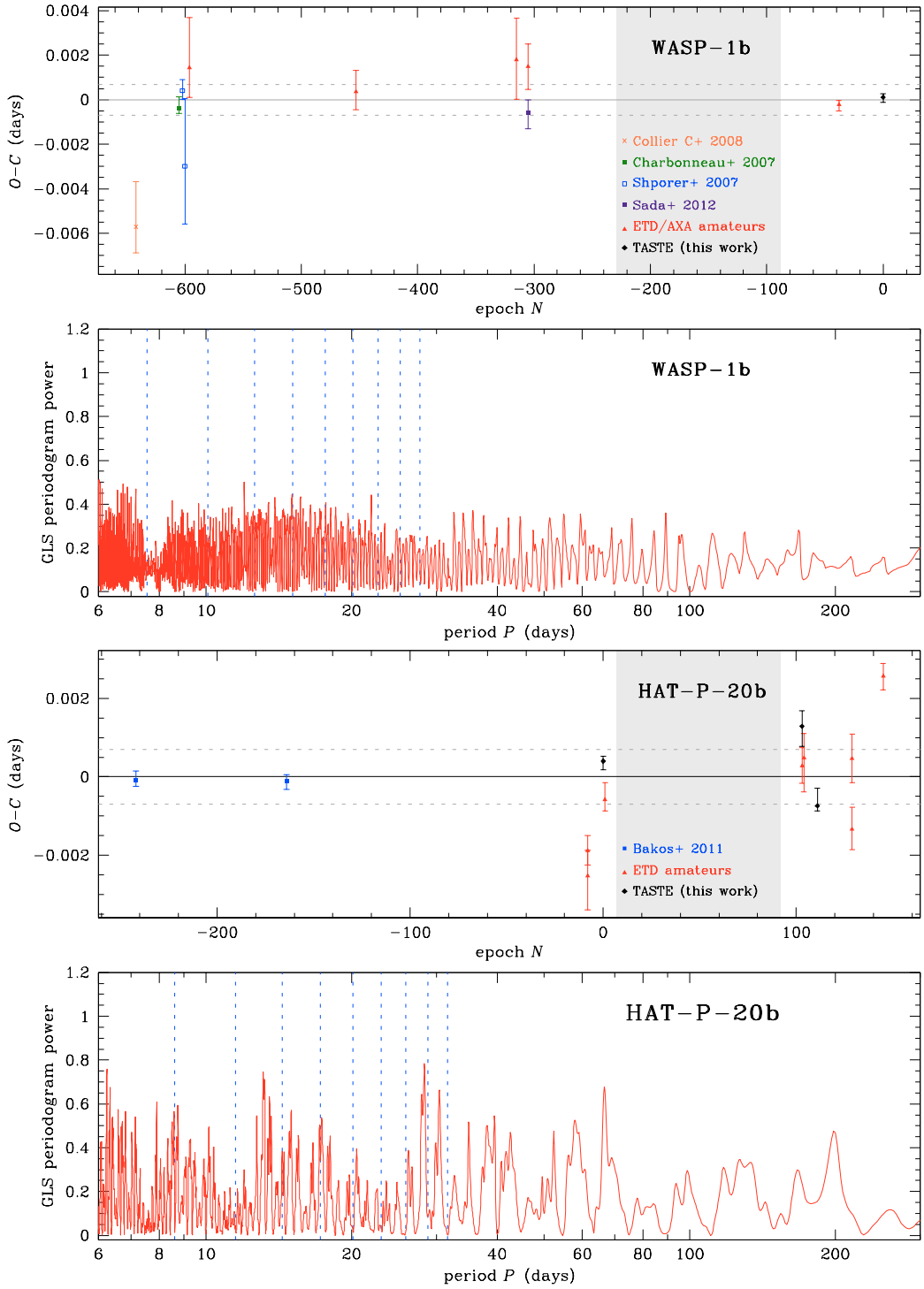

Figure 23: *First panel from the top*: O − C diagram for WASP-1b, where every estimated transit time T_0 reported in Table 10 has been compared with that predicted by the best-fit ephemeris in Eq. 19 (gray continuous line). Two dashed gray lines mark ±1 minute from the ephemeris. *Second panel from the top*: GLS periodogram for all O − C points of WASP-1b, excluding `WC1` as explained in the text. Blue dashed lines mark the first ten sub-harmonics of the orbital period. *Third and fourth panels*: same as above for HAT-P-20b, employing Eq. 20 as reference ephemeris. The GLS periodogram has been computed from all data points reported in Table 10.

Table 13: Orbital/physical parameters of WASP-1b and HAT-P-20b estimated from individual light curves.

WASP-1b

ID	telescope	filter	$(R_p + R_\star)/a$	$R_p/R_\star$	i	u_1	$u_{1,th}$
WC1	KO-0.35m	R	$0.1978^{+0.0370}_{-0.0124}$	$0.0985^{+0.0032}_{-0.0030}$	$88.96^{+0.84}_{-1.39}$	$1.143^{+0.271}_{-0.417}$	0.286
WH1	FLWO-1.2m	Sloan z	$0.1937^{+0.0066}_{-0.0024}$	$0.1040^{+0.0009}_{-0.0010}$	$88.45^{+1.18}_{-1.60}$	$0.015^{+0.115}_{-0.080}$	0.167
WS1	Wise-1.0m	I	$0.2009^{+0.0098}_{-0.0069}$	$0.1049^{+0.0020}_{-0.0021}$	$86.77^{+1.58}_{-1.50}$	$0.025^{+0.081}_{-0.112}$	0.204
WS2	Wise-1.0m	I	$0.1854^{+0.0122}_{-0.0076}$	$0.1043^{+0.0016}_{-0.0011}$	$88.40^{+1.25}_{-1.98}$	$0.122^{+0.097}_{-0.101}$	0.204
WD1	KPNO-2.1m	J	$0.2321^{+0.0243}_{-0.0259}$	$0.1069^{+0.0014}_{-0.0013}$	$83.36^{+3.03}_{-2.13}$	0.076 (fixed)	0.076
WT1	Asiago-1.82m	R	$0.1922^{+0.0016}_{-0.0011}$	$0.1030^{+0.0007}_{-0.0006}$	$89.51^{+0.40}_{-0.79}$	$0.318^{+0.040}_{-0.034}$	0.286
WE2	Calar Alto-1.23m	R	$0.1953^{+0.0016}_{-0.0015}$	$0.1029^{+0.0003}_{-0.0003}$	$89.46^{+0.40}_{-1.03}$	0.323 (fixed)	0.323
w. mean			$0.1936^{+0.0032}_{-0.0032}$	$0.1032^{+0.0013}_{-0.0013}$	$89.00^{+1.00}_{-1.26}$		

The columns give: the ID code of the light curve, the telescope and the filter employed, the fitted sum of the fractional radii $R_p/a + R_\star/a$, the fitted ratio of the fractional radii $R_p/R_\star$, the fitted inclination i, the adopted linear limb darkening (LD) coefficient u_1, and the theoretical linear LD coefficient $u_{1,th}$ interpolated from the Claret (2000, 2004) tables. The quoted error bars are derived from the JKTEBOP RP algorithm. For WE2, HE2 and HE3 we fixed u_1 coefficient to its theoretical value otherwise RP algorithm gives us a non-physical solution. For both planets, the last row of each sub-table shows the weighted means of all the individual estimates.

Table 14: Orbital/physical parameters of WASP-1b and HAT-P-20b estimated from individual light curves.

HAT-P-20b

ID	telescope	filter	$(R_p + R_\star)/a$	$R_p/R_\star$	i	u_1	$u_{1,th}$
HB1	FLWO-1.2m	Sloan i	$0.0949^{+0.0055}_{-0.0054}$	$0.1256^{+0.0020}_{-0.0044}$	$87.33^{+0.64}_{-0.46}$	$0.520^{+0.095}_{-0.098}$	0.470
HB2	FLWO-1.2m	Sloan i	$0.1023^{+0.0057}_{-0.0054}$	$0.1287^{+0.0023}_{-0.0032}$	$86.67^{+0.50}_{-0.52}$	$0.419^{+0.170}_{-0.178}$	0.470
HT1	Asiago-1.82m	R	$0.1074^{+0.0055}_{-0.0064}$	$0.1441^{+0.0035}_{-0.0058}$	$86.46^{+0.62}_{-0.46}$	$0.663^{+0.131}_{-0.134}$	0.595
HT3	Asiago-1.82m	R	$0.1105^{+0.0052}_{-0.0051}$	$0.1456^{+0.0028}_{-0.0041}$	$86.12^{+0.47}_{-0.49}$	$0.561^{+0.115}_{-0.215}$	0.595
HE2	SC-0.35m	clear	$0.1079^{+0.0041}_{-0.0048}$	$0.1377^{+0.0017}_{-0.0020}$	$86.37^{+0.39}_{-0.27}$	0.449 (fixed)	0.449
HE3	Newton-0.25m	clear	$0.1271^{+0.0082}_{-0.0063}$	$0.1484^{+0.0037}_{-0.0023}$	$85.29^{+0.39}_{-0.55}$	0.449 (fixed)	0.449
w. mean			$0.1071^{+0.0091}_{-0.0091}$	$0.1374^{+0.0087}_{-0.0087}$	$86.32^{+0.62}_{-0.62}$		

The columns give: the ID code of the light curve, the telescope and the filter employed, the fitted sum of the fractional radii $R_p/a + R_\star/a$, the fitted ratio of the fractional radii $R_p/R_\star$, the fitted inclination i, the adopted linear limb darkening (LD) coefficient u_1, and the theoretical linear LD coefficient $u_{1,th}$ interpolated from the Claret (2000, 2004) tables. The quoted error bars are derived from the JKTEBOP RP algorithm. For WE2, HE2 and HE3 we fixed u_1 coefficient to its theoretical value otherwise RP algorithm gives us a non-physical solution. For both planets, the last row of each sub-table shows the weighted means of all the individual estimates.

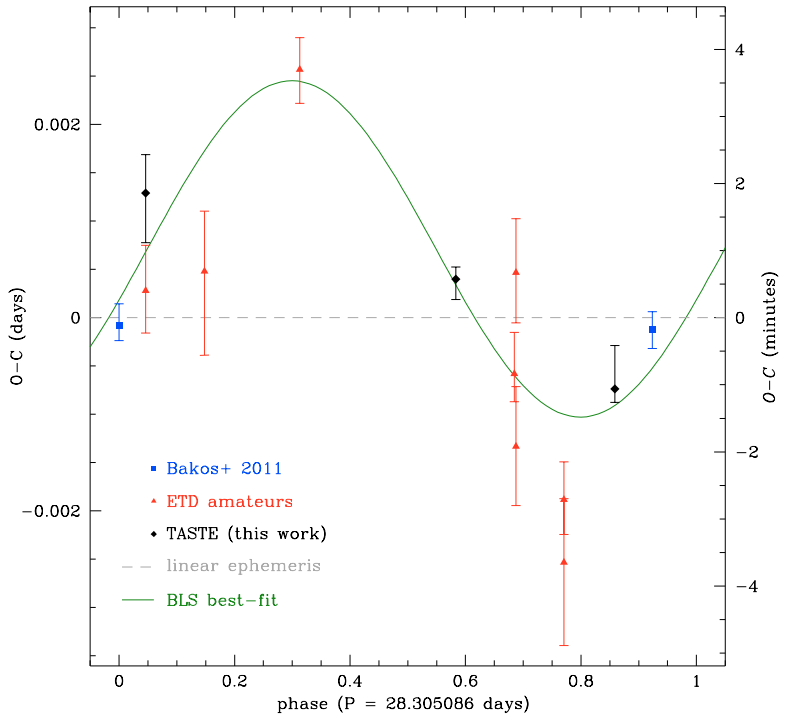

Figure 24: O − C diagram for HAT-P-20b folded over the best-fit period P = 28.305086 days corresponding to the highest peak found in the GLS periodogram. The green line is the GLS best-fit sinusoidal model, while the gray dashed line is the reference ephemeris in Eq. 20.

analysis is still based on small-sample statistics. Our TTV detection is thus only suggestive, deserving further follow-up observations for a confirmation.

5.4.2 *Orbital and physical parameters*

Along with T_0, `JKTEBOP` was allowed to fit for both planets all those orbital and physical parameters which can be derived from a transit light curve: i, $R_p/R_\star$, $(R_p + R_\star)/a$ and, for high-S/N transits, the linear limb darkening coefficient u_1. All the individual fitted values are summarized on Table 13, along with the non-symmetric uncertainties estimated by the residual-permutation technique. Most values are in agreement within their error bars with each other, with the exception of `WC1` for WASP-1b and `HB1`, `HB2` for the fractional ratio of HAT-P-20b. We thus did not employed these transits in the subsequent analysis. We evaluated as final best-fit values the weighted means of i, $(R_p + R_\star)/a$ and $R_p/R_\star$ (last row of each sub-table of Table 13): for this last quantity we counted only `HT1`, `HT3` and `HE3`. The image subtraction tool employed by Bakos et al. (2011) probably underesti-

mates the flux coming from the stellar companion therefore the host star turns out to be larger and the corresponding light curves is less deep. For the same reason, the linear LD coefficient is smaller both in `HB1` and `HB2`. As linear limb darkening coefficient u_1 is dependent on wavelength, no average of this quantity was calculated.

Our resulting parameters agree with the other previous estimate and, in particular, with the performed means. Moreover, our uncertainties are among the smallest ever published.

5.5 CONCLUSIONS

In this paper, we presented new light curves of the hot Jupiters WASP-1b and HAT-P-20b (not included in the original TASTE sample), and carried out a homogeneous (re-)analysis of both new data and other archival light curves from professional astronomers and from amateurs.

We gave new, more accurate estimate of the physical and orbital parameters of both planets, and carried out a TTV analysis to search for variations in the transit periodicity which could be ascribed to unknown perturbers. While the orbital period of WASP-1b is constant within the estimated uncertainties (120 s), the $O-C$ diagram of HAT-P-20b shows an anomalous amount of scatter (Fig. 24) which could be ascribed to a periodical TTV signal. We stress out that this detection is based on a few observational points a thus could be biased by small-sample statistics. New photometric observations are needed to confirm or disprove this statement and for this reason HAT-P-20b is now included in the primary TASTE sample for further analysis.

Acknowledgements

This work was partially supported by PRIN INAF 2008 "Environmental effects in the formation and evolution of extrasolar planetary system". V. G. acknowledges support from PRIN INAF 2010 "Planetary system at young ages and the interactions with their active host stars". V. N. and G. P. acknowledge partial support by the Università di Padova through the "progetto di Ateneo #CPDA103591". We thank A. Ayomamitis, A. Carreño, R. Garcia, F. Hormuth, R. Naves, J. Olhert, V. Přibík, J. Trnka (TRESCA) for their light curves published on ETD database and B. Gary and V. Hentunen for their data available on NASA Exoplanets Archive. Some tasks of our data analysis have been carried out with the VARTOOLS (Hartman et al. 2008) and `Astrometry.net` codes (Lang et al. 2010).

6

A SEARCH FOR PLANETS IN NGC 6397

Searches for planetary transits carried out in open and globular clusters have to date yielded only a handful of weak, unconfirmed candidates. These results have been interpreted as either being insignificant, or evidence that the cluster chemical or dynamical environment inhibits planetary formation or survival. Most campaigns have been limited by small sample statistics or systematics from ground-based photometry. In this chapter I will present a search for transiting planets and variables in a deep stellar field of NGC 6397 imaged by HST-ACS over 126 orbits. We analyzed 5,078 light curves, including a careful selection of 2,215 cluster-member M0–M9 dwarfs. The light curves were corrected for systematic trends and inspected using several tools. No high-significance planetary candidate is detected. We compared this null detection with the most recent results from Kepler, showing that no conclusive evidence of lower planet incidence can be drawn. However, a very small photometric jitter is measured for early-M cluster members ($\lesssim$ 2 mmag on 98% of them), which may be worth targeting in the near future with more optimized campaigns. Twelve variable stars are reported for the first time.

This chapter is based on: V. Nascimbeni, L. R. Bedin, G. Piotto, F. De Marchi, R. M. Rich (2012) *An HST search for planets in the lower Main Sequence of the globular cluster NGC 6397*, A&A, 541, A144.

6.1 INTRODUCTION

More than seven-hundred extrasolar planets are known (`exoplanet.eu` database). Most of them are characterized only through radial velocities (RV) and lack any information about their "real" mass M_p, because only $M_p \sin i$ can be measured, where i is the inclination of the orbit with respect to the line of sight. Their size is also unknown, which prevents us from getting any clues about their density and physical composition. Exoplanetary transits are highly complementary to RV techniques, providing the planetary radius R_p from the stellar radius $R_\star$ in a direct geometrical way (Seager 2011b, p. 55). Photometric searches for transits can also go much deeper than RVs in magnitude, and can monitor thousands of stars simultaneously. The Kepler mission (Borucki et al. 2010), for instance, has demonstrated the power of this technique by discovering many planetary systems with unexpected properties. Hundreds of Kepler "candidate planets", for which confirmation and mass measurement via RVs re-

mains infeasible, are still very useful for statistical purposes (Howard et al. 2011; Schlaufman & Laughlin 2011)

Star clusters, and in particular globular clusters (GC), offer a unique opportunity to study how the chemical and dynamical environments affect planetary formation and evolution. They are also comprised of stars that share (in most cases) the same age and chemistry, and whose radii $R_\star$ and masses $M_\star$ are reliably known on their main sequence (MS). Open clusters (OC) have been targeted for extensive transit searches (Mochejska et al. 2005; Montalto et al. 2007, 2011; Hartman et al. 2009, most notably) but only a handful of weak, unconfirmed candidates have been so far detected (Mochejska et al. 2006; Montalto et al. 2011). A global reanalysis suggests that the overall statistical significance of these campaigns is so low that it could be compatible with the planet host incidence observed in the field (van Saders & Gaudi 2011). On the other hand, GCs are on average much richer in stars than OCs, providing a much higher statistical significance in the case of a null detection. The only GCs monitored for transits have been 47 Tucanae for both 8 days with HST WFPC2 (Gilliland et al. 2000) and 33 days from the ground (Weldrake et al. 2005); and ω Centauri with a 25-day ground-based campaign (Weldrake et al. 2008). No planetary detection has been claimed, and Gilliland et al. (2000) concluded that the planetary occurrence in 47 Tuc is smaller by a factor of ten than in field stars. The reasons that have mostly been hypothesized to explain the lack of giant planets in GCs are their metallicity and their dynamical environment.

It has long been known that metallicity is a strong primary parameter that correlates with the fraction of stars with planets Φ_p. For giant planets, Fischer & Valenti (2005), among others, measured an increase from the typical value $\Phi_p^\odot \sim 0.03$ for stars with solar metallicity up to $\Phi_p \sim 0.25$ for very metal-rich ([Fe/H] $\gtrsim +0.3$) stars. For moderately metal-poor stars ($-0.5 \lesssim$ [Fe/H] $\lesssim 0$), it is still disputed whether this correlation becomes flat at values $\Phi_p \simeq \Phi_p^\odot$ (Udry & Santos 2007; Santos et al. 2011) or Φ_p continues to decrease exponentially towards lower metallicities (Johnson et al. 2010). As more and more low-mass planets ($M_p \lesssim 30 M_\oplus$) are being discovered, it becomes clear that their Φ_p is much larger than that of giant planets (Lovis et al. 2009; Wittenmyer et al. 2011), probably around ~20–30 %. The occurrence of low-mass planets seems to be insensitive to the host star metallicity (Udry et al. 2006), except maybe for very late-type stars (Johnson & Apps 2009; Schlaufman & Laughlin 2011) but the M-dwarf metallicity calibration is still too uncertain to draw conclusions.

The complex dynamical environment of a cluster is the second major concern about the survival of protoplanetary systems. Theoretical studies give different answers, but some of them imply that gravitational stripping processes are not strong enough to disrupt very short-period ($P < 5$ days) planetary systems, even in the densest regions

of a typical GC (Fregeau et al. 2006; Spurzem et al. 2009). Planets do indeed exist in clusters. Giant planets have been detected around evolved stars belonging to open clusters (Lovis & Mayor 2007; Sato et al. 2007), and around a pulsar in the globular cluster M4 (Thorsett et al. 1999). It is therefore difficult to understand why no planets have been detected in 47 Tuc. The search by Gilliland et al. (2000) was sensitive only to giant planets ($R_p \gtrsim 1 R_{jup}$) around stars in the upper MS, excluding late-K and M dwarfs. More data are needed to sample other regions of the parameter space.

On the other hand, it is convenient to search for transits around KM main-sequence stars because of their larger expected signal. These targets, even in the nearest GCs, are faint ($V > 18$) and extremely crowded. Space-based observations are necessary to achieve the needed signal-to-noise ratio (S/N) per time unit, and to minimize the number of false positives caused by blended photometric contaminants. The wide-field imagers mounted on HST (ACS and WFC3) are unrivalled in this respect, and their large archive of deep photometric series of GCs is already available to be exploited for transit searches. However, we show in Sec. 6.3 that HST time-resolved photometry is influenced by many sources of systematic errors that require a careful correction. We developed specific tools to this purpose and applied them to a test case. Other data sets (such as those for 47 Tuc) will be investigated in the near future, to test whether a more optimized campaign is worth pursuing.

In this paper, we present a search for variables and planetary transits in NGC 6397, exploiting a 126-orbit data set from the HST Advanced Camera for Surveys (ACS; GO-10424; PI:Richer). NGC 6397 is a metal-poor ($[Fe/H] \simeq -2$) core-collapsed globular cluster, and the second-closest known (Gratton et al. 2003; Richer et al. 2008). Our work is in some sense complementary to that presented by Stello & Gilliland (2009), who employed the same data set to study the microvariability of highly saturated red giants. Though these data were not optimized for a transit search, its unprecedented depth allowed us to search for planets on a homogeneous sample of 2,215 member M-dwarf stars down to the hydrogen-burning limit. The M dwarfs are considered the most promising targets to discover rocky planets in the near future (Scalo et al. 2007). They are the smallest stars ($R_\star \simeq 0.1$–$0.5 R_\odot$), and therefore the transit depth for a given planet is larger by a factor of ~ 4–100 that that of a solar-type host star. They are also intrinsically faint ($L_\star \simeq 0.02$–$5 \cdot 10^{-5} L_\odot$), meaning that a habitable planet would have an orbital period of only $P = 10$–30 days.

6.2 OBSERVATIONS AND DATA REDUCTION

Our analysis is based on the HST data set GO-10424 (PI: Richer), whose acquisition was originally made to probe the bottom of the

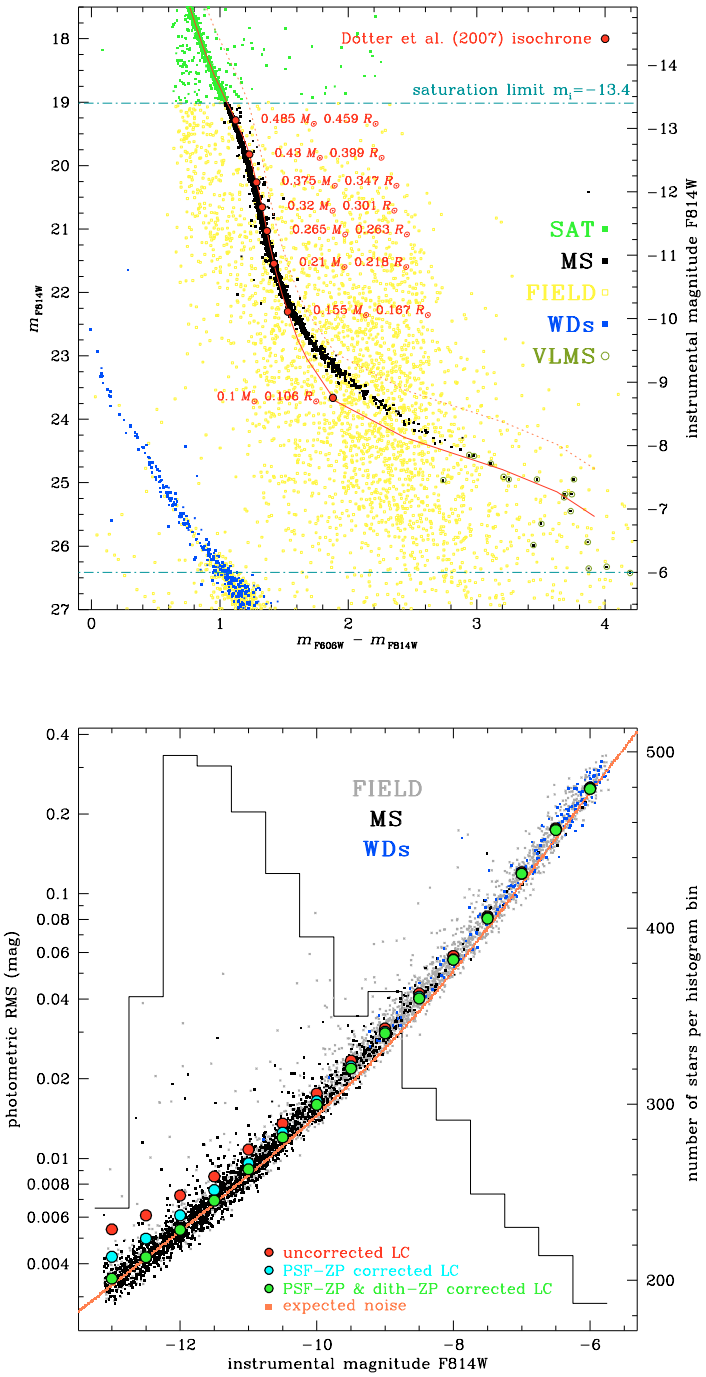

Figure 25: *Upper panel.* Color-magnitude diagram ($m_{F606W} - m_{F814W}, m_{F814W}$) for all the stars in the Anderson et al. (2008) master list; the 5,078 sources selected in this work lie between the saturation limit at $m_{F814W} \simeq 19$ and the faint limit $m_{F814W} \simeq 26.5$ (dash-dot lines). The red line is the isochrone by Dotter et al. (2007) employed in Richer et al. (2008). The dotted line marks the loci occupied by equal-mass MS-MS binaries. *Lower panel.* The RMS for light curves in our sample as a function of the instrumental magnitude. Red circles: median RMS averaged over 0.5 mag bins, without any correction. Cyan circles: the same, after PSF-ZP correction. Green circles: both PSF-ZP and dither-ZP corrections applied. Small points are the RMS of the individual light curves after both corrections. The solid orange line is the expected theoretical noise level. The superimposed histogram represents the number of targets in each 0.5 mag bin (scale at the right).

MS and the end of the white dwarf (WD) cooling sequence in NGC 6397 (Hansen et al. 2007; Richer et al. 2008). A single $202'' \times 202''$ field, located $5'$ from the cluster core was imaged for 126 orbits with the wide-field channel of the ACS. In each orbit, a single exposure through the F606W filter was preceded and succeeded by two F814W images, with exposure times ranging between 584 s and 804 s (median: 704 s). Overall, 252 F814W frames and 126 F606W frames were secured, for a total exposure time of $\sim$ 50 hours. Shorter exposures ($t_{exp} = 1, 5, 40$ s) were also taken to measure the fluxes of the brightest stars, but they were not used in our study.

The dynamic range of the "deep" exposures is perfect for our purposes, as the observed luminosity function (LF) of the cluster MS members peaks at $m_{F814W} \simeq 21$ (that is, on well-measured stars with S/N $\sim$ 200 in the same filter; Fig. 25, histogram on the right panel). Saturation occurs around MoV spectral type at $m_{F814W} \simeq 18.7$ and the faintest cluster members (M9V) are found at $m_{F814W} \simeq 24$ (S/N $\sim$ 20), such that a sample of $\sim 2,000$ cluster M dwarfs down to the hydrogen-burning limit is available to transit search (Fig. 25, left panel).

On the other hand, these data were not optimized to search for transit events, thus two aspects of the observing setup are somewhat restrictive. First, the time coverage of the frames is discontinuous, unlike in Gilliland et al. (2000). The data for $\sim$ 50 h of integration time were spread among twenty-one non-contiguous days, spanning a twenty-eight day period. This translated into a much lower completeness for our search, especially for the longest periods ($P > 3$ d, see Sec. 6.5). The second reason is that each pointing was shifted within a ten-position dithering pattern $\Delta x, \Delta y$ plus a subpixel offset $\delta x, \delta y$. While dithering is usually suitable for undersampled images (Anderson & King 2000), it prevented us from reaching the highest photometric accuracy possible for the brightest stars. For these targets, the amount of random noise is so low that the unavoidable flat-field and pixel-to-pixel residual errors are no longer negligible. A zero-point correction, discussed in the next Section, was developed to suppress these systematic errors.

We carried out the data reduction on individual bias-corrected and flat-fielded `.flt` images provided by the HST pipeline. We employed the master input list from Anderson et al. (2008), and the code described by Anderson & King (2006) based upon the effective PSF (ePSF) approach first developed by Anderson & King (2000). Four tests were performed on a subset of twenty F814W frames taken at the same integer-pixel dithering position, to choose the best reduction strategy among:

1. Allowing spatially-constant perturbed ePSFs as described by Anderson & King (2006);

2. Correcting the raw frames for charge transfer (in)efficiency (CTE) with the pixel-based algorithm proposed by Anderson & Bedin (2010);

3. Using both the 1) and 2) corrections;

4. Using neither.

For all the measured sources, the root mean square (RMS) values of their light curve as a function of magnitude were compared. Methods 1-3 above provided no detectable improvement over the fourth choice, therefore we decided not to apply any CTE or PSF correction at this stage. Actual PSFs are both spatially and temporally variable, and require a frame-to-frame *a posteriori* correction that is explained in Section 6.3.

Hereafter, we focus our analysis on only F814W frames for many reasons. They are much deeper than F606W images for faint, red, low MS stars, and less affected by PSF short-term variations as shown for this very same dataset by Anderson & King (2006). The sky background is also much lower in F814W exposures. The way in which the F814W frames were sampled (at the beginning and the end of each 96-minute orbit) ensures that the F606W frames are nearly useless for increasing the transit detection efficiency. In this way, we also avoided the need to correct for any tricky registration of the light curves between the two filters.

Sources beyond the saturation limit of the longest exposures ($m_{F814W} \lesssim 19$) and sources detected in fewer than 200 frames ($m_{F814W} \gtrsim 26.5$) were excluded from this study, leaving 5,078 objects including cluster members, field stars, and a limited number of non-stellar objects. We evaluated the membership of each entry by performing a selection on the proper motions between our epoch and the archival ACS GO-11633 data set (PI: Rich), centered on the same field. We flagged 2,430 sources as cluster members, of which 215 belong to the white dwarf (WD) sequence (see the CMD on Fig. 25, left panel). The remaining 2,215 MS stars are red dwarfs ranging from MoV spectral type ($R_p \simeq 0.5 R_\odot$, $M_p \simeq 0.5 M_\odot$) down to the hydrogen-burning limit, as confirmed by superimposing an isochrone by Dotter et al. (2007) on the CMD, as done in Richer et al. (2008).

6.3 SYSTEMATIC CORRECTION

The instrumental magnitude $-2.5\log(\mathrm{DN})$ of each star was registered to the median instrumental magnitude of stars measured in the deepest frame of the F814W series. We refer to this magnitude as m. Saturation occurs at $m \lesssim -13.4$. The RMS σ_m of our full sample of 5,078 light curves was compared with the expected noise budget, as calculated by combining theoretical photon-, dark-, background- and readout noises (right panel of Fig. 25, orange line). Individual σ_m

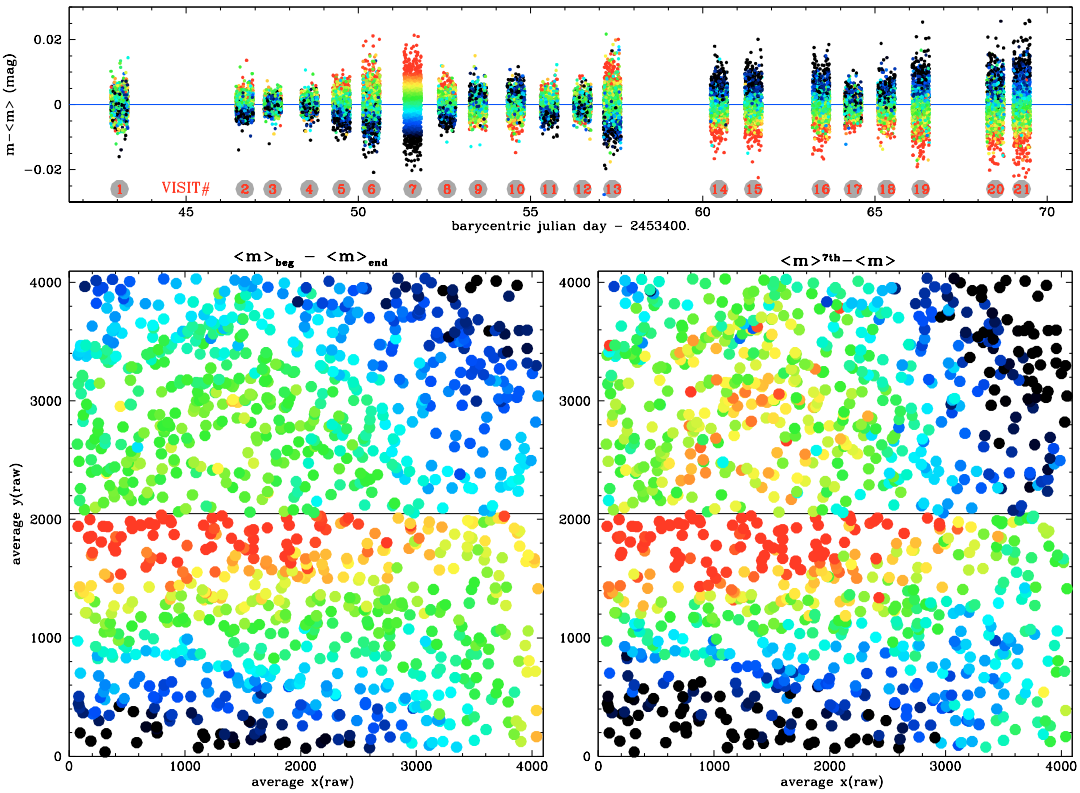

Figure 26: Mapping the PSF-ZP shift as a function of time and position on the ACS detector, with two different diagnostics (see text). The First (*left panel*) is the difference between the median magnitudes $\langle m \rangle_{beg}$ and $\langle m \rangle_{end}$ measured in frames taken respectively at the beginning and the end of the orbit, while the second (*right panel*) is the difference between the median magnitude of the star $\langle m \rangle^{7th}$ measured during the seventh "visit" of the program ($2453451 < JD < 245352$), and the median magnitude $\langle m \rangle$ of its full light curve. *Top panel:* All the high-S/N light curves ($\sigma_m < 0.02$) have been registered to their average magnitude $\langle m \rangle$. In all panels, the color scale spans the range -0.02-0.02 mag from black to red.

were averaged whitin 0.5 mag bins by applying a clipped median (red circles in the same plot) to exclude outliers from the comparison.

On the bright side, the observed noise level on average is far higher than expected, even by 50-60% for stars with $m \lesssim -12$ (red circles, right panel of Fig. 25). We identified the source of most of this excess noise as a variation in the photometric zero point (ZP) induced by systematic changes in the PSF shape. Long-term instability of the PSF was reported for ACS by Anderson & King (2006). We noticed that this ZP change (hereafter called *PSF-ZP*) follows a well-defined pattern as a function of time and average x, y position on the detector. The pattern can be mapped by evaluating for each star two diagnostic parameters that appear to be strongly correlated with the PSF-ZP shift:

1. The difference between the median magnitude $\langle m \rangle_{beg}$ measured in frames taken at the beginning of the orbit, and the median magnitude $\langle m \rangle_{end}$ measured in frames taken at the end of the orbit (left panel of Fig. 26, color-coded in the range -0.02-0.02 mag from black to red).

2. The difference between the median magnitude of the star $\langle m \rangle^{7th}$ measured in 16 consecutive frames taken during the seventh "visit" of the program ($2453451 < JD < 245352$), and the median magnitude $\langle m \rangle$ of its full light curve (right panel of Fig. 26, same scale).

The pattern is very similar in both cases. The first diagnostic $\langle m \rangle_{beg} - \langle m \rangle_{end}$ is probably a proxy of the real origin of the PSF-ZP systematic: a thermal/mechanical instability linked to the orbital phase. The dependence of PSF-ZP on time becomes evident when all the light curves with a high S/N (i.e., measured on all the 252 frames and having $\sigma_m < 0.02$) are registered to their average magnitude $\langle m \rangle$, stacked in the same plot, and color-coded as a function of $\langle m \rangle^{7th} - \langle m \rangle$ (Fig. 26, top panel, color scale from black to red in the range -0.02 to 0.02 mag). It is clear that on average stars whose flux is overestimated during the seventh visit are also systematically underestimated in the last visits (JD>2453460), and viceversa.

For a given frame and within the same chip, the PSF-ZP is a smooth function of the position on the detector. The diagnostics $\langle m \rangle^{7th} - \langle m \rangle$ and $\langle m \rangle_{beg} - \langle m \rangle_{end}$ are too noisy when evaluated for faint stars to implement an effective correction with them. We chose instead to correct the PSF-ZP with a local approach, adapted from the differential photometry algorithms described in Nascimbeni et al. (2011a). For each target star i in our sample, a set of N nearby reference stars $k = 1, \ldots, N$ was selected with the following criteria: 1) they had to lie on the same chip as the target and be within 200 pixels of it; 2) they had to be at least 20 stars whose total flux had to exceed ten times the flux of the target; and 3) they had to be detected in at least

250 frames among 252, instead of the 200-frame limit required for a target star. When requirement 2) was not met, the search radius was increased until it was met. If on a given frame j a reference star k was not detected, or when its magnitude $m_{j,k}$ was more than $3\sigma_{j,k}$ off its value averaged over the series $\langle m_{j,k} \rangle$, its magnitude was set to $\langle m_{j,k} \rangle$. A reference magnitude $m_{0,j}$ was calculated in each frame by performing the weighted mean of the magnitudes of the N reference stars $m_{0,j} = \sum_k (m_{j,k}/\sigma^2_{j,k}) / \sum_k (1/\sigma^2_{j,k})$ (Broeg et al. 2005). The target magnitude was then normalized to $m_{0,j}$. The PSF-ZP correction was applied only when it decreased the overall RMS of the target light curve. After the correction, the median RMS of the light curves (right panel of Fig. 25, cyan circles) was substantially smaller. For the brightest stars ($m \lesssim -12$), it had decreased to a level $\sim 15\%$ above the expected noise.

Most of the remaining excess noise is due to local ZP changes as well as the dithering pattern employed: an integer $\Delta x, \Delta y$ shift plus a small sub-pixel offset $\delta x, \delta y$ were added to the initial pointing x_0, y_0 (where the units are in physical pixels). We refer to this systematic effect as *dith-ZP*. To each light curve, already corrected for PSF-ZP, we applied two decorrelating algorithms where

1. The median magnitude of the star $\langle m \rangle_{\Delta x, \Delta y}$ was calculated for each subset of frames sharing the same integer-pixel dither $\Delta x, \Delta y$. The magnitude m of each frame in the subset $\Delta x, \Delta y$ was then registered to $\langle m \rangle_{\Delta x, \Delta y}$.

2. For each $\Delta x, \Delta y$ subset corrected by the previous step, we considered the magnitude m_j in each frame j as a function of the sub-pixel shift $\delta x_j, \delta y_j$. An ordinary linear least squares fitting was carried out to find the coefficients c_0, c_x, and c_y such that

$$m_j = c_0 + c_x \, \delta x_j + c_y \, \delta y_j \ . \tag{21}$$

   Once the best-fit value $m'_j = c_0 + c_x \, \delta x_j + c_y \, \delta y_j$ had been evaluated for each frame, the corrected light curves were extracted and normalized to zero by evaluating $m'_j - m_j$.

Both steps 1) and 2) were applied only when the RMS had decreased. The resulting median RMS of the PSF-ZP + dith-ZP correction is plotted in the right panel of Fig. 25 as green circles. The small black points in the same plot show the RMS of each single light curve of cluster members after our PSF-ZP and dith-ZP corrections have been applied. Their noise level approaches the theoretical limit in every magnitude bin, demonstrating that the algorithms we applied were effective.

6.4.1 *Search for transit-like events*

We searched for transits in the full set of 5,078 light curves (that is, including field stars) by applying the box-fitting least-square algorithm (BLS, Kovács et al. 2002). For each curve, BLS was applied to search for periodic dips of duration Δ and depth δ with 10,000 trial periods between 0.2 and 14 days. The relative transit duration $q = \Delta/P$ was constrained to the values possible for planetary transits around low-MS stars ($R_\star = 0.08$–$1.4 R_\odot$).

For each star, three detection diagnostics were calculated: the signal residue (SR), the signal detection efficiency (SDE) associated with the maximum peak in the BLS periodogram (Kovács et al. 2002), and the detection S/N defined as

$$S/N_{BLS} = \frac{\delta}{\sigma} \cdot \sqrt{n_t} \ , \tag{22}$$

where σ is the (unbinned) photometric noise and n_t the number of data points sampled during transits.

Other more sophisticated detection diagnostics, such as the "signal-to-pink" S/N (Pont et al. 2006; Hartman et al. 2008), are robust if correlated noise σ_{red} ("red noise", Pont et al. 2006) is present. However, they require knowledge of σ_{red} on timescales close to Δ. This is difficult to evaluate in our data, as transits are expected to be undersampled by the observing cadence. Transits of a $P \sim 3$ d planet around a M4V star are expected to last $R_\star P/(\pi a) \sim 60$ min at most, and only $\sim$ 30-40 min for later types, while images are sampled every 32-64 min. However, the amount of red noise here is very low, as demonstrated by the similarity of the measured RMS to the theoretical one. Therefore, we decided to employ both S/N_{BLS} and SDE as detection diagnostics.

To set a reliable detection criterium, 2,215 light curves were simulated, that had the same sampling times t_i and noise level as the real M-dwarfs. A synthetic transit (following the analytical model of Mandel & Agol 2002) of a 1 R_{jup} planet was injected into each curve, with a random uniform distribution in P and $\sin i$ where P was bounded to the range 1–5 d, while $\sin i$ was constrained to allow transits. The process was iterated 200 times for a total of 450,000 injections. We then tried to recover the transits with BLS, by setting the same parameters used for the real search. A planet was defined as "recovered" if at least two transits had been sampled, and if the estimated orbital period (or a low-order harmonics: 2:1, 3:1, 3:2) matched the injected one. The distributions of the "injected" and "recovered" transits in the SDE vs. S/N_{BLS} plane are plotted as black and red points in the upper left panel of Fig. 27. By dividing the parameter space into cells and evaluating the fraction of "recovered" over "injected" transits

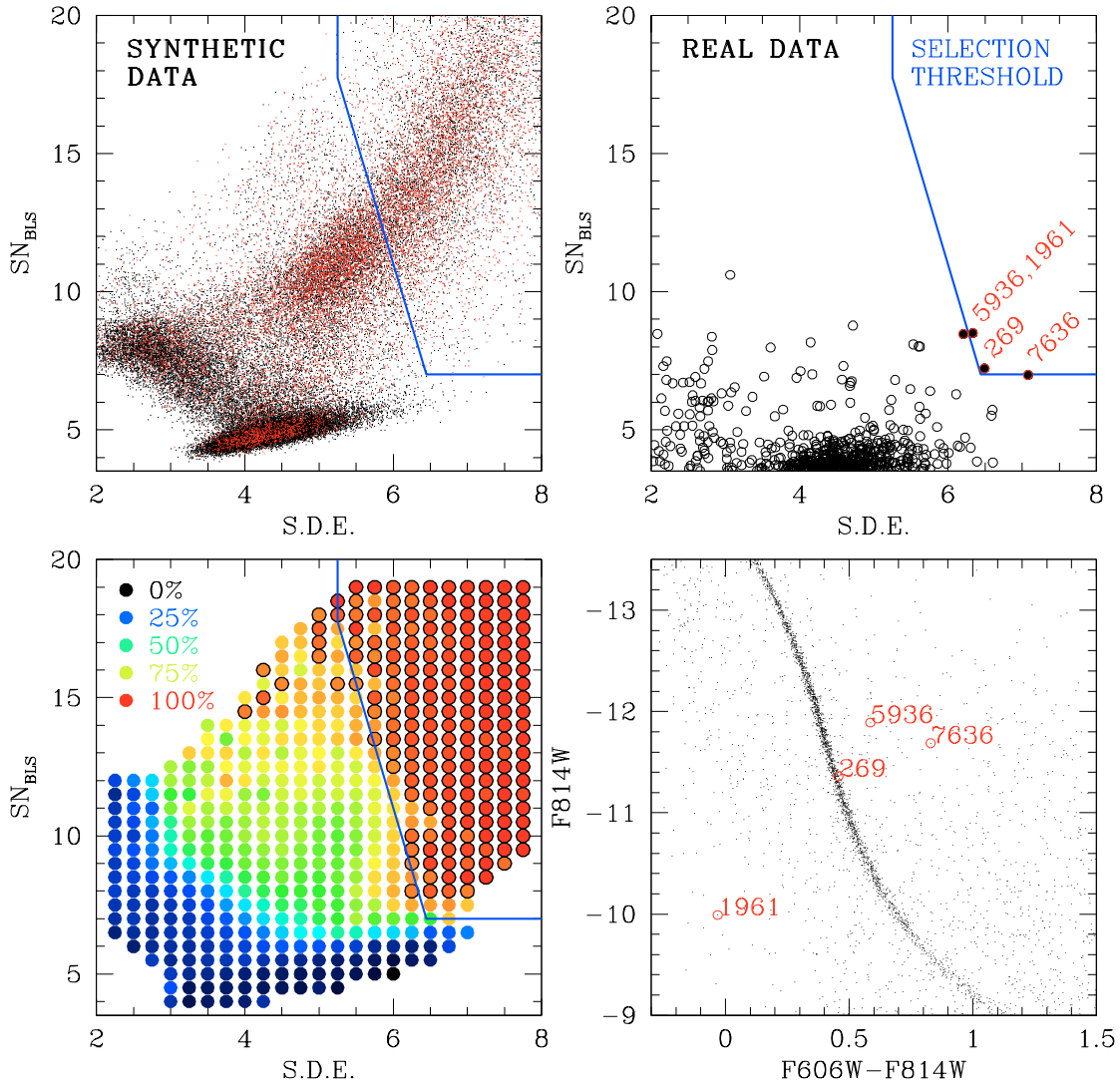

Figure 27: *Upper left:* distribution of SDE and SN_{BLS} from the BLS analysis of 450,000 artificially injected transits in synthetic light curves. "Recovered" transits are plotted as red dots (see text). *Lower left:* same as above, where the parameter space has been divided into cells and color-coded as a function of the fraction f of transits successfully recovered. Cells with $f > 90\%$ (that is, with an incidence of false positives smaller than 10%) are highlighted with a black border. The blue line correponds to the threshold defined in Eq. (23). *Upper right:* distribution of SDE and SN_{BLS} from the BLS analysis of the full sample of 5,078 real light curves. Four low-significance candidates are labeled. *Lower right:* location of the four low-significance candidates on the CMD.

(Fig. 27, lower left panel), we obtained an estimate of the expected fraction f of real transits successfully detected ("true positives"). We defined detection criteria that guarantee a fraction of false positives that is smaller than 10% (that is, $f \geqslant 90\%$) where

$$\begin{cases} SDE \geqslant 5.25 \\ S/N_{BLS} \geqslant 65 - 9 \cdot SDE \\ S/N_{BLS} \geqslant 7 \end{cases} \tag{23}$$

as indicated by the blue line in Fig. 27. With this choice, the fraction of false negatives (that is, real planets discarded by selection criteria) is about 55%, and gets larger for planets smaller than Jupiter. This is unavoidable if one wishes to keep the fraction of false positives as low as possible.

The position of all the real sources in the (SDE, SN_{BLS}) plane is shown in the upper-right panel of Fig. 27. Only four stars among the full sample meet the criteria set in Eq. (23) or get very close to the threshold. These "borderline" targets (ID#0269, 1961, 5936, and 7637) were inspected and cross-checked individually.

ID#269 light curve is crippled by a CCD bad pixel falling just under the star in one of the dithering positions.

ID#1961 is contaminated by brighter surrounding stars, and its flux drops off significantly in one fourth of the images. The BLS signal is probably spurious.

ID#5936 seems accurately measured by the reduction pipeline, though it lies extremely close to a saturated star. Its light curve should be treated with caution. The parameters of the detected signal ($P \sim 2.1$ d, $\delta = 0.08$ mag, $q = 0.025$) would be compatible with a $\sim 1\ R_{jup}$ transiting body with zero impact parameter, or with a grazing eclipsing binary. We classified ID#5936 as a cluster M-dwarf member by analyzing its proper motion (with $M_\star = 0.34 M_\odot$, $R_\star = 0.32 R_\odot$ from its color), though its position in the CMD diagram is offset from the MS by 1.4 mag in m_{F814W} and 0.2 mag in color (Fig 27, lower right panel). This cannot be due to binarity alone, and maybe the presence of a bright contaminant or the departure from the normal evolution of the companion play a role. There is also a non-negligible probability that ID#5936 is a field star having a proper motion compatible with the common motion of the cluster. It it worth noting that at least one data point with a similar decrease in brightness (0.08 mag, that is $\sim 4\sigma$) fell outside the expected transit windows fitted by BLS, and that the estimated duration ($\Delta = 76$ min) is way larger than expected. We do not consider ID#5936 to be a convincing planetary candidate. Its coordinates are listed in Table 15 for possible further studies.

ID#7636 was rejected because it fell over a bad column on frames corresponding to "transits".

In summary, we did not detect transits in our light curves, at least with an acceptable degree of statistical significance. We discuss the significance of this null detection in Section 6.5.

6.4.2 *Search for variable stars*

We performed a search for variable stars in our full database of 5,078 light curves corrected for systematic errors. First, the coefficient of spectral correlation (Ferraz-Mello 1981) was calculated for each light curve. Following the method described in de Marchi et al. (2007, 2010), we obtained a sample of 13 suspected variable stars (Table 15). All these candidates, based on their proper motions and position in the CMD, were identified as field stars with high confidence. To classify these objects, a least squares iterative sine-wave search was applied (Vaníček 1971).

Most of our candidates show a single harmonic sinusoidal shape and short periods ($P \leqslant 9$ d), namely ID#830, ID#7523, ID#2178, ID #5600, and ID#4957. Without other elements, it was impossible to derive an unambiguous classification for these variables. We suspect that these stars are most probably field BY Draconis variables, i.e. spotted and rotating KM dwarfs. This tentative classification is supported by their very red colors ($m_{F606W} - m_{F814W} = 1.27$-$2.65$).

For four stars, a good best-fit can be obtained using two harmonics. The second harmonic in the light curves of ID#3428, ID#1383, ID#4430, and ID#270 could indicate the presence of spots on the surfaces and confirm the BY Dra-type classification, while in the light curve ID#6119 the second harmonic reveals the profile of a W UMa contact eclipsing binary system. Two stars (ID#2086 and ID#258) show clearly orbit-to-orbit variability but the time coverage was too short to infer reliable values for their periods: we classified them as generic "long period variables". Finally, the fluctuations in the light curve ID#1882 are too small to allow us to confirm its nature as a variable star, hence we discarded it from our analysis. The summary classification of the entire sample is reported in Table 15, along with the best candidate transit found by BLS and discussed in Section 6.4.1.

6.5 COMPLETENESS AND SIGNIFICANCE

The significance of our null detection of transits was assessed by considering only the 2,215 cluster-member M dwarfs for which we derived reliable estimates of $R_\star$ and $M_\star$ from their position in the CMD.

For a planet of given radius R_p and orbital period P, the number of expected planet detections is given by

$$N_p = N_\star \iint \left(\Phi_p(P, R_p) \cdot \Phi_{geo} \cdot \Phi_{det} \right) \, dP \, dR_p \quad , \tag{24}$$

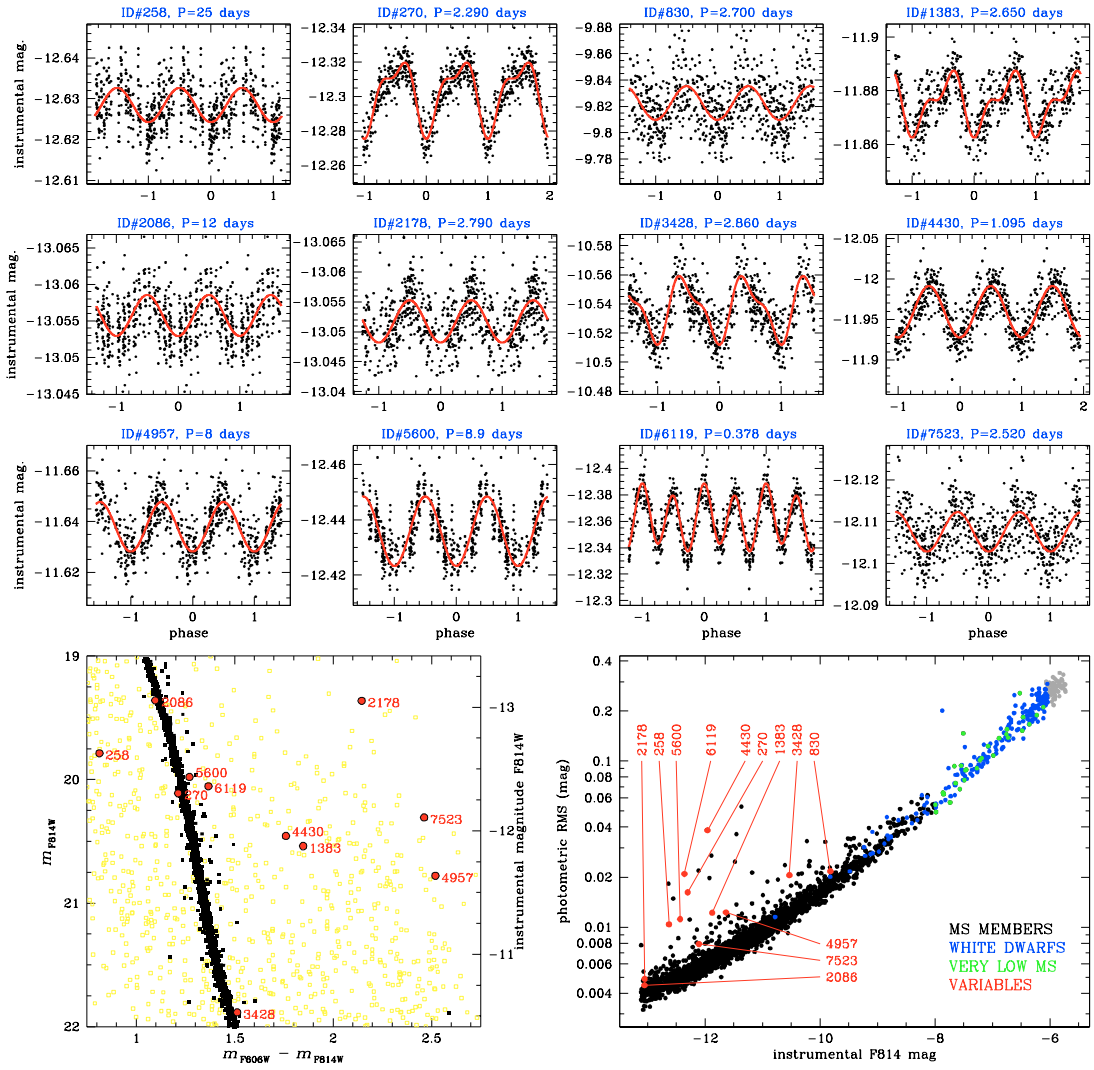

Figure 28: *Top panels:* light curves of the variable stars found (first twelve entries in Table 15), folded around the best-fit period. *Bottom left panel:* position of the variables (red IDs) in the ($m_{F606W} - m_{F814W}$,m_{F814W}) color-magnitude diagram. *Bottom right panel:* photometric RMS of the variables (red IDs) compared with all the analyzed light curves.

Table 15: Parameters for the variable stars found.

ID#	RA (2000.0) h:m:s	DEC (2000.0) d:m:s	m_{F814W}	$m_{F606W} - m_{F814W}$	p.m.(α) (pixels)	p.m.(δ) (pixels)	P (days)	Δm (mag)	N_{harm}	notes
3428	17:41:06.078	−53:45:47.62	21.884	1.513	−1.2192	0.4788	2.860	0.047	2	double-wave BY Dra
1383	17:41:11.653	−53:45:02.54	20.538	1.848	−1.3037	0.2494	2.650	0.025	2	double-wave BY Dra
270	17:41:14.751	−53:45:04.94	20.110	1.213	−1.0478	0.7856	2.290	0.044	2	double-wave BY Dra
6119	17:40:58.818	−53:45:41.10	20.054	1.367	−1.4436	0.5940	0.378	0.051	2	W UMa
4430	17:41:03.155	−53:44:49.11	20.456	1.761	−1.2356	0.4401	1.095	0.069	2	BY Dra?
830	17:41:13.183	−53:45:37.72	22.598	2.654	−1.3962	0.6337	2.700	0.026	1	BY Dra?
7523	17:40:55.370	−53:45:27.03	20.306	2.463	1.0304	0.5997	2.520	0.009	1	BY Dra? (weak)
2178	17:41:09.636	−53:43:17.61	19.362	2.146	−1.6238	0.5057	2.790	0.007	1	BY Dra? (weak)
5600	17:41:00.192	−53:42:46.28	19.979	1.271	−1.5276	0.3267	≈ 8.9	0.025	1	BY Dra?
4957	17:41:01.787	−53:43:31.37	20.778	2.520	−1.6460	0.3394	≈ 8	0.019	1	BY Dra?
2086	17:41:09.888	−53:43:10.59	19.359	1.097	−1.5737	0.3106	≈ 12	0.006	1	long period
258	17:41:14.789	−53:44:58.36	19.786	0.813	−1.7434	0.3614	≈ 25	0.008	1	long period
1882	17:41:10.379	−53:44:52.05	19.430	0.792	−1.0721	0.7363	0.920	0.005	1	spurious candidate?
5936	17:40:59.316	−53:44:06.51	20.524	1.493	0.0181	0.0055	2.120	0.080	–	grazing binary?

The columns give: the ID number of the star, the right ascension α and declination δ at epoch 2000.0, the calibrated magnitude m(F814W) and color m(F814W)−m(F606W), the proper motion (α,δ) in ACS-WFC pixels relative to the cluster, the period found in days, the amplitude found in magnitude, and the number of harmonics employed in the fit and a tentative interpretation.

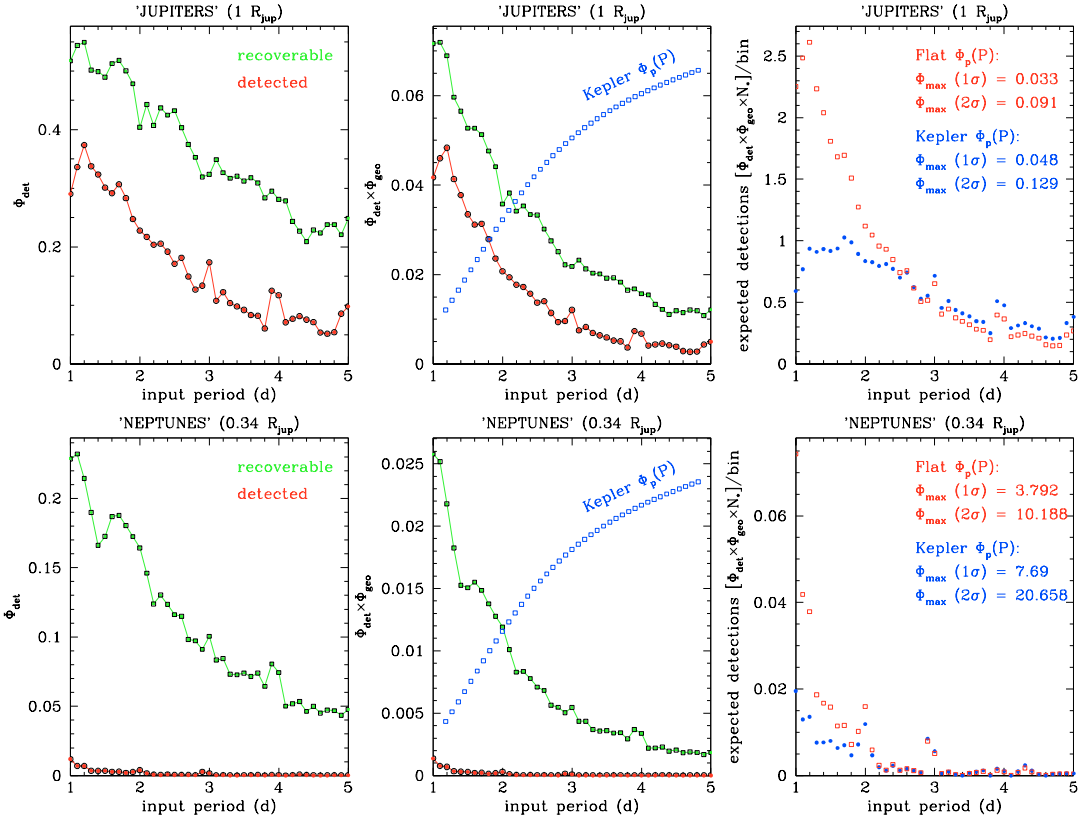

Figure 29: Completeness tests for cluster stars based on artificially injected transits, for 1 R_{jup} planets (upper row) and 0.336 R_{jup} planets (lower row). *Left panels:* detection efficiency Φ_{det} as a function of the input period, for planets potentially recoverable (green symbols) and for those planets effectively detected by the criterion in Eq. (23) (red symbols). *Middle panels:* same as above, but Φ_{det} is convolved with the geometrical probability Φ_{geo} for a planet to transit. The Howard et al. (2011) $\Phi_p(P)$ period distribution function is plotted in blue symbols (arbitrary normalization). *Right panels:* number of expected transit detections per period bin, assuming one planet per star within $1 < P < 5$ d. $\Phi_p(P)$ is assumed to be flat (red symbols) or as modeled by Howard et al. (2011) (blue symbols). 1- and 2-σ upper limits for the planet occurence $\Phi_{p,max}$ are shown.

where Φ_p is the fraction of stars with a planet, Φ_{geo} is the geometric *a priori* probability for that system to be aligned such that a transit occurs, Φ_{det} is the probability for that transit to be detected by our pipeline, and $N_\star$ is the number of target stars. As in our case we found that $N_p = 0$, we wished to estimate an upper limit to Φ_p, at least in the (P, R_p) range for which the efficiency of our search Φ_{det} is not negligible. Φ_{det} is expected to depend on the transit depth $(R_p/R_\star)^2$, the duration Δ, and the orbital period P.

For simplicity, our analysis was limited to two values of planetary radii: "Jupiter" planets (1 R_{jup}) and "Neptune" planets (0.338 R_{jup}). To estimate Φ_{det}, we ran simulations in a way similar to what has been done to set the detection threshold (Section 6.4.1). In each set of 2,215 simulated light curves, a synthetic transit was injected into each curve, with random uniform distributions of both P and $\sin i$ ($1 \leqslant P \leqslant 5$ d, $\sin i$ was constrained to allow transits). The process was iterated 200 times, for a total of 450,000 injections. We then tried to recover transits with BLS, by setting the same parameters and detection criterium defined in Eq. (23) and adopted for the real search. To derive Φ_{det}, the ratio of the detected to injected transits was evaluated for each 0.1-day bin of period P. The resulting distribution is plotted as a red line in the left panels of Fig. 29, as a function of the injected orbital period P_{in}. For comparison, the ratio of the "recoverable" transits (i.e., with at least two transits sampled and P/P_{in} =1:1, 3:2, 2:1) to the injected transits is plotted with a green line on the same panels. As expected, Φ_{det} is a decreasing function of P, with minor features at integer and semi-integer values of P owing to phasing effects. We note that for "Neptunes", Φ_{det} is extremely low (0.005–0.01) even for short periods ($P \sim$ 1–2 d). This is a consequence of inefficient sampling, which makes the significance of neptunian transits very weak: 3–4σ even for the most favourable case.

The geometric factor Φ_{geo} was calculated for each injected transit as $(R_p + R_\star)/a$ (a is the semimajor axis), and then convolved with Φ_{det} to obtain the probability of detecting transits on a star which is known to host a planet on a random orbit, as a function of its period (Fig. 29, middle panels).

We parametrized the "planet occurrence" following the analysis of Howard et al. (2011) for the distribution of 1,235 planetary candidates detected by Kepler. In this case, $\Phi_p(P)$ was assumed to be a power law modified with an exponential cut-off at period P_{cut}

$$\frac{d\Phi_p(P)}{d\log P} = k \cdot P^{\beta} \left(1 - e^{-(P/P_{cut})^{\gamma}}\right) \quad . \tag{25}$$

From Howard et al. (2011) we adopted the parameters: $k = 0.0025$, $\beta = 0.37$, $P_{cut} = 1.7$ days, $\gamma = 4.1$ for "Jupiters" ($8R_\oplus < R_p < 32R_\oplus$), and $k = 0.002$, $\beta = 0.79$, $P_{cut} = 2.2$ days, and $\gamma = 4.0$ for "Neptunes" ($4R_\oplus < R_p < 8R_\oplus$). $\Phi_p(P)$ is plotted, with an arbitrary normalization, as blue squares in the middle panels of Fig. 29.

We first normalized $\Phi_p(P)$ by imposing $\sum_1^5 \Phi_p(P) = 1$, that is assuming one planet with 1 d $< P <$ 5 d per star. The total number of expected detections $N_{exp}(\sum \Phi_p = 1)$ within each bin over the range $1 < P < 5$ d is $(\Phi_{det} \cdot \Phi_{geo} \cdot \Phi_p)\, N_\star$. By summing over the range $1 < P < 5$ d, we obtained $N_{exp} = 23.8$ expected detections of "Jupiters" and 0.14 of "Neptunes" (right panels of Fig. 29, blue symbols). For a flat $\Phi_p(P)$ distribution, N_{exp} is larger at 42.3 and 0.45, respectively.

The upper limit $\Phi_{p,max}$ to $\sum_1^5 \Phi_p(P)$ suggested by our null detection can be evaluated by simple binomial statistics, normalizing Φ_p in order to get a 68.27% (1σ) or 95.44% (2σ) probability of zero detections. We estimated for Jupiters that $\Phi_{p,max}(1\sigma) = 4.8\%$ and $\Phi_{p,max}(2\sigma) = 12.9\%$ assuming the Howard et al. (2011) Φ_p, and $\Phi_{p,max}$ $(1\sigma) = 3.3\%$, $\Phi_{p,max}(2\sigma) = 9.1\%$ assuming a flat Φ_p. As expected, $\Phi_{p,max}$ is well above unity for the "Neptune" sample, leaving this planetary population essentially unconstrained by our data (Fig. 29, lower right panel).

6.6 DISCUSSION AND CONCLUSIONS

We have performed a search for planetary transits and variability among 5,078 stars imaged in one of the deepest ACS fields ever observed, which had been originally acquired to probe the bottom of the main sequence of the metal-poor globular cluster NGC 6397. The sample includes 2,215 M0-M9 dwarfs of secure membership. Though these data were not optimized for such a study, this is the largest homogeneous sample of M dwarfs ever searched for variability.

Instrumental drifts and systematic errors caused by dithering required a careful empirical correction, described in Section 6.3. We developed and implemented algorithms that allowed us to approach the theoretical noise limit across the whole magnitude range $19 \lesssim m_{F814W} \lesssim 26$. The brightest cluster members (M0V) were measured with an average scatter of 0.003-0.004 mag over a time span of 28 days, illustrating the power of our decorrelating techniques and the feasibility of transit searches in the low main sequence of GCs.

We found no valid planetary transit above the significance threshold that we set from simulations. Considering only cluster stars, whose physical parameters can be reliabily infered, this null detection sets an upper limit to the fraction of stars hosting a $P < 5$ d Jupiter-sized planet to about $\Phi_p = 4.8\%$ at 1-σ confidence and 12.9% at 2-σ, assuming the planetary radius distribution derived by Howard et al. (2011) from Kepler data. In other words, only 0.13 detections are expected assuming that the underlying planetary population is similar to that studied by Kepler. Most studies based on RVs also hypotesized $\Phi_p < 1\%$ for short-period, Jupiter-sized planets around solar-type stars (Marcy et al. 2005). Furthermore, Φ_p is expected to be a

very steep function of the stellar metallicity (Fischer & Valenti 2005). Therefore, we are unable to make any firm conclusion about the occurrence of giant planets in NGC 6397.

As demonstrated in Section 6.4.1, our data set is not sensitive enough to Neptune-sized planets to draw any conclusion about their occurrence, though a much higher Φ_p is expected for M dwarfs by Howard et al. (2011) and Lovis et al. (2009), among others. This was due to an inefficient sampling of the time series available from archive material, which translated into poor phase coverage and severe undersampling of transit-like events, whose duration is expected to be on the same order as the effective cadence.

Twelve new variable stars have been identified in the NGC 6397 field (Table 15). Most of these can be classified as BY Draconis variables, that is, spotted rotating KM dwarfs. Interestingly, no variable has been detected among the 2,430 cluster members. Hundreds of member early-M dwarfs ($m_{F814W} < 21$, Fig. 25) follow the expected noise on timescales of up to 28 days, though they were measured with a 0.003-0.006 mag precision. The lack of eclipsing binaries is unsurprising. The number of expected detections can be estimated by scaling down the number of EBs detected by Albrow et al. (2001) for 47 Tuc. If one takes into account the smaller fraction of binaries in NGC 6397 ($< 3\%$, even at radii smaller than the half-mass radius, **?**) and the smaller number of targets (2,215 vs. 46,422), we would expect much less than one EB. On the other hand, the lack of BY Dra variables is more puzzling, as one would expect 4-5 such detections, considering the number of monitored cluster stars in this paper. We note that our stars are cooler than the Albrow et al. (2001) sample, and we should expect longer photometric periods. Our search is insensitive to periods $\gtrsim 28$ days, so this could be a possible explanation.

We evaluated an upper limit to the photometric jitter σ_{jit} of the brightest members (M0V) by subtracting the contribution of the expected noise σ_{exp} to the measured scatter σ_{obs} (that is, assuming $\sigma^2_{jit} = \sigma^2_{obs} - \sigma^2_{exp}$). The fraction of stars f with $\sigma_{jit} > 2$ mmag is $f \lesssim 2\%$. This value should be compared with the results found by Ciardi et al. (2011) examining the first quarter of Kepler photometry on 2,182 field M dwarfs: these data cover an interval of 33 days with an average cadence of 30 minutes, which is quite similar to our cadence and time scale. They found a fraction $f \simeq 20\%$ of stars with $\sigma > 2$ mmag, that is at least an order of magnitude larger fraction than that we measured in NGC 6397. The low MS of this cluster is extremely stable and therefore worth targeting using more optimized observations. The James Webb Space Telescope Near-Infrared Camera (NIRCam), for instance, would be able to probe the bottom of the MS of NGC 6397 ($m_{F814W} \sim 24$) with a photometric precision better than 0.01 mag in a single 600 s exposure, without any of the coverage/sampling issues mentioned above.

Most of the analysis techniques presented in this paper can also be applied (with little or no modification) to other existing ACS/WFC3 time series of rich stellar fields. This is the case for the metal-rich globular cluster 47 Tucanae, which has been imaged with ACS and WFC3 over a longer time-frame. Such a search for transits will allow us to complement the results of Gilliland et al. (2000) in a different range of spectral types and planetary masses.

Acknowledgements

Based on observations with the NASA/ESA Hubble Space Telescope, obtained at the Space Telescope Science Institute, which is operated by AURA, Inc., under NASA contract NAS 5-26555. This work was partially supported by PRIN INAF 2008 "Environmental effects in the formation and evolution of extrasolar planetary system". V.N. acknowledges support by STScI grant DDRF D0001.82432. We thank Ennio Poretti for helping us to identify the variable stars. We thank Aaron Dotter for providing us with the isochrones used in Richer et al. (2008) and presented in Dotter et al. (2007). Some tasks of our data analysis have been carried out with the VARTOOLS code (Hartman et al. 2008). We thank Ron Gilliland for his useful comments and suggestions.

7

FIELD SELECTION FOR PLATO

Plato will search primarily for low-mass, habitable planets around bright stars, covering up to the ~ 40% of the sky at the end of the mission. Suitable targets (dwarfs and subgiants later than spectral type F5, down to $V \sim 13$) have to be selected in advance. An unprecedented all-sky stellar classification is then needed. Within the Working Package (WP 131210: "Analysis of photometric and astrometric catalogues") I evaluated the feasibility and reliability of stellar classification techniques based upon the existing and forthcoming photometric/astrometric catalogs.

7.1 INTRODUCTION

During its five-year mission, Plato will image two "long-duration" fields (for three and two years, respectively) and a lager number of supplementary fields for two months each, during the "step-and-stare" phase. The thirty-two "normal" telescopes are subdivided in four groups, each groups pointing in a direction which is displaced by ~ 9.2 degrees from the center of the overall FOV. Such strategy provides a non-uniform coverage of instanteous ~ 2300 deg^2 field: 353 deg^2 are imaged by thirty-two telescopes, ~ 264 deg^2 by twenty-four, ~ 749 deg^2 by sixteeen, and ~ 928 deg^2 by eight telescopes. This gives rise to the characteristic "flower-shaped" Plato Field (Fig. 30). Two additional "fast" telescopes will provide photometry with a faster cadence and with color information.

Observational constraints requires that the centers of both long-duration fields lie within two "allowed regions" defined by a ecliptic latitude $|\beta| > 60°$. Both these two regions, one in the north an one in the south emisphere, are simmetrically located at high declination ($|\delta| \gtrsim 40°$), include the celestial poles, and are tangent to the galactic plane in two points (at $l \sim 276°$, $l \sim 96°$ respectively). The allowed regions are only slightly larger (~ 2750 deg^2) than the Plato FOV, but that constraint holds only for the center of the field. It is easy to see that the area covered by the envelope of every possible long-duration field is huge: about 40% of the whole sky.

Plato will perform most of the reduction tasks on-board, sending back to Earth only light curves and centroids for most targets (while for a selected sample of stars also small images will be downloaded around the target). The number of measured targets itself is limited by telemetry and by computational power. The Plato Scientific Require-

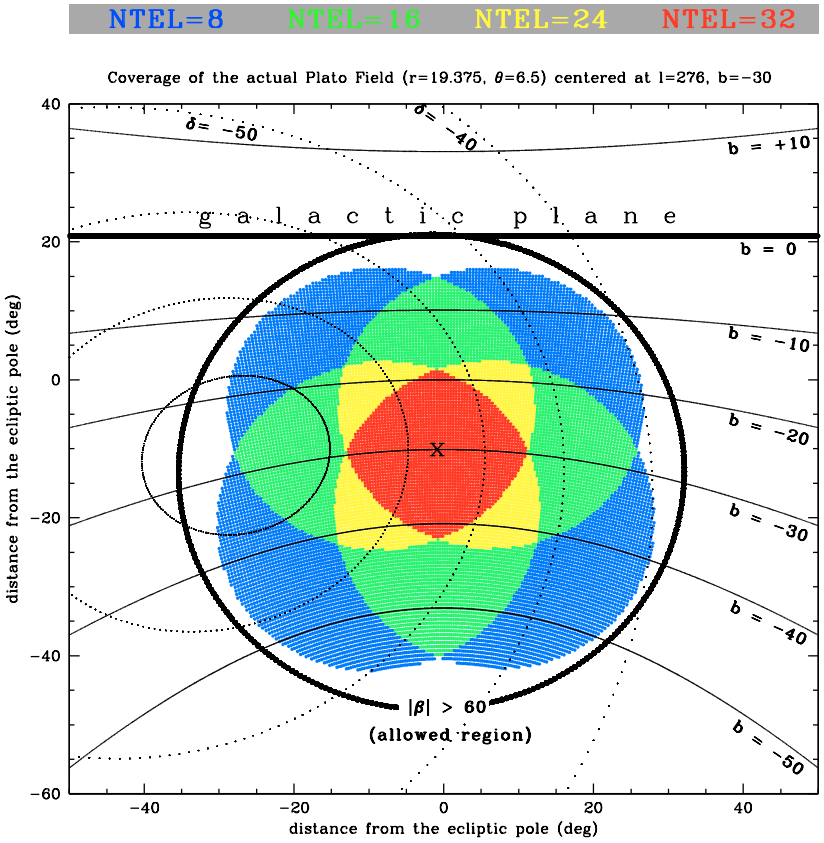

Figure 30: The Plato Field coverage based upon the actual design (diameter of the field of each telescope: 19.37 deg, displacement from the center of the pointing: 9.2 deg.). The region covered by 8, 16, 24, 32 telescopes are coded in different colors. The field here is pointed at the center of one of the two regions allowed for the long-duration fields ($|\beta| > 60$).

ments Document (Sci-RD) defines five complementary stellar samples to be surveyed, which are listed below by order of priority:

P1: $\gtrsim$20,000 dwarfs and subgiants later than spectral type F5, for which the photometric noise level is below 27 ppm/h, to be observed during the long monitoring phases.

P2: : $\gtrsim$1,000 dwarfs and subgiants later than spectral type F5 brighter than $m_V = 8$, for which the photometric noise level is below 27 ppm/h, to be observed during the long monitoring phases.

P3: $\gtrsim$3,000 dwarfs and subgiants later than spectral type F5 brighter than $m_V = 8$, for which the photometric noise level is below 27 ppm/h, to be observed during either the long monitoring phases or during the shorter runs of the Step&Stare phase. The P3 sample is an extension of the P2 sample, i.e. P2 sample is included in P3 sample.

P4: $\gtrsim$10,000 cool M dwarfs, with at least 5,000 monitored during the long pointing phases of the mission, and more than 5,000 during the Step&Stare phase, for which the photometric noise level is below 800 ppm/h.

P5: $\gtrsim$245,000 dwarfs and subgiants later than spectral type F5, for which the photometric noise level is below 80 ppm/h, to be observed during the long monitoring phases.

In addition, the number of cool dwarfs and subgiants down to $m_V = 11$ must be maximized, as these are the stars for which ground-based radial velocity follow-up will be most effective.

As Plato will not download the full images of its FOV, the samples P1-P5 have to be selected in advance. This requires the deepest all-sky stellar classification ever attempted: to assign at least the spectral type and the luminosity class to every star brighter than $V = 13$. This should be viewed as the minimal requirement for the selection of the targets. However, the previous experience of the CoRoT and Kepler space missions (Auvergne et al. 2009; Borucki et al. 2010) has shown that detailed knowledge of the stellar parameters (such as $T_{\rm eff}$, $\log(g)$, [M/H], $R_\star$, $M_\star$, age, ...) makes the follow-up and the rejection of false alarms much more efficient, and helps the prioritization of the targets. These entries and other TBD will constitute the core of the Plato Input Catalog (PIC), from which the P1-P5 target lists will be drawn.

The GAIA Mission, to be launched in 2012, is expected to play a fundamental role in the PIC compilation, by performing an unprecedented ultra-high-precision astrometric survey of nearly every source brighter than $V \sim 20$, along with low-resolution spectrophotometry and radial velocities (`http://sci.esa.int/gaia/`). An early-release catalog is expected in 2015. However, we have to keep in mind that 1)

the compilation of the PIC should not depend upon a single point-of-failure 2) the GAIA classification will be affected by crowing in the densest regions (Zwitter & Henden 2003) 3) there will be degeneration among certain parameters, such as temperature and interstellar extinction (Straižys et al. 2006; Bailer-Jones 2010b) 4) other astronomical catalogs (for instance, X/UV/IR/narrow-band photometry and activity diagnostics) are strongly complementary to the GAIA measurements 5) at least the position of the first long-duration field has to be chosen before 2015.

The working package 131210 is carrying out an analysis of the published or forthcoming astrometric/photometric catalogs, in order to perform an all-sky stellar classification using data that is already available, or that will become available before 2015. The best techniques developed to this purpose will be reviewed and compared. External validation will be obtained cross-matching the results with existing realiable spectral classifications.

7.2 THE BASIC PROBLEM

The most reliable stellar classification is provided by spectra and trigonometric parallaxes, from which it is possible to extract the basic parameters of the stellar atmosphere (T_{eff}, $\log(g)$, $[M/H]$) and the distance in a relatively straightfoward way. Once these parameters are known, we can use stellar models to derive other important physical quantities such as the radius $R_\star$, the mass $M_\star$, and the age of the star.

Unfortunately, both spectroscopy and high-precision astrometry are time-consuming. Until GAIA will begin to release data, neither techniques are feasible to characterize hundreds of thousands of stars on an extremely large field of view (such as the Plato field). The only available all-sky classifications of this kind are limited at sources brighter than $V \sim 8$ (HD/MK/Geneva-Copenhagen spectroscopical/-narrowband surveys, and the Hipparcos Catalogue). So far, we must rely on the only all-sky available catalogs that reach at least the $V = 13$ magnitude limit required by the Plato P5 sample: wide-band photometric catalogs (both in the visible and in the near-infrared region of the spectrum) and astrometric catalogs (which are accurate enough to provide good proper motions, but not for trigonometric parallaxes). For a detailed review of the main standard photometric systems, see Bessell (2005). A summary of calibrated broad-band colors and physical properties of typical main sequence, solar-metallicity dwarfs is given in Table 16, pag. 117 from Cox (2000).

Using wide-band photometry to derive stellar parameters is a challenging task for many reasons. First of all, over most of the visible spectrum, the expected differences in color between cool stars of similar T_{eff}/SpT but different surface gravity and metallicity is at most few tenths of mag, when using suitable narrow- or intermediate-band

SpT	M(V)	B − V	U − B	V − R	R − I	V − K	J − H	H − K	T_{eff}	BC	$M/M_{\odot}$	$R/R_{\odot}$	$\log(g/g_{\odot})$	$\log(\rho/\rho_{\odot})$	v_{rot}
O5V	-5.70	-0.33	-1.19	-0.15	-0.32	-0.87	-0.14	-0.04	42,000	-4.40	60	12	-0.40	-1.50	
O9V	-4.50	-0.31	-1.12	-0.15	-0.32	-0.83	-0.12	-0.04	34,000	-3.33	23	8.5	-0.50	-1.40	200
B0V	-4.00	-0.30	-1.08	-0.13	-0.29	-0.66	-0.09	-0.03	30,000	-3.16	17.5	7.4	-0.50	-1.40	170
B2V	-2.45	-0.24	-0.84	-0.10	-0.22	-0.42	-0.06	-0.01	20,900	-2.35	7.6	4.8	-0.50	-1.15	190
B5V	-1.20	-0.17	-0.58	-0.06	-0.16	-0.24	-0.03	0.00	15,200	-1.46	5.9	3.9	-0.40	-1.00	240
B8V	-0.25	-0.11	-0.34	-0.02	-0.10	0.00	0.00	0.00	11,400	-0.80	3.8	3	-0.40	-0.85	220
A0V	0.65	-0.02	-0.02	0.02	-0.02	0.14	0.02	0.01	9,790	-0.30	2.9	2.4	-0.30	-0.70	180
A2V	1.30	0.05	0.05	0.08	0.01	0.38	0.06	0.02	9,000	-0.20					
A5V	1.95	0.15	0.10	0.16	0.06	0.70	0.13	0.03	8,180	-0.15	2	1.7	-0.15	-0.40	170
F0V	2.70	0.30	0.03	0.30	0.17	0.82	0.17	0.04	7,300	-0.09	1.6	1.5	-0.10	-0.30	100
F2V	3.60	0.35	0.00	0.35	0.20	1.10	0.23	0.04	7,000	-0.11					
F5V	3.50	0.44	-0.02	0.40	0.24	1.32	0.29	0.05	6,650	-0.14	1.4	1.3	-0.10	-0.20	30
F8V	4.00	0.52	0.02	0.47	0.29	1.41	0.31	0.05	6,250	-0.16					
G0V	4.40	0.58	0.06	0.50	0.31	1.46	0.32	0.05	5,940	-0.18	1.05	1.1	-0.05	-0.10	10
G2V	4.70	0.63	0.12	0.53	0.33	1.58	0.35	0.06	5,790	-0.20					
G5V	5.10	0.68	0.20	0.54	0.35				5,560	-0.21	0.92	0.92	0.05	-0.10	< 10
G8V	5.50	0.74	0.30	0.58	0.38	1.96	0.45	0.08	5,310	-0.40					
K0V	5.90	0.81	0.45	0.64	0.42	2.22	0.50	0.09	5,150	-0.31	0.79	0.85	0.05	0.10	< 10
K2V	6.40	0.91	0.64	0.74	0.48	2.85	0.61	0.11	4,830	-0.42					
K5V	7.35	1.15	1.08	0.99	0.63				4,410	-0.72	0.67	0.72	0.10	0.25	< 10
M0V	8.80	1.40	1.22	1.28	0.91	3.65	0.67	0.17	3,840	-1.38	0.51	0.6	0.15	0.35	
M2V	9.90	1.49	1.18	1.50	1.19	4.11	0.66	0.20	3,520	-1.89	0.4	0.5	0.20	0.80	
M5V	12.30	1.64	1.24	1.80	1.67	6.17	0.62	0.33	3,170	-2.73	0.21	0.27	0.50	1.00	

Table 16: Calibration of MK spectral types, from *Allen's Astrophysical Quantities* (Cox 2000): absolute magnitude, colors in Johnson-Cousins and JHK bands, effective surface temperature, bolometric correction, mass, radius, surface gravity, density and rotational velocity for the MK dwarf spectral classes. All calibrations are made for solar-metallicity, ZAMS stars.

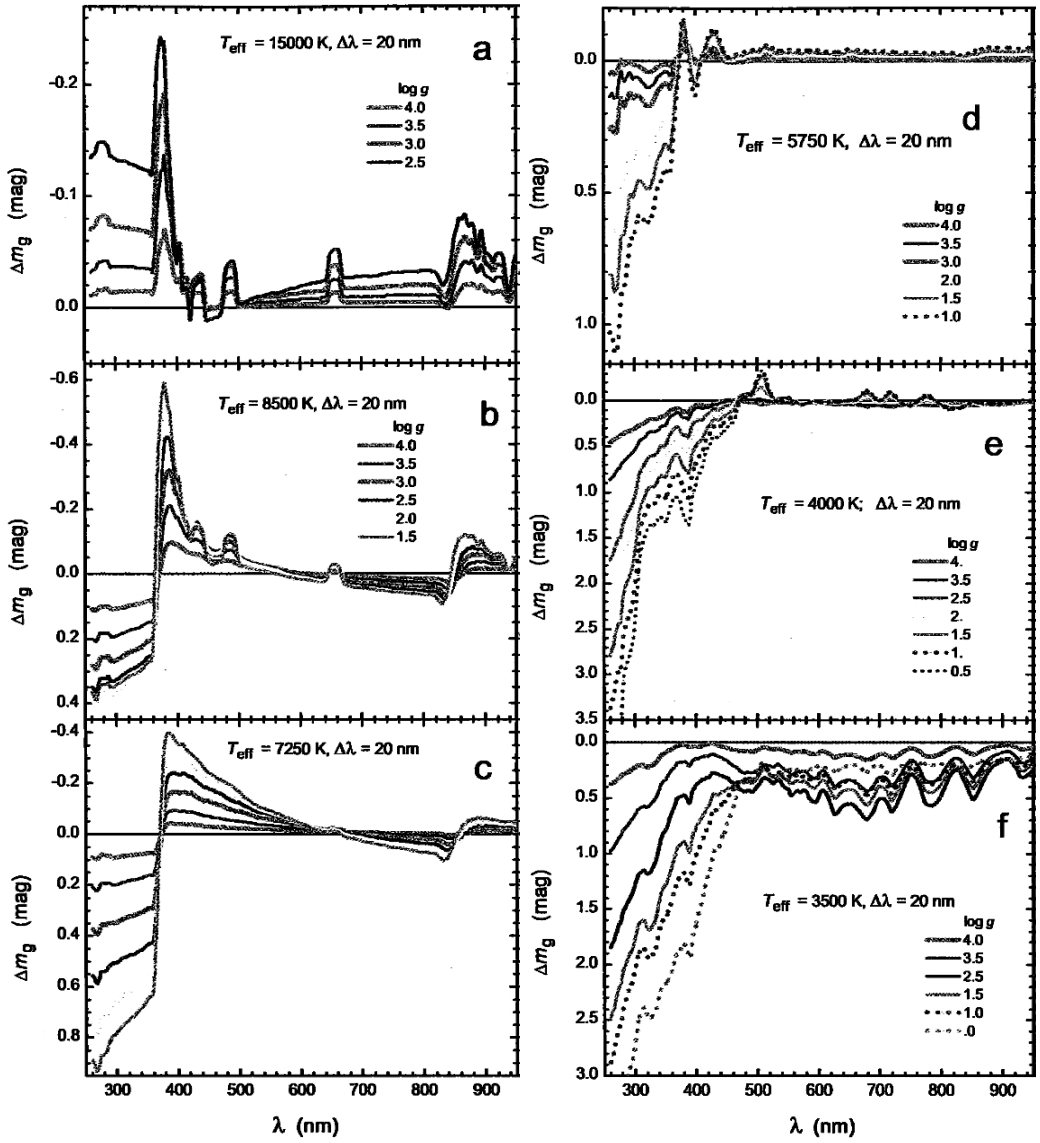

Figure 31: The magnitude differences Δm_g due to changes of $\log g$ when T_{eff} is constant, evaluated over passbands with $\Delta\lambda = 200$ Å. Δm_g is defined zero for $\log g = 4.5$. For each panel the approx. SpT is a) B5, b) A3, c) F0, d) G2, f) K8, g) M5. All models are for $[M/H] = 0$. From Zdanavičius (2005).

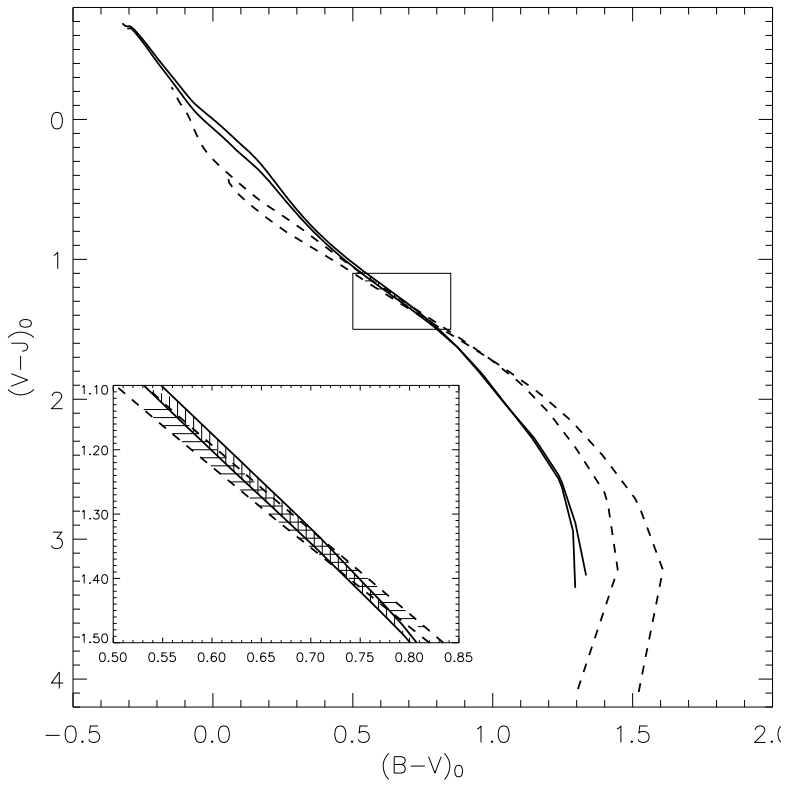

Figure 32: Synthetic color-color diagram for $(B-V)_0$ and $(V-J)_0$ colors. Solid lines are for metallicity $[M/H] = -0.5$ and $\log g$ between 4.5 and 5.0, dashed lines for solar metallicity and $\log g$ between 1.0 and 2.0. For late F- and G-type stars there is a clear degeneration between gravity and metallicity. From Belikov & Röser (2008).

filters (Zdanavičius 2005, see Fig. 31). When the spectral energy distribution of those stars is integrated over the wavelength ranges of a typical wide-band photometric system ($\Delta\lambda \sim 1000$Å) the differences fade to only few hundredths of mag. A notable exception is in the spectral region bluer than the Balmer Jump, which is sampled both by the Johnson U and by the SDSS u′ filters (Fig. 31; see also Zdanavicius 1998). Unluckily, these magnitudes are the most difficult to measure and calibrate, due to a combination of atmospheric effects, standardization issues and low instrumental sensitivity (Bessell 2005). No all-sky, deep catalogs of UV magnitudes are available so far.

Even more important, wide-band photometric classifications are known to be highly degenerate for some stellar parameters, such as metallicity and gravity; see for instance the example reported by Belikov & Röser (2008), shown in Fig. 32. By using a B, V, J two-color diagram it is not possibile to discriminate between a metal-poor dwarf and a solar-metallicity giant, both of G spectral type. F and G stars are expected to dominate the Plato target samples, and is also the region where most degeneracy occurs. A further source of degeneracy is the interstellar reddening, which is not negligible in a magnitude-limited

sample of stars at low galactic latitude, as most Plato targets will be. In particular, $E(B-V)$ (or A_V) and T_{eff} are degenerate: a distant, hot star can be misclassified as a close and cool star. To a lesser extent, this holds also for NIR photometry, and even when parallaxes and low-resolution spectra are available (Bailer-Jones 2010b,a).

The most important task of the PIC will be to tell dwarfs from giants for the spectral types ranging from late F stars down to the late M ones. The most relevant spectral regions are therefore those sensitive to $\log(g)$, and not much sensitive to metallicity. Aside from the UV wavelenghts, the most prominent features are located on the continuum at $4000-4500$Å (mostly for the F-G spectral types) and at the MgI triplet absorption feature at 5150Å (mostly for G-K spectral types, as shown by Teig 2008). Most of narrow- and intermediate-band photometric systems developed for stellar classification purposes, as well as the G_{red} and DDO51 filters originally designed for the Kepler Input Catalog survey (KIC; Batalha et al. 2010) are taylored on these spectral features. As for the wide-band photometry, we note that the three above-mentioned features fall roughly inside the Johnson U, B, V bands, though their contribute is greatly diluted by the width of the bands and it never exceeds few hundreths of magnitude on the $B-V$ color, for instance. Cousins R_c and I_c bands are relatively insensitive to $\log(g)$, except for the spectral class M. Results from synthetic photometry applied on M dwarfs should be taken with caution, however, as the theoretical uncertainties on their atmospheric opacities make their calculated SEDs to differ from the observed ones (Zdanavičius 2005).

Near-infrared wide-band photometry, that is carried out in the JHK or JHK_s bands by most ground-based surveys (such as 2MASS), is especially effective in higlightning gravity effects on late spectral types. $H-K$ or $H-K_s$ color, for instance, can differ by few tenths of magnitude between M-dwarfs and M-giants (Lépine & Shara 2005), and this technique works also for some late K stars. However, the effects become smaller and more degenerate for earlier type such as F and G, which are expected to dominate by far the Plato P1-3 and P5 samples. NIR colors are less affected by interstellar extinction, still in fields at very low galactic latitude reddening effects are not negligible.

Proper motions, which are provided with a typical accuracy of few mas/yr by the Tycho-2 and UCAC3 surveys, are helpful in discriminating dwarfs from giants when combined with photometric colors. The Reduced Proper Motion technique (RPM) is very effective for selecting dwarfs among bright ($V \lesssim 11$) stars of latest spectral types (K-M, Gould & Morgan 2003; Gontcharov 2009). For fainter stars, and for F and G spectral types the RPMs are less effective, and a large fraction of false positives is expected (Gould & Morgan 2003). However, for $V \lesssim 13.5$ targets, and applying the same criteria using NIR colors (to minimize the reddening) should yeld acceptable results (Gould &

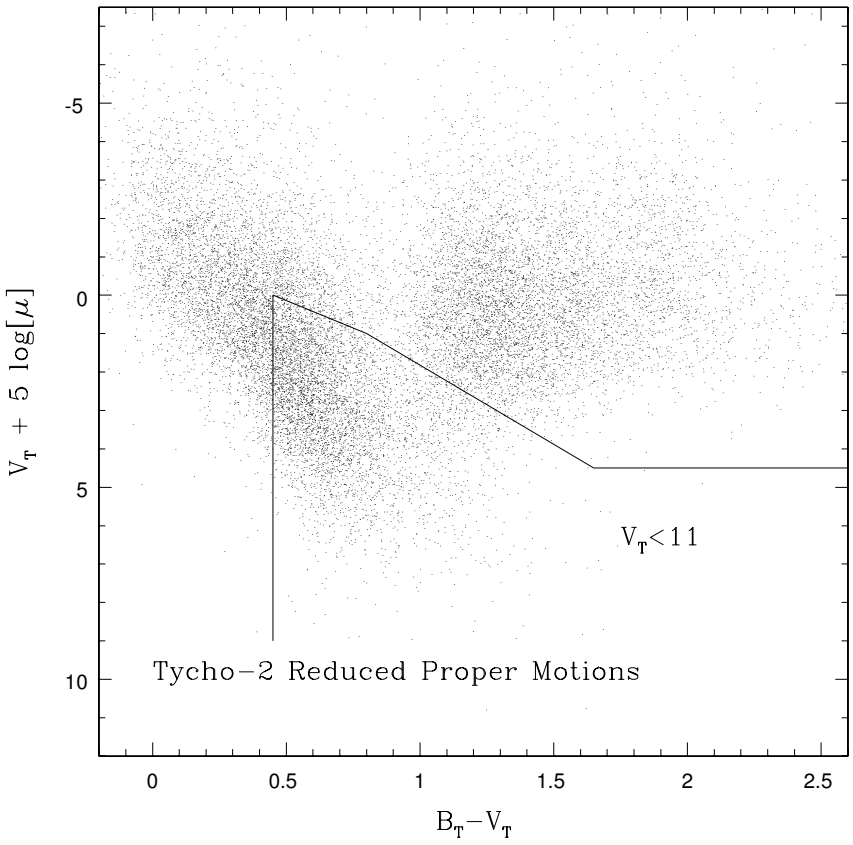

Figure 33: Reduce proper motion (RPM) diagram constructed from Tycho-2 proper motions and colors ($V < 11$), with the selection criteria for $R_\star < 1.25 R_\odot$ adopted by Gould & Morgan (2003). At least 90% of the existing dwarfs are estimated to have been selected, while the $\sim 60\%$ of the sample are contaminating giant stars.

Morgan 2003). While the maximum level of contamination required for the P1-P5 samples has not been explicitly assessed yet, we note that Plato has the capability to observe much more targets than the minimum number stated in the requirements. We can then perform conservative selections of our dwarfs by maximizing the completeness of our sample, and than reject the contaminating giants at a later stage of the mission. The RPM technique, by itself, cannot provide stellar parameters other than a very rough estimate of the absolute magnitude. In addition, selection cuts based upon on the proper motions have to be done with care, as the resulting sample can be biased in a subtle way toward thick disk or halo targets (Lépine & Shara 2005).

In summary, to assign a reliable set of stellar parameters to every possible candidate for the inclusion in the P1-P5 samples is a challenging task with the existing data, and requires an assembly of different tools and data types. Even so, the estimated stellar parameters can have large uncertainties or be affected by degeneration. Nevertheless, the minimal task required by the scientific objectives of the Plato mission (that is, to properly select targets which are suitable for detect and characterize earth-like planets) appears feasible when some degree of contamination is allowed in the sample.

7.3 THE AVAILABLE CATALOGS

The astrometric and photometric catalogs that are already available –and that could be useful for stellar classification purposes– will be reviewed. Some informations in this section are taken from the ASDC document "*Catalogues for PIC implementation*" (draft). A comparison between the properties of those catalogs is summarized in Tab. 17.

7.3.1 *Hipparcos*

The Hipparcos astrometric catalog, containing 117,955 stars, is one of the final products of the Hipparcos mission and was originally released in June 1997 (Perryman & ESA 1997). It provides absolute positions and trigonometric parallaxes, as well as photometry in one custom wide band named H_p. For bright stars, the photometric precision can be as high as 0.004 mag. The completeness limit is dependent upon the galatic latitude, ranging from $H_p \sim 9$ down to $H_p \sim 7.2$ along the galactic plane (roughly equal to $V \sim 9, 7.2$ for F-K stars). A small number of stars down to $H_p \sim 12$ was also included.

A new reduction of the astrometric data as produced by the Hipparcos mission has been published, reporting accuracies for nearly all stars brighter than magnitude $H_p = 8$ to be better, by up to a factor 4, than in the original catalogue (van Leeuwen 2007). The new reduction of the Hipparcos astrometric data provides an improvement by a

NAME	coverage	released	V_{lim}	V_{sat}	bands	σ_{phot} (mag)	σ_{xy} (mas)	P.M.	notes
Hipparcos	100%	yes	8		H_p	0.001-0.002	1-3	yes	parallaxes
Tycho-2	100%	yes	11		$B_T V_T$	0.013-0.1	7-60	yes	
USNO-A2.0	100%	yes	20	11	$\sim$ BR	0.3	250	no	
USNO-B1.0	100%	yes	21	11	$\sim$ BRI	0.3	200	yes	
GSC 2.3	100%	yes	20	11	$B_j R_f I_N V$	0.13-0.22	200-300	yes	
UCAC3	100%	yes	16		wide	-	15-20	yes	only astrometric
2MASS	100%	yes	17	7-8	JHK_s	0.01-0.15	70	no	
SDSS	25%	2016	22		ugriz	0.02-0.03	100	yes	+spectra
APASS	15%	?	17		$BVg'r'i'$	0.01-0.03	100-250	no	
ASAS/AASC	>50%	partial	14		VI	0.05-0.1	-	no	variability survey
Skymapper	-	?	16-23	8-9	ugriz + v_s	0.03	50	?	only South
PAN-Starrs	-	2013	24		wide + griz	0.01	70	yes	only North
LSST	-	2017	24		ugrizY	0.01	20	yes	only South
Gaia	-	2015 (ER)	20		LR spectra	<0.01	0.02	yes	plx, RV, spectra

Table 17: Comparison between the main photometric and astrometric catalogs reviewed for this work. When available, for each entry are provided: the actual coverage as fraction of the sky, the approximate V magnitude range, the photometric system employed, the photometric and astrometic error for typical, well-exposed targets, and the availability of proper motions.

factor 2.2 in the total weight compared to the catalogue published in 1997, and provides much improved data for a wide range of studies on stellar luminosities and local galactic kinematics. This revision is the most accurate astrometric catalog available, with about 1 mas of error on the absolute position of the stars.

7.3.2 *Tycho-2*

The Tycho-2 Catalogue is an astrometric reference catalogue for the ~2.5 million brightest stars in the sky, collected by the star mapper of the ESA Hipparcos satellite (Høg et al. 2000). The astrometric precision of Tycho-2 is much lower than the Hipparcos Catalogue (between 7 and 60 mas, dependent upon the magnitude) but it provides also photometry in two bands named B_T and V_T, whose bandpasses are similar to the Johnson B and V filters. The photometric precision ranges from 0.013 to 0.1 mag for the fainter targets. The nominal completeness limit is about $V = 11.2 - 11.5$ at 90 and 99%, respectively, though it has to be further assessed near the galactic plane. Only extremely bright stars saturate ($B_T, V_T \lesssim 2$).

The Tycho-2 positions and magnitudes are based on precisely the same observations as the original Tycho Catalogue (Tycho-1), but Tycho-2 is much bigger and slightly more precise, owing to a more advanced reduction technique. Components of double stars with separations down to 0.8 arcsec are included. Proper motions precise to about 2.5 mas/yr are given as derived from a comparison with the Astrographic Catalogue and 143 other ground-based astrometric catalogues, all reduced to the Hipparcos celestial coordinate system.

7.3.3 *2MASS*

2MASS is the deepest near-infrared all-sky survey available (Skrutskie et al. 2003), carried out in the JHK_s bands. The 2MASS All-Sky Data Release covers 99.998% of the sky, derived from all northern and southern observations. The All-Sky Release products include a Point Source Catalog (PSC), containing positions and photometry for 470,992,970 objects, an Extended Source Catalog (XSC), containing positions, photometry and basic shape information for 1,647,599 resolved sources, most of which are galaxies, and the Image Atlas, containing over 4,121,439 J, H and K_s FITS images.

At high galactic latitude ($b > 30$ deg), 2MASS is complete at 99% level down to $J = 16.1$, $H = 15.5$, $K_s = 15.1$, i.e. about $V \gtrsim 16$ for spectral types F-M. The typical photometric precision is between 0.01 and 0.05 mag, decreasing for the faintest targets and when approaching the saturation limit ($J = 4.5$, $H = 4$, $K_s = 3.5$). The astrometric accuracy is 70-80 mas for $9 < K_s < 14$ sources and 120 mas at $K_s < 9$, but no proper motions are provided.

7.3.4 *USNO-B1.0, GSC-2.3*

USNO-* and GSC-* are families of catalogs derived from digitized photographic plates at epochs ranging from 1950 to 1999. They are the deepest optical catalogs available, providing multiband all-sky coverage with a completeness limit at about $V \sim 19$. On the other hand, the source material limits the typical photometric precision to $0.1 - 0.3$ mag and the astrometric accuracy to 200-300 mas, even for the best stars.

USNO-B (Monet et al. 2003) presents positions, proper motions, magnitudes in the photographic passbands O, E, J, F, N (renamed B_1, R_1, B_2, R_2, I and roughly corresponding to Johnson passbands BRI), and star/galaxy estimators for 1,042,618,261 objects derived from 3,643,201,733 separate observations. The data were obtained from scans of 7435 Schmidt plates taken for the various sky surveys during the last 50 years.

The Guide Star Catalog II (GSC-II, Lasker et al. 2008) is an all-sky database of objects derived from the uncompressed Digitized Sky Surveys that the Space Telescope Science Institute has created from the Palomar and UK Schmidt survey plates and made available to the community. Like its predecessor (GSC-I), the GSC-II was primarily created to provide guide star information and observation planning support for Hubble Space Telescope. Magnitudes are provided in the photographic passbands B_J R_f, I_N and V with different coverage (B_J and R_F being the most complete), completemented with Tycho-2 measurements at the bright end. GSC-2.3 claims a slightly better photometric accuracy and more refined rejection of artefacts. Anyway, data sources close to bright stars, or in crowded fields, have to be treated with caution when dealing with both catalogs.

7.3.5 *UCAC3*

UCAC3 (Zacharias et al. 2010) is a compiled, all-sky astrometric catalog designed to provide high-quality CCD positions and proper motions for targets fainter than the limiting magnitude of Hipparcos and Tycho-2. The star catalog covers mainly the $R = 7.5$ to 16.3 range in a single wide bandpass between Johnson V and R. Most observations were carried out in non-photometric conditions. However, UCAC3 magnitudes has been calibrated against Tycho-2 stars and systematic errors are probably constrained within 0.1 mag.

Positional errors are about 15 to 20 mas for stars in the 10 to 14 mag range. It is supplemented by proper motions and SuperCosmos and 2MASS photometric data, as well as various flags. The proper motions of bright stars are based on about 140 catalogs, including Hipparcos and Tycho, as well as all catalogs used for the Tycho-2 proper motion construction. Proper motions of faint stars are based

on a re-reduction of early epoch SPM data (-90 to -10 deg Dec) plus Schmidt plate data from the SuperCosmos project (down weighted due to systematic errors of order 100 mas). A UCAC4 release is anticipated in the future.

7.3.6 *SDSS*

The Sloan Digital Sky Survey[1] (SDSS) DR7 (Abazajian et al. 2009) represents the completion of the SDSS Legacy project, which consists of an imaging survey in five bands (ugriz) over a contiguous 7646 deg^2 high-latitude elliptical region in the Northern Galactic Cap, plus an additional 750 deg^2 in the Southern Galactic Cap, together with spectroscopy of complete samples of galaxies and quasars covering about 8200 deg^2. The total imaging area in the Legacy survey is 8423 deg^2.

The photometric catalog is 95% complete down to $g \simeq 22.0$, with typical calibration errors of 0.02-0.03 mag. Positional accuracy is about 100 mas for most targets. While SDSS do not cover the whole sky (nor it is expected to do so), its catalogue of u magnitudes is the largest available so far. Also, the large number of stellar spectra which has been retrieved ($> 450,000$) makes it a possible benchmark to cross-check and validate stellar classifications based on photometry.

7.3.7 *ASAS*

The All Sky Automated Survey[2] (ASAS) is a project dedicated to constant photometric monitoring of the whole available sky (Pojmański 2001). One of the main objectives of ASAS is to find and catalog variable stars.

ASAS consists of two observing stations, one in LCO, Chile (since 1997) and the other on Haleakala, Maui (since 2006). Both are equipped with two wide-field 200 mm instruments, observing simultaneously in V and I band. The ASAS-3 Photometric V-band Catalogue contains over 15,000,000 light curves for stars brighter than about $V \sim 14$. The lower limit, due to saturation, is at $V \sim 8$ mag, but this value depends on a number of parameters (a focus, an exposure time, a place on frame) and changes in time. For now, ASAS-3 V-band and ASAS-2 I-band measurements are available. In most cases photometry is accurate to about 0.05 mag, but in many cases (due to problems with flatfielding and lack of colour information) errors could be 0.1 mag or larger.

The ASAS project published also the ASAS-3 Catalog of Variable Stars, which contains over 10,000 eclipsing binaries, almost 8,000 peri-

1 http://www.sdss.org/
2 http://www.astrouw.edu.pl/asas/

odic pulsating and over 31,000 irregular stars found among 15,000,000 stars on the sky south of the declination $+28°$.

7.3.8 *APASS*

The AAVSO Photometric All-Sky Survey[3] (APASS) will be conducted in five filters: Johnson B and V, plus Sloan g', r', i'. It will cover the magnitude range between $V \sim 10$ and $V \sim 17$. It will bridge the gap between Tycho2 and SDSS, plus cover the entire sky at the same depth as UCAC3.

Johnson B and V were chosen to extend the Tycho-2 calibration to fainter magnitudes and to match the many archival published datasets. Sloan g', r', i' passbands provide a direct link to the SDSS, SkyMapper, PanSTARRs etc. surveys, and provide a homogeneous catalog of brighter stars. Blending will be a problem in APASS. The pixel scale is 2.57 arcsec/pixel, the PSFs are purposely defocused to a FWHM of 1.5-2.0 pixels.

Data release 1 of APASS occurred on September 2010, and contains photometry for approximately four million stars distributed among several hundred discrete fields between $-10.15 < \delta < +87.35$. Each object will have a minimum of four photometric observations by the end of the survey, while DR1 has typically only two observations. The expected mean photometric errors will be few hundreths of mag.. The survey will take approximately two years to complete.

7.4 THE FORTHCOMING CATALOGS

7.4.1 *SkyMapper S3*

SkyMapper is a 1.35m survey telescope at Siding Spring Observatory featuring a 268-million pixel imager with a 5.7 deg^2 field of view. The SkyMapper telescope is designed to carry out the Stromlo Southern Sky Survey[4] (S3), a multi-color, multi-epoch survey of the southern sky. S3 will be analogous to the Sloan Digital Sky Survey in the North hemisphere with several enhancements, including temporal coverage, more precise measurements of stellar properties and coverage of large part of the Galactic Plane. Approximately 75% of the time on SkyMapper will be initially dedicated to the Southern Sky Survey.

Multi-epoch photometric measurements will be carried out on 20,000 deg^2 south of equator, on five standard ugriz filters plus a Strömgren-like v_s band specifically designed for stellar classification purposes. The absolute calibration will be accurate within 0.03 mag, while the positional accuracy will be better than 50 mas.

3 http://www.aavso.org/apass

4 http://msowww.anu.edu.au/skymapper/survey.php

In addition, a 5-Second Survey will be undertaken in photometric conditions for calibration of stars in the range 9-16 mag in all bands. This will provide the calibration of the survey and will allow the survey to be tied to the Hipparchos and Tycho-2 catalogs (and other photometric standard systems that are established in the southern hemisphere) to ensure uniformity across the sky.

7.5 STELLAR CLASSIFICATION TECHNIQUES

Stellar classification is traditionally performed with spectroscopy or intermediate-/narrow-band photometry. As these techniques are very time-consuming, such surveys are usually limited to very specific targets or sky regions. All-sky surveys such as the MK classification (Cannon & Pickering 1993), the HD classification (Houk & Swift 2000), and the Geneva-Copenhagen survey (Nordström et al. 2004) are limited to stars brighter than $V \sim 8$. Recent spectroscopical surveys such as SDSS (Abazajian et al. 2009) and RAVE (Steinmetz et al. 2006) go deeper but are limited to sky regions accessible from a single site and far from the galactic plane.

Beginning in the 2000s, with the advent of accurate all-sky catalogs such as Hipparcos, Tycho-2, and 2MASS, some authors have tried to extract stellar parameters using only wide-band photometry and proper motions. Some were driven by the need to extract a target list for exoplanet searches (e.g., Ammons et al. 2006 for the NHK radial velocity survey, Gould & Morgan 2003 for generic transit surveys). Other were trying to provide an all-sky calibration for the ugriz passbands (Ofek 2008; Pickles & Depagne 2010), or to develop a general method to classify galactic stellar populations (Bilir et al. 2006; Belikov & Röser 2008).

Most of these works employ similar input catalogs. Usually Tycho-2 B_T and V_T and 2MASS JHK_s magnitudes are chosen, as they provide uniform, precise all-sky photometry over passbands that contains useful informations on $[M/H]$ and $\log(g)$ (See Sec. 1). Proper motions, when used, are extracted also from Tycho-2. Unfortunately, most photometric classifications are limited to about $V \lesssim 11$ (and therefore to the Plato stellar samples P1-P4) by the completeness limit of Tycho-2. While 2MASS provides very good photometry ($\sigma_{phot} < 0.05$ mag) down to $V \sim 15$ and Tycho-2 proper motions are also well complemented by UCAC3 for stars brighter than $V \sim 15$, no reliable source of visual magnitudes is available for $V \gtrsim 11$ on the whole sky. Once full-coverage catalogs from APASS and SkyMapper will be released, it will be possibile to extend (and probably improve) those classifications to include the magnitude range of the candidate P5 targets $V \lesssim 13.5$.

7.5.1 *Ofek (2008) , Pickles & Depagne (2010)*

Ofek (2008) matches the 2MASS and Tycho-2 catalogs, and fits the resulting $B_T V_T JHK_s$ magnitudes with a set a library spectra taken from Pickles (1998). The χ^2 best-fit template is then associated to each star, and a set of SDSS griz synthetic magnitudes is evaluated on each template to construct an all-sky catalog of griz magnitudes for calibration purposes. Though not designed specifically to derive stellar parameters, this works provide a spectral type and luminosity class for $\sim$ 1.56 million Tycho-2 entries (and, for some spectral types, also metal rich/poor stars are discriminated). For some unknown reason, stars with $\delta \simeq 4°$, $54° \lesssim \delta \lesssim 59°$, $\delta \gtrsim 80°$ are lacking.

Pickles & Depagne (2010) extends the work done by Ofek by fitting updated spectral templates on a larger set of stellar magnitudes, having complemented the Tycho/2MASS $B_T V_T JHK_s$ with the photographic R_N magnitudes from USNO-B1.0 (through the NOMAD compiled catalog, Zacharias et al. 2005). Cuts are performed on 2MASS $J - H$, $H - K_s$ colors and Tycho-2 proper motions, attempting to discriminate giants from dwarfs when both templates fitted with a similar χ^2.

For our purposes, both the Ofek (2008) and Pickles & Depagne (2010) classifications should be treated with caution. Interstellar reddening is not accounted for, and this is known to make many distant, hot giants to be misclassified as cool dwarfs. If one select only candidate P1 targets ($V < 11$, SpT>F5 stars), the sample is strongly concentrated toward the galactic disk, and this is also more evident when selecting only K and M dwarfs, which should be distributed nearly isotropically in the sky. Moreover, K and M stars dominate the sample along the galactic plane, while F and G stars are expected to do so in a magnitude-limited sample. In summary, these kinds of classifications are not to be trusted when working at low galactic latitudes ($b < 20°$).

7.5.2 *Ammons et al. (2006)*

Ammons et al. (2006) develops an entirely empirical approach to identify metal-rich, low main-sequence stars as targets for N2K, a radial velocity search for hot jupiters (Fischer et al. 2005).

A training set of stars with both high-resolution spectra and photometry from Tycho-2 and 2MASS is employed to fit polynomials and spline functions to the broad-band colors extracted from $B_T V_T JHK_s$ magnitudes and Tycho-2 proper motions. Polynomials and spline functions are then fitted to the all Tycho-2 sources with a flexible χ^2-minimization procedure, in order to derive distance and temperature. The training set comes from Valenti & Fischer (2005), which contains over 1000 F, G, and K dwarfs with Keck HIRES spectra. For a selected

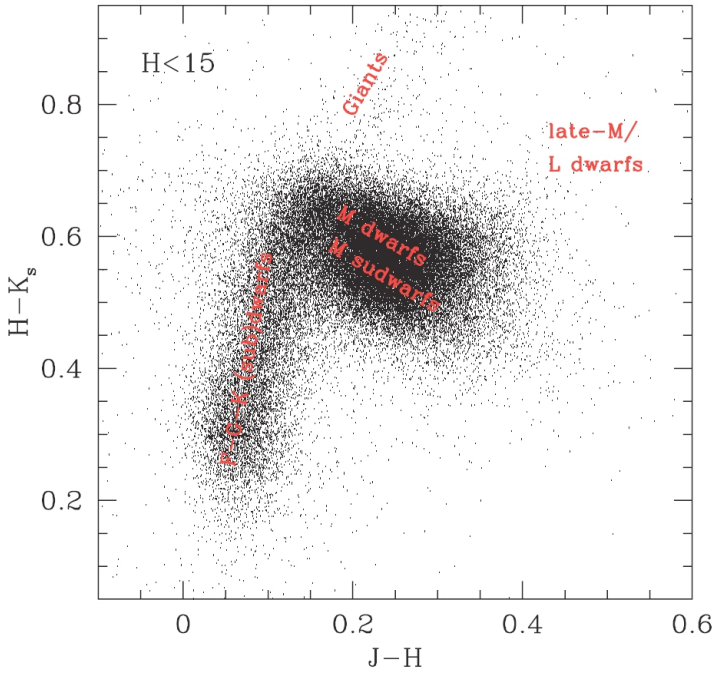

Figure 34: 2MASS JHK$_s$ color-color diagram for a sample of high proper motions (> 150 mas/yr) stars, from Lépine & Shara (2005).

subset of 354,822 FGK dwarfs, metallicity [M/H] and the probability of multeplicity are also derived with the same techniques, while T_{eff} is estimated with a finer polynomial function. For FGK dwarfs with photometric error $V < 0.05$ mag the temperature and metallicity models give a standard error of 70 K and 0.14 dex respectively. The binarity model can remove 70% of doubles with $1.25 < M_1/M_2 < 3.0$ from a magnitude-limited sample of dwarfs at a cost of cutting 20% of the sample.

This technique uses primarily the distance (and hence the absolute magnitude) as parameter to discriminate dwarfs from giants. It fails when trying to estimates directly log g. The main reasons are: (1) the physical processes that differentiate dwarfs from giants in photometry vary widely as a function of T_{eff}: a single polynomial or even a spline cannot be expected to capture all possible effects (2) Entire groups of stars are underrepresented by the Valenti & Fischer (2005) training set, namely, blue giants and cool red dwarfs. Though reddening is not taken into account, the use of proper motion to infer the distance minimize the contamination of the sample by giants even at low galactic latitudes.

7.5.3 *Contamination and completeness*

In order to assess the completeness and the fraction of contaminants of a sample selected by photometric classification algorithms, we ma-

tched both catalogs by Ammons et al. (2006) and Ofek (2008) with a reliable source of atmospheric parameters: the spectroscopic survey RAVE (Steinmetz et al. 2006).

Stars selected as FGK dwarfs according to their "photometric" T_{eff}, $\log(g)$ as estimated by Ammons et al. (2006) and Ofek (2008) are plotted in Fig. 37 as a function of their "spectroscopic" parameters T_{eff}, $\log(g)$ as tabulated in the RAVE data release 2 (DR2). Then the fraction of "false positives" (i. e., star misclassified as dwarfs by photometric algorithms) is estimated as the fraction of stars falling outside the boundaries $\log(g) > 3.5$ and $T_{eff} < 6600$ extracted from RAVE. The resulting contamination is $\sim$ 22% for Ofek (2008) and $\sim$ 14% for Ammons et al. (2006).

7.6 CONCLUSIONS

Considering that the vast majority of a magnitude-limited sample at $V \leqslant 11$ is composed by early-type and evolved giants, photometric classification techniques such those developed by Ammons et al. (2006) and Ofek (2008) lead to satisfactory results, and succeed in selecting a sample of FGK dwarfs with a contamination on the order of 14-22%. Such a fraction of contaminating objects is reasonable in the context of the selection of Plato P1 targets, as Plato has the capability to observe much more targets than the minimum number stated in the requirements. Thus, target density maps such those plotted in Fig. 35 and 36 will be useful to choose where to point the two long-duration FOV of Plato in order to maximize the number of detected planets and to minimize the time required by ground-based follow-up facilities to confirm and characterize those planets.

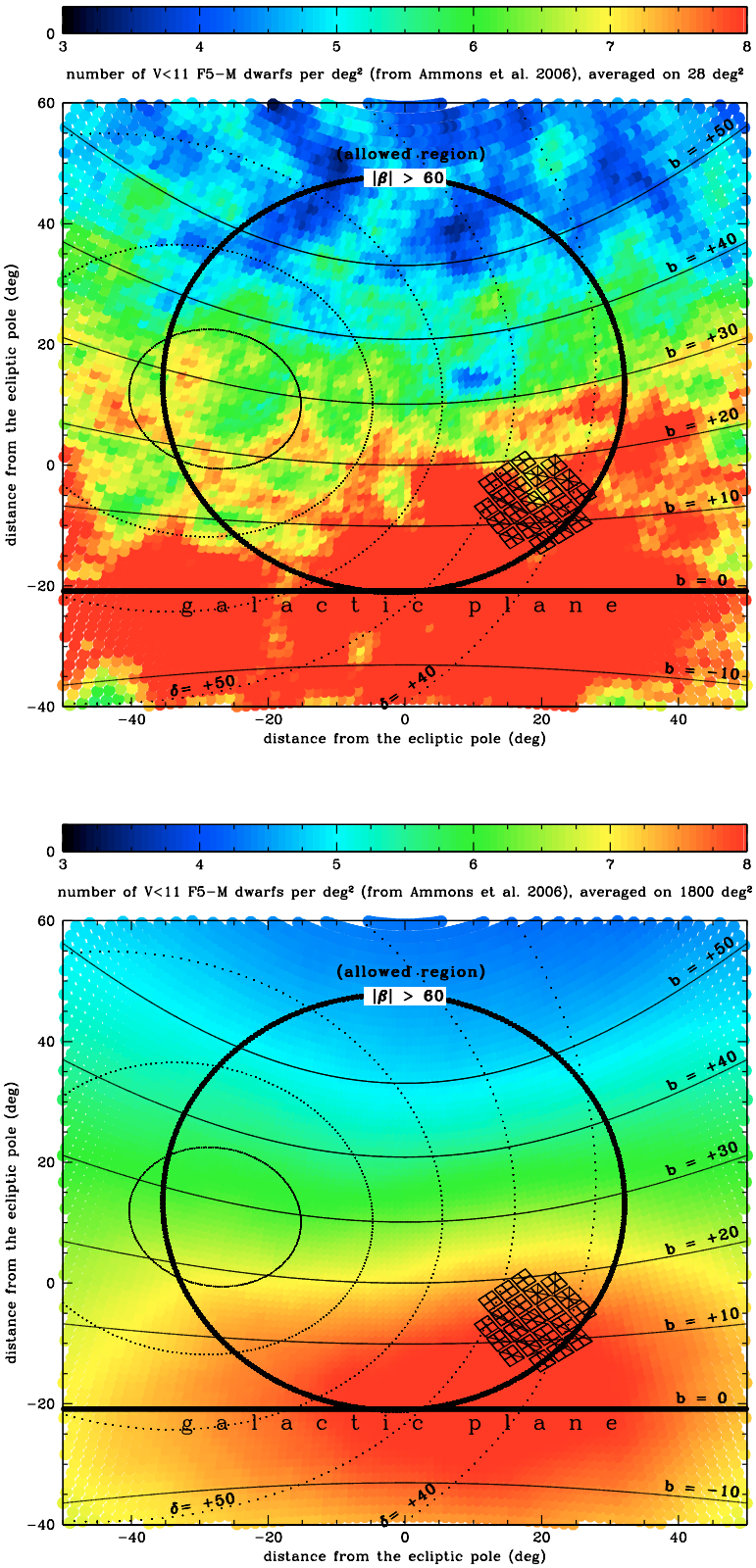

Figure 35: Density maps from Ammons et al. (2006) for the northern field.

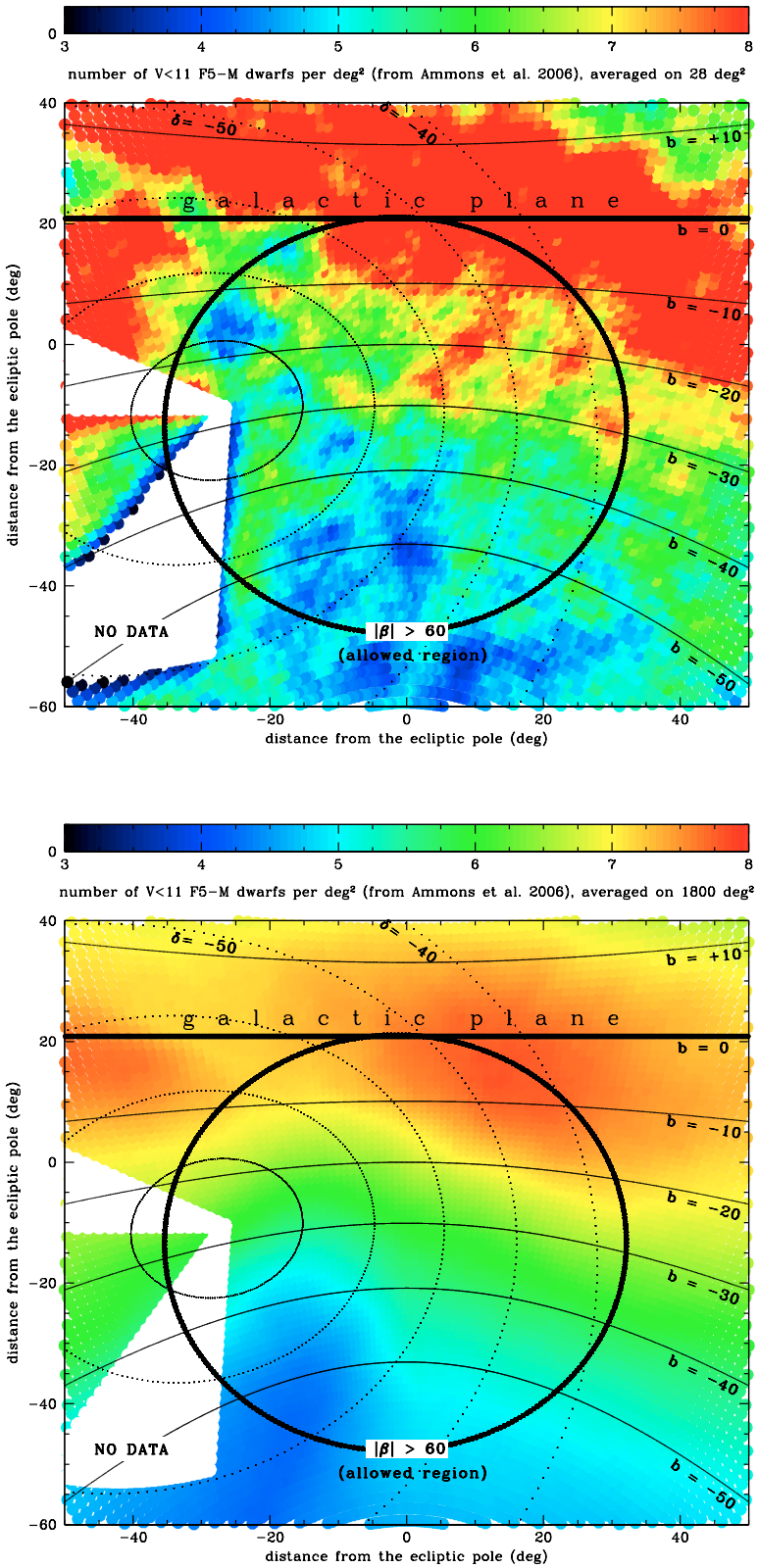

Figure 36: Density maps from Ammons et al. (2006) for the southern field.

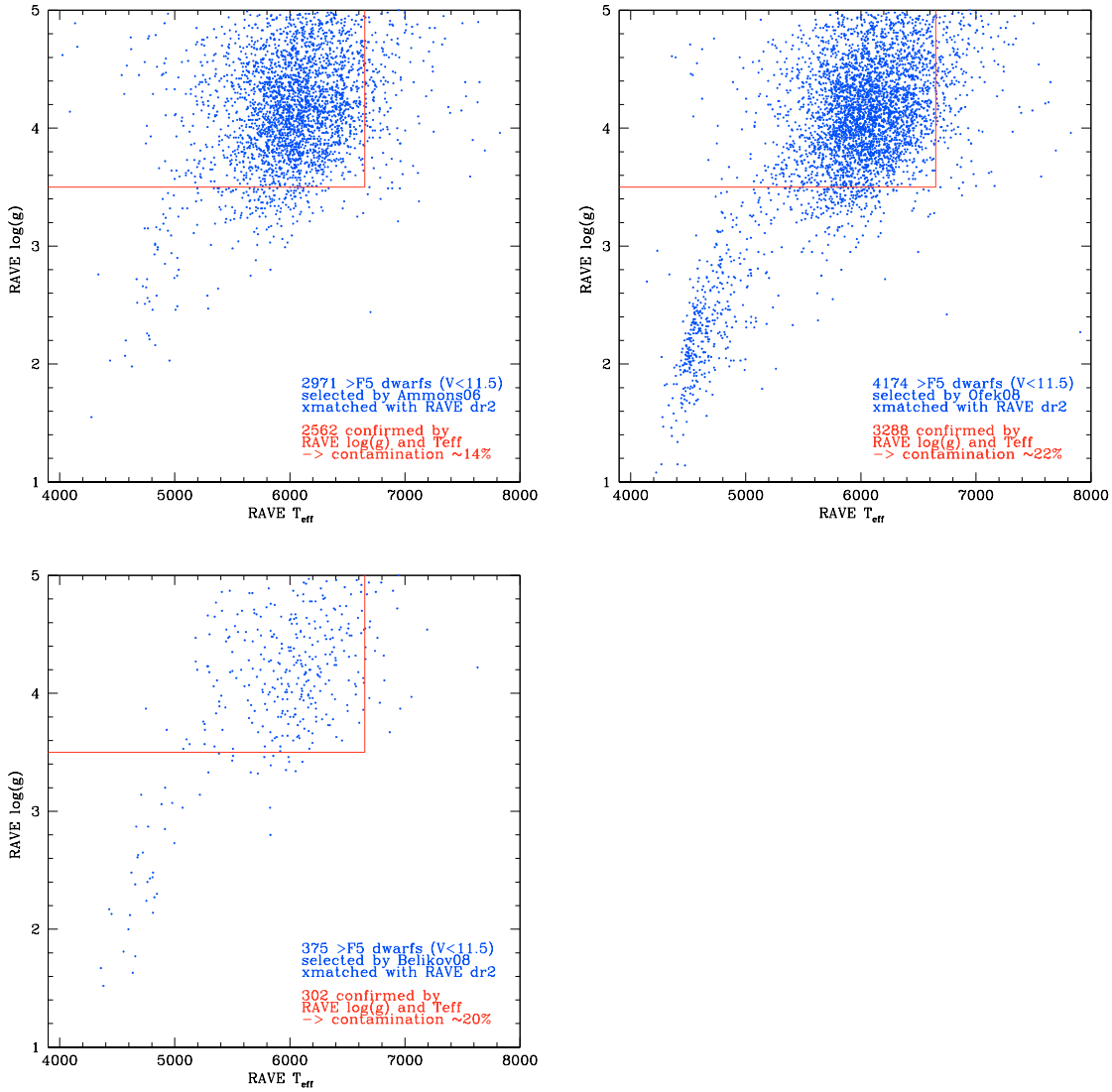

Figure 37: Estimate of the contamination fraction from a crosscheck with the RAVE DR1 data, for the all-sky databases published by 1) Ammons et al. (2006), 2) Ofek (2008), 3) Belikov & Röser (2008).

BIBLIOGRAPHY

Abazajian, K. N., Adelman-McCarthy, J. K., Agüeros, M. A., et al. 2009, ApJS, 182, 543

Agol, E., Steffen, J., Sari, R., & Clarkson, W. 2005, MNRAS, 359, 567

Albrow, M. D., Gilliland, R. L., Brown, T. M., et al. 2001, ApJ, 559, 1060

Ammons, S. M., Robinson, S. E., Strader, J., et al. 2006, ApJ, 638, 1004

Andersen, M. I., Freyhammer, L., & Storm, J. 1995, in European Southern Observatory Astrophysics Symposia, Vol. 53, European Southern Observatory Astrophysics Symposia, ed. P. Benvenuti, 87–+

Anderson, J. & Bedin, L. R. 2010, PASP, 122, 1035

Anderson, J. & King, I. R. 2000, PASP, 112, 1360

Anderson, J. & King, I. R. 2006, PSFs, Photometry, and Astronomy for the ACS/WFC, Tech. rep.

Anderson, J., King, I. R., Richer, H. B., et al. 2008, AJ, 135, 2114

Auvergne, M., Bodin, P., Boisnard, L., et al. 2009, A&A, 506, 411

Bailer-Jones, C. A. L. 2010a, MNRAS, 1784

Bailer-Jones, C. A. L. 2010b, MNRAS, 403, 96

Bakos, G. Á., Hartman, J., Torres, G., et al. 2011, ApJ, 742, 116

Bakos, G. Á., Howard, A. W., Noyes, R. W., et al. 2009, ApJ, 707, 446

Bakos, G. Á., Lázár, J., Papp, I., Sári, P., & Green, E. M. 2002, PASP, 114, 974

Ballard, S., Fabrycky, D., Fressin, F., et al. 2011, ApJ, 743, 200

Batalha, N. M., Borucki, W. J., Koch, D. G., et al. 2010, ApJ, 713, L109

Beaulieu, J.-P., Bennett, D. P., Fouqué, P., et al. 2006, Nature, 439, 437

Belikov, A. N. & Röser, S. 2008, A&A, 489, 1107

Benedict, G. F., McArthur, B. E., Forveille, T., et al. 2002, ApJ, 581, L115

Bessell, M. S. 2005, ARA&A, 43, 293

Bilir, S., Karaali, S., Güver, T., Karataş, Y., & Ak, S. G. 2006, Astronomische Nachrichten, 327, 72

Borucki, W. J., Koch, D., Basri, G., et al. 2010, Science, 327, 977

Borucki, W. J., Koch, D. G., Batalha, N., et al. 2012, ApJ, 745, 120

Boué, G., Oshagh, M., Montalto, M., & Santos, N. C. 2012, MNRAS, 422, L57

Broeg, C., Fernández, M., & Neuhäuser, R. 2005, Astronomische Nachrichten, 326, 134

Cannon, A. J. & Pickering, E. C. 1993, VizieR Online Data Catalog, 3135, 0

Cassan, A., Kubas, D., Beaulieu, J.-P., et al. 2012, Nature, 481, 167

Charbonneau, D., Allen, L. E., Megeath, S. T., et al. 2005, ApJ, 626, 523

Charbonneau, D., Brown, T. M., Latham, D. W., & Mayor, M. 2000, ApJ, 529, L45

Charbonneau, D., Brown, T. M., Noyes, R. W., & Gilliland, R. L. 2002, ApJ, 568, 377

Charbonneau, D., Winn, J. N., Everett, M. E., et al. 2007, ApJ, 658, 1322

Christiansen, J. L., Ballard, S., Charbonneau, D., et al. 2011, ApJ, 726, 94

Ciardi, D. R., von Braun, K., Bryden, G., et al. 2011, AJ, 141, 108

Claret, A. 2000, A&A, 363, 1081

Claret, A. 2004, A&A, 428, 1001

Collier Cameron, A., Bouchy, F., Hébrard, G., et al. 2007, MNRAS, 375, 951

Coughlin, J. L., Stringfellow, G. S., Becker, A. C., et al. 2008, ApJ, 689, L149

Cox, A. N. 2000, Allen's astrophysical quantities, ed. Cox, A. N.

Cresswell, P. & Nelson, R. P. 2006, A&A, 450, 833

Damasso, M., Giacobbe, P., Calcidese, P., et al. 2010, PASP, 122, 1077

de Marchi, F., Poretti, E., Montalto, M., Desidera, S., & Piotto, G. 2010, A&A, 509, A17

de Marchi, F., Poretti, E., Montalto, M., et al. 2007, A&A, 471, 515

Díaz, R. F., Rojo, P., Melita, M., et al. 2008, ApJ, 682, L49

Dotter, A., Chaboyer, B., Jevremović, D., et al. 2007, AJ, 134, 376

Dravins, D., Lindegren, L., Mezey, E., & Young, A. T. 1998, PASP, 110, 610

Dzigan, Y. & Zucker, S. 2012, ArXiv e-prints

Eastman, J., Siverd, R., & Gaudi, B. S. 2010, PASP, 122, 935

Fabrycky, D. C. 2010, ArXiv e-prints

Ferraz-Mello, S. 1981, AJ, 86, 619

Fischer, D. A., Laughlin, G., Butler, P., et al. 2005, ApJ, 620, 481

Fischer, D. A. & Valenti, J. 2005, ApJ, 622, 1102

Fregeau, J. M., Chatterjee, S., & Rasio, F. A. 2006, ApJ, 640, 1086

Fukui, A., Narita, N., Tristram, P. J., et al. 2011, PASJ, 63, 287

Fulton, B. J., Shporer, A., Winn, J. N., et al. 2011, AJ, 142, 84

Gibson, N. P., Pollacco, D., Simpson, E. K., et al. 2009, ApJ, 700, 1078

Gibson, N. P., Pollacco, D., Simpson, E. K., et al. 2008, A&A, 492, 603

Gibson, N. P., Pollacco, D. L., Barros, S., et al. 2010, MNRAS, 401, 1917

Gilliland, R. L., Brown, T. M., Guhathakurta, P., et al. 2000, ApJ, 545, L47

Giménez, A. 2006, A&A, 450, 1231

Gontcharov, G. A. 2009, Astronomy Letters, 35, 638

Gould, A. & Loeb, A. 1992, ApJ, 396, 104

Gould, A. & Morgan, C. W. 2003, ApJ, 585, 1056

Gratton, R. G., Bragaglia, A., Carretta, E., et al. 2003, A&A, 408, 529

Hansen, B. M. S., Anderson, J., Brewer, J., et al. 2007, ApJ, 671, 380

Hartman, J. D., Gaudi, B. S., Holman, M. J., et al. 2008, ApJ, 675, 1254

Hartman, J. D., Gaudi, B. S., Holman, M. J., et al. 2009, ApJ, 695, 336

Hebb, L., Collier-Cameron, A., Loeillet, B., et al. 2009, ApJ, 693, 1920

Henry, G. W., Marcy, G. W., Butler, R. P., & Vogt, S. S. 2000, ApJ, 529, L41

Høg, E., Fabricius, C., Makarov, V. V., et al. 2000, A&A, 355, L27

Holman, M. J., Fabrycky, D. C., Ragozzine, D., et al. 2010, Science, 330, 51

Holman, M. J. & Murray, N. W. 2005, Science, 307, 1288

Holman, M. J., Winn, J. N., Latham, D. W., et al. 2006, ApJ, 652, 1715

Horne, J. H. & Baliunas, S. L. 1986, ApJ, 302, 757

Houk, N. & Swift, C. 2000, VizieR Online Data Catalog, 3214, 0

Howard, A. W., Marcy, G. W., Bryson, S. T., et al. 2011, ArXiv e-prints

Jenkins, J. M., Caldwell, D. A., & Borucki, W. J. 2002, ApJ, 564, 495

Johns-Krull, C. M., McCullough, P. R., Burke, C. J., et al. 2008, ApJ, 677, 657

Johnson, J. A., Aller, K. M., Howard, A. W., & Crepp, J. R. 2010, PASP, 122, 905

Johnson, J. A. & Apps, K. 2009, ApJ, 699, 933

Kalas, P., Graham, J. R., Chiang, E., et al. 2008, Science, 322, 1345

Kane, S. R. & Gelino, D. M. 2012, ArXiv e-prints

Kipping, D. M. 2009a, MNRAS, 392, 181

Kipping, D. M. 2009b, MNRAS, 396, 1797

Kovács, G., Zucker, S., & Mazeh, T. 2002, A&A, 391, 369

Lagrange, A.-M., Gratadour, D., Chauvin, G., et al. 2009, A&A, 493, L21

Lang, D., Hogg, D. W., Mierle, K., Blanton, M., & Roweis, S. 2010, AJ, 139, 1782

Lasker, B. M., Lattanzi, M. G., McLean, B. J., et al. 2008, AJ, 136, 735

Lee, J. W., Kim, S.-L., Kim, C.-H., et al. 2009, AJ, 137, 3181

Lépine, S. & Shara, M. M. 2005, AJ, 129, 1483

Lissauer, J. J., Fabrycky, D. C., Ford, E. B., et al. 2011, Nature, 470, 53

Littlefield, C. 2011, ArXiv e-prints

Lovis, C. & Mayor, M. 2007, A&A, 472, 657

Lovis, C., Mayor, M., Bouchy, F., et al. 2009, in IAU Symposium, Vol. 253, IAU Symposium, 502–505

Maciejewski, G., Dimitrov, D., Neuhäuser, R., et al. 2010, MNRAS, 407, 2625

Maciejewski, G., Dimitrov, D., Neuhäuser, R., et al. 2011, MNRAS, 411, 1204

Mandel, K. & Agol, E. 2002, ApJ, 580, L171

Marcy, G., Butler, R. P., Fischer, D., et al. 2005, Progress of Theoretical Physics Supplement, 158, 24

Marois, C., Macintosh, B., Barman, T., et al. 2008, Science, 322, 1348

Mayor, M. & Queloz, D. 1995, Nature, 378, 355

Merline, W. J. & Howell, S. B. 1995, Experimental Astronomy, 6, 163

Meschiari, S. & Laughlin, G. P. 2010, ApJ, 718, 543

Mochejska, B. J., Stanek, K. Z., Sasselov, D. D., et al. 2006, AJ, 131, 1090

Mochejska, B. J., Stanek, K. Z., Sasselov, D. D., et al. 2005, AJ, 129, 2856

Monet, D. G., Levine, S. E., Canzian, B., et al. 2003, AJ, 125, 984

Montalto, M., Piotto, G., Desidera, S., et al. 2007, A&A, 470, 1137

Montalto, M., Villanova, S., Koppenhoefer, J., et al. 2011, A&A, 535, A39

Nascimbeni, V., Piotto, G., Bedin, L. R., & Damasso, M. 2011a, A&A, 527, A85+

Nascimbeni, V., Piotto, G., Bedin, L. R., & Damasso, M. 2011b, A&A, 527, A85

Nascimbeni, V., Piotto, G., Bedin, L. R., et al. 2011c, A&A, 532, A24

Naylor, T. 1998, MNRAS, 296, 339

Nesvorný, D., Kipping, D. M., Buchhave, L. A., et al. 2012, Science, 336, 1133

Nordström, B., Mayor, M., Andersen, J., et al. 2004, A&A, 418, 989

Ofek, E. O. 2008, PASP, 120, 1128

Paczynski, B. 1991, ApJ, 371, L63

Pál, A., Sárneczky, K., Szabó, G. M., et al. 2011, MNRAS, 413, L43

Palmer, D. M. 2009, ApJ, 695, 496

Payne, M. J. & Ford, E. B. 2011, ApJ, 729, 98

Pepe, F., Mayor, M., Delabre, B., et al. 2000, in Society of Photo-Optical Instrumentation Engineers (SPIE) Conference Series, Vol. 4008, Society of Photo-Optical Instrumentation Engineers (SPIE) Conference Series, ed. M. Iye & A. F. Moorwood, 582–592

Perryman, M. A. C. & ESA, eds. 1997, ESA Special Publication, Vol. 1200, The HIPPARCOS and TYCHO catalogues. Astrometric and photometric star catalogues derived from the ESA HIPPARCOS Space Astrometry Mission

Pickles, A. & Depagne, É. 2010, ArXiv e-prints

Pickles, A. J. 1998, PASP, 110, 863

Poddaný, S., Brát, L., & Pejcha, O. 2010, New A, 15, 297

Pojmański, G. 2001, in Astronomical Society of the Pacific Conference Series, Vol. 246, IAU Colloq. 183: Small Telescope Astronomy on Global Scales, ed. B. Paczynski, W.-P. Chen, & C. Lemme, 53–+

Pollacco, D., Skillen, I., Collier Cameron, A., et al. 2008, MNRAS, 385, 1576

Pollacco, D. L., Skillen, I., Collier Cameron, A., et al. 2006, PASP, 118, 1407

Pont, F., Bouchy, F., Queloz, D., et al. 2004, A&A, 426, L15

Pont, F., Zucker, S., & Queloz, D. 2006, MNRAS, 373, 231

Pravdo, S. H. & Shaklan, S. B. 2009, ApJ, 700, 623

Richer, H. B., Dotter, A., Hurley, J., et al. 2008, AJ, 135, 2141

Sada, P. V., Deming, D., Jennings, D. E., et al. 2012, ArXiv e-prints

Santos, N. C., Mayor, M., Bonfils, X., et al. 2011, A&A, 526, A112+

Santos, N. C., Mayor, M., Naef, D., et al. 2001, A&A, 379, 999

Sato, B., Izumiura, H., Toyota, E., et al. 2007, ApJ, 661, 527

Scalo, J., Kaltenegger, L., Segura, A. G., et al. 2007, Astrobiology, 7, 85

Schlaufman, K. C. & Laughlin, G. 2011, ArXiv e-prints

Schwarz, R., Haghighipour, N., Eggl, S., Pilat-Lohinger, E., & Funk, B. 2011, MNRAS, 414, 2763

Seager, S. 2011a, Exoplanets

Seager, S. 2011b, Exoplanets, ed. Piper, S.

Seager, S. & Deming, D. 2010, ARA&A, 48, 631

Shporer, A., Tamuz, O., Zucker, S., & Mazeh, T. 2007, MNRAS, 376, 1296

Silvotti, R., Schuh, S., Janulis, R., et al. 2007, Nature, 449, 189

Simpson, E. K., Barros, S. C. C., Brown, D. J. A., et al. 2010, ArXiv e-prints

Skrutskie, M. F., Cutri, R. M., Stiening, R., et al. 2006, AJ, 131, 1163

Skrutskie, M. F., Cutri, R. M., Stiening, R., et al. 2003, VizieR Online Data Catalog, 7233, 0

Southworth, J. 2008, MNRAS, 386, 1644

Southworth, J. 2010a, MNRAS, 408, 1689

Southworth, J. 2010b, MNRAS, 408, 1689

Southworth, J., Bruni, I., Mancini, L., & Gregorio, J. 2012, MNRAS, 2177

Southworth, J., Hinse, T. C., Burgdorf, M. J., et al. 2009a, MNRAS, 399, 287

Southworth, J., Hinse, T. C., Jørgensen, U. G., et al. 2009b, MNRAS, 396, 1023

Southworth, J., Maxted, P. F. L., & Smalley, B. 2004, MNRAS, 351, 1277

Southworth, J., Wheatley, P. J., & Sams, G. 2007, MNRAS, 379, L11

Sozzetti, A. 2005, PASP, 117, 1021

Spurzem, R., Giersz, M., Heggie, D. C., & Lin, D. N. C. 2009, ApJ, 697, 458

Steele, I. A., Bates, S. D., Gibson, N., et al. 2008, in Society of Photo-Optical Instrumentation Engineers (SPIE) Conference Series, Vol. 7014, Society of Photo-Optical Instrumentation Engineers (SPIE) Conference Series

Steffen, J. H. & Agol, E. 2005, MNRAS, 364, L96

Steinmetz, M., Zwitter, T., Siebert, A., et al. 2006, AJ, 132, 1645

Stello, D. & Gilliland, R. L. 2009, ApJ, 700, 949

Straižys, V., Lazauskaitė, R., Brown, A. G. A., & Zdanavičius, K. 2006, Baltic Astronomy, 15, 449

Struve, O. 1952, The Observatory, 72, 199

Szabó, G. M., Kiss, L. L., Benkő, J. M., et al. 2010, A&A, 523, A84+

Tamuz, O., Mazeh, T., & Zucker, S. 2005, MNRAS, 356, 1466

Teig, M. 2008, PASP, 120, 474

Thorsett, S. E., Arzoumanian, Z., Camilo, F., & Lyne, A. G. 1999, ApJ, 523, 763

Tinney, C. G., Butler, R. P., Marcy, G. W., et al. 2006, ApJ, 647, 594

Torres, G., Bakos, G. A., Hartman, J., et al. 2010, ArXiv e-prints

Torres, G., Bakos, G. Á., Kovács, G., et al. 2007, ApJ, 666, L121

Tripathi, A., Winn, J. N., Johnson, J. A., et al. 2010, ApJ, 715, 421

Udry, S., Mayor, M., Benz, W., et al. 2006, A&A, 447, 361

Udry, S. & Santos, N. C. 2007, ARA&A, 45, 397

Valenti, J. A. & Fischer, D. A. 2005, ApJS, 159, 141

van de Kamp, P. 1969, AJ, 74, 757

van Leeuwen, F. 2007, A&A, 474, 653

van Saders, J. L. & Gaudi, B. S. 2011, ApJ, 729, 63

Vaníček, P. 1971, Ap&SS, 12, 10

Veras, D., Ford, E. B., & Payne, M. J. 2011, ApJ, 727, 74

Weldrake, D. T. F., Sackett, P. D., & Bridges, T. J. 2008, ApJ, 674, 1117

Weldrake, D. T. F., Sackett, P. D., Bridges, T. J., & Freeman, K. C. 2005, ApJ, 620, 1043

Winn, J. N. 2010, ArXiv e-prints

Winn, J. N., Holman, M. J., Torres, G., et al. 2008, ApJ, 683, 1076

Winn, J. N., Johnson, J. A., Howard, A. W., et al. 2010, ApJ, 718, 575

Wittenmyer, R. A., Tinney, C. G., Butler, R. P., et al. 2011, ArXiv e-prints

Wolszczan, A. & Frail, D. A. 1992, Nature, 355, 145

Zacharias, N., Finch, C., Girard, T., et al. 2010, AJ, 139, 2184

Zacharias, N., Monet, D. G., Levine, S. E., et al. 2004, in Bulletin of the American Astronomical Society, Vol. 36, American Astronomical Society Meeting Abstracts, 1418

Zacharias, N., Monet, D. G., Levine, S. E., et al. 2005, VizieR Online Data Catalog, 1297, 0

Zdanavicius, K. 1998, Baltic Astronomy, 7, 551

Zdanavičius, K. 2005, Baltic Astronomy, 14, 104

Zechmeister, M. & Kürster, M. 2009, A&A, 496, 577

Zhang, J.-C., Cao, C., Song, N., Wang, F.-G., & Zhang, X.-T. 2011, Chinese Astron. Astrophys., 35, 409

Zwitter, T. & Henden, A. A. 2003, in Astronomical Society of the Pacific Conference Series, Vol. 298, GAIA Spectroscopy: Science and Technology, ed. U. Munari, 489–+

LIST OF TABLES

Table 17 Comparison between the main photometric and astrometric catalogs reviewed for this work. When available, for each entry are provided: the actual coverage as fraction of the sky, the approximate V magnitude range, the photometric system employed, the photometric and astrometic error for typical, well-exposed targets, and the availability of proper motions. 123